Investigation of tin oxide (SnO_x) gas sensors based on monodisperse nanoparticle films

Der Fakultät für Ingenieurwissenschaften
der Universität Duisburg-Essen
zur Erlangung des akademischen Grades eines

Doktor-Ingenieurs

genehmigte Dissertation

von

Marcus Kennedy

aus

Bonn

Referent:	Prof. Dr.-Ing. H. Fißan
Korreferent:	Prof. Dr.-Ing. H. Hahn
Tag der mündlichen Prüfung:	28. Januar 2004

meiner lieben Frau

und meinem lieben Vater

Vorwort

Die vorliegende Arbeit entstand während meiner Tätigkeit als wissenschaftlicher Angestellter im Fachgebiet Prozeß- und Aerosolmeßtechnik der Fakultät für Ingenieurwissenschaften an der Universität Duisburg-Essen.

Diese Arbeit wurde als Teilprojekt des Sonderforschungsbereiches 445 Nanopartikel aus der Gasphase: "Entstehung, Struktur, Eigenschaften" von der DFG gefördert.

Mein besonderer Dank gilt dem ehemaligem Leiter des Fachgebiets Prozeß- und Aerosolmeßtechnik, Herrn Prof. Dr.-Ing. Heinz Fissan, der es mir ermöglichte, diese Arbeit durchzuführen. Herr Prof. Dr.-Ing. Heinz Fissan gab mir jederzeit große wissenschaftliche Freiheit und brachte mir sehr viel Vertrauen entgegen.

Herzlich bedanke ich mich bei den ehemaligen Arbeitskollegen der AMT. Insbesondere möchte Herrn Dr. Frank Jordan, der immer für konstruktive fachliche Diskussion Zeit hatte, Herrn Dipl.-Ing. Ulrich Drosten für die wertvollen Hinweise und Herrn Christoph Kleinert für die gute Zusammenarbeit danken.

Vielen Dank auch an Herrn Dr. Hartmut Wiggers und Herrn Dr. Nienhaus, mit denen ich viele interessante und sachdienliche Diskussionen im Bereich der chemischen Gassensorik geführt habe.

Unter anderem gilt besonderer Dank Herrn Prof. Dr.-Ing. Horst Hahn vom Fachbereich Materialwissenschaften an der Technischen Universität Darmstadt, der durch wertvolle Diskussionen und kritische Bemerkungen wesentlich zum Gelingen meiner Arbeit beigetragen hat.

An dieser Stelle danke ich auch sehr herzlich meiner Frau Ira, meinem Vater Philip, Peter Rang und Ingo und Magarethe Alberty, die sich immer für meine Arbeit begeisterten.

Contents

Symbols

e	$1.602{\cdot}10^{-19}$ As	Elementary charge
k	$1.38066{\cdot}10^{-23}$ J/K	Boltzmann‘s constant
E_{vac}	eV	Vacuum energy level
E_{C}	eV	Energy level of conduction band
E_{V}	eV	Energy level of valence band
E_{F}	eV	Energy level of Fermi energy
E_{t}	eV	Energy level of surface barrier
V_{s}	eV	Schottky barrier height
χ	eV	Electron affinity
φ	eV	Electron work function
δ	eV	Dope parameter
L_{D}	m	Debeye length
N_{s}	m^{-2}	Number of occupied adsorbed places
N_{d}	m^{-3}	Donator density
ρ	m^{-3}	Charge carrier density
ε_0	$8.8{\cdot}10^{-12}$As/Vm	Permittivity of vacuum level
ε_{r}		Permittivity of semiconductor
D_{mi}	m	Initial mobility diameter
D_{ms}	m	Sintered mobility diameter
ϕ	V	Electrical potential

ρ	$(\Omega\mathrm{m})^{-1}$	Conductivity
μ	m^2/Vs	Charge carrier mobility
n	m^{-3}	Charge carrier concentration
G	Ω^{-1}	Conductance
H_p	eV	Energy after physisorption
H_C	eV	Energy after chemisorption
D	m	Crystallite size
V	J	Lennard-Jones potential
ε		Depth of potential cavity
σ	m	Distance between interacting particles
r	m	Atomic distance
Θ		Langmuir-Isotherm
N	m^{-3}	Particle number concentration
S		Sensivity
U	V	Voltage
I	A	Electrical current
τ	s	Response time constant
R	Ω	Electrical resistance
D_K	m^2/s	Knudsen diffusion coefficient
T	°C	Temperature
M	g/mol	Molecular weight
r_p	m	Pore radius
$\dot{\mathrm{x}}$		Neck growth rate
γ	J/m^2	Surface tension
a	m	Initial particle radius
d_ox	m	Silicon oxide thickness
t	s	Process duration

Chapter 1

Introduction

1.1 General

It has been known for a long time that the adsorption of gas molecules on a metal-oxide semiconductor surface can cause a significant change in the electrical resistance of the material [Weisz [88]]. Their surface properties are sensitive to changes in the gas atmosphere, especially on small amounts of hydrocarbons and hydrogen [Seiyama et al.[78]]. Tin oxide (SnO_2), which is an n-type semiconductor material, is one of the most investigated materials [McAleer et al. [59]]. The gas-sensing mechanism depends on chemical and electronic properties and on the three-dimensional ordering of both the bulk and the surface material, and is mainly influenced by the surface region of the grains/particles. Göpel et al. emphasised that the development and improvement of a chemical sensor requires a balance between empirical knowledge and systematic research as long as the basic processes involved are unknown [Göpel [30]]. Accordingly, studying the structure as well as the volume and surface chemical composition, is of great importance to better understand the gas-sensing mechanism [Martinelli et al. [58]].

The gas-sensing mechanism is still not fully understood. It is described as a chemical adsorption/desorption process of oxygen on the surface of sensing materials [Ihokura et al. [40] and Wada et al., [87]], followed by a charge transfer mechanism between the adsorbate and surface of the sensing material, leading to a measurable change in the electrical resistance. During this mechanism a space charge region with a thickness of $\sim$3 nm is built at the surface leading to a decreased electrical conductance. If the sensing material is exposed to a reducing atmosphere, such as air containing carbon monoxide, ethanol, hydrogen or methane, surface reactions will result in a lower surface

coverage of oxygen adsorbates and, therefore, in an increased conductance [Shimizu et al. [81]]. Oxidising gases, such as ozone and nitrogen oxide, can also be detected by metal-oxide gas sensors [Zampiceni et al. [93] and Dieguez et al. [20]].

Regarding the chemical composition, it is of importance to know the stoichiometry because this can have an effect on the gas-sensing properties of metal-oxide materials [Martinelli et al. [58]]. The oxygen stoichiometry of tin oxide can lie between SnO and SnO_2. Additionally, different crystallographic phases of tin oxide exist. Generally, understoichiometric tin oxide (SnO_{2-x}) is used as sensing material because oxygen vacancies are necessary for the gas-sensing mechanism. Consequently, the chemical composition during synthesis needs to be optimised and a stable crystallographic structure and stoichiometry must be formed for best sensor operations. In spite of many studies concerning the oxidation of SnO_x thin films prepared from Sn or SnO_2 precursors [Yoo et al. [92]], only a little amount of work on the oxidation process of SnO nanoparticles can be found in literature. Nevertheless, it is known that annealing treatments and structure influence the sensitivity of SnO_2 thin film gas sensors [Pan et al. [69]].

Nanostructured materials for gas-sensing applications are of great interest due to their higher surface/volume ratio compared to that of bulk material leading to a larger reactive surface. Additionally, microelectronic circuitry provides the means of achieving low fabrication cost and ease of miniaturisation of nanostructured gas-sensing devices [Chung et al. [13]]. SnO_2 gas sensors are one of the examples of functional materials where the use of nanoparticles was shown to lead to improved sensor properties due to the higher surface to volume ratio [Baik et al. [3]]; nanoparticles build porous films, thus increasing the reactive surface in relation to the whole material volume of the dense film.

In 1982, the sensitivity of dense nanoparticle films was compared with that of porous nanoparticle films with mean grain sizes in the order of 7-12 nm [Ogawa et al. [67]]. The increased resistance change in the nanoparticle porous layer in ethanol was explained by showing that the charge carrier mobility is not a function of the concentration of one gas in the case of dense films, but is strongly dependent on the gas concentration for the porous nanocrystalline films; this resulted from the charge carrier mobility modulation, caused by the gas adsorption leading to higher sensitivity values. Porous layers have a higher reactive surface: this causes an increased gas adsorption quantity. Consequently, the mobility is influenced by the morphology of the

layer being changed.

Significant alterations in the resistance, due to the change of the gas ambient, are expected if a material is composed of very small SnO_2 particles; the particle size should be approximately twice the depth of the space charge region. In particular, the use of grain sizes below 6 nm results in large increases in sensitivity [Xu et al. [91]]. However, changing the grain size is normally accompanied by a change in the material structure and chemical composition.

Many different synthesis methods have been used to study the properties of nanoparticle gas-sensing layers. The most popular methods, as indicated in Table 1.1, are sol-gel and gas-phase condensation. The results of studies, which determined both the SnO_2 particle size and the sensitivity of the corresponding nanoparticle film gas sensor, are presented. Note that it is not possible to correlate directly particle size with sensitivity from these studies because other parameters which influence the electrical properties of the metal-oxide gas sensor are not shown.

Generally, sensitivity diminishes with a decreasing gas concentration. Other important aspects are the operating temperature and gas type: these must be taken into account in comparing gas-sensing measurements between the various researchers. For instance, Barbi et al. made gas-sensing measurements of particle layers with a mean particle size of 15.5 nm and a thickness of 155 nm and obtained a sensitivity value of 90 at 191 °C and 500 at 300 °C for 15 ppm NO_2 [Barbi et al. [5]]. Baik et al. produced particle layers by means of the sol-gel method and, subsequently, by a calcination process: a sensitivity value of 1,700 was obtained for particle layers with a mean crystallite size of 9 nm at 600 °C for 800 ppm H_2 and a value of 250 for particle layers with a mean diameter of 18 nm after calcination for the same gas concentration [Baik et al. [3]]; unfortunately, the work was done using a different gas type and film thickness was not mentioned although this has a significant influence on the sensitivity of different gas types. It was discovered in another study that the sensitivity for H_2 decreases as film thickness increases, while the CO response was almost independent of the film thickness [Sakai et al. [74]].

For an objective comparison between different sensor material structures, particular attention must be given to the particle size as well as to the nanoparticle film dimensions and chemical composition which have to be identical. To illustrate this: the grain size was altered by changing the par-

tial pressure of oxygen during the synthesis, so that the stoichiometry of the films with different particle sizes varied [Ogawa et al. [65][66]]. For gas-sensing measurements, it is important to have grain transitions which are conducting, i.e. grains which are in the conducting state. Aging effects, during the heating of the layer to reach a certain operating temperature, can destroy the particle size distribution because small grains can sinter to compact clusters and, thus, create larger grains. One very popular method to obtain size-dependent gas-sensing properties is to calcinate the samples at temperatures of 500-900 °C. It has been shown that a calcination process changes the particle size distribution [Baik et al. [3]].

Another method used to vary the grain size is to add different metals to the SnO_2 before sintering the films at 700 °C, but then the effects of dopant and grain size are difficult to distinguish [Xu et al. [91]]. Annealing temperatures higher than 600 °C are applied to stabilise the microstructure so that no altering process during sensor operating occurs. However, almost no size-dependent gas-sensing measurements have been achieved for monodisperse particles without an additional treatment, such as calcination or doping.

Experiments up to now seem to indicate that the production of monodisperse SnO_2 particles in the gas-phase with different sizes is the best method to investigate their size-dependent characteristics. In this investigation, a synthesis procedure was developed to obtain tailored nanoparticle films from monosized tin oxide nanoparticles. Various particle and film characteristics can be independently controlled. However, the production of nanostructured devices also requires the development of specially configured substrates.

1.2 Structure of this investigation

The purpose of this investigation is to produce a gas-sensing device based on monodisperse SnO_x nanoparticles and to examine the particle size and chemical composition dependent properties of nanoparticle films. Accordingly, a thin film synthesis technique to generate monodisperse SnO_x nanoparticles with a defined chemical composition has been developed. This investigation will show how the process parameters affect the gas-sensing properties of the nanoparticle films generated and, consequently, will provide information to enable the material dependent properties of defined SnO_x gas sensors produced in the gas phase to be better understood. Furthermore, the production of commercially available metal-oxide gas sensors can be improved by means

Bibliography	Synthesis method	Size-variation method	Particle size (nm) smallest; largest	Sensitivity values
Ogawa et al. [65]	gas phase condensation	varying oxygen pressure	3; 15	1 - 10
Li et al., 2002[53]	sol-gel	annealing	3; 15	1 - 100
Liu et al. [54]	laser ablation	different targets; annealing	4; 46	1 - 200
Barbi et al. [5]	reactive sputtering	unknown	4; 16	1.5 - 20,000
Xu et al. [91]	sol-gel	calcination; doping	5; 32	10 - 360
Baik et al. [3]	hydrothermal treatment	solution concentration	5; 32	up to 2,000
Sakai et al. [74]	sol-gel	unknown	6	100 - 360
Jin et al. [42]	sol-gel	calcination	7; 15	2 - 10
Herrmann et al. [37]	gas phase condensation	unknown	9	unknown
Pan et al. [68]	sol-gel	unknown	11	1 - 18
Adachi et al. [1]	gas phase condensation	furnace temperature	12; 100	unknown
Diequez et al. [22]	sol-gel	calcination	20; 110	1.5 - 40
Fau et al. [26]	decomposition of organo-	unknown	20	7 - 80
Nayral et al. [63]	metallic precursor	unknown	20	unknown
Panchapakesan et al. [70]	decomposition of organo-metallic precursor	unknown	20; 120	2 - 3
Baraton et al. [4]	laser evaporation	unknown	8; 16	169.8

Table 1.1: Overview of different nanoparticle synthesis methods including particle size and sensitivity values.

of using suitable nanoparticles.

Chapter 2 gives a basic overview of the basic gas-sensing mechanism and the important parameters which influence the gas-sensing properties of nanoparticle films and the thickness of the space charge region; it concentrates on the physical effects on metal-oxide surfaces in different gas ambients and provides information about possible changes in the sensing characteristics if either the microstructure or the chemical composition is altered.

Details of the experimental method to produce monodisperse tin oxide nanoparticles are set out in Chapter 3. The important parameters are particle size, film formation and chemical composition due to the in-situ and ex-situ treatment of thin films. Additionally, the methods to characterise the material and electrical properties of undoped as-deposited and annealed nanoparticles and particle films are presented.

The material, electrical and gas-sensing characterisation results of as-deposited and annealed SnO_x nanoparticle films are described in Chapter 4. The influence of the in-situ and ex-situ process parameters on gas sensitivity and response behaviour is discussed for ethanol (C_2H_5OH) and carbon monoxide (CO) as reducing gases, and nitrogen oxide (NO) and oxygen (O_2) as oxidising gases. The relationship between the material and gas-sensing properties of SnO_2 nanoparticle layers is of particular interest.

Chapter 5 contains concluding comments.

Chapter 2

Fundamentals of metal-oxide gas sensors based on nanoparticles

2.1 Metal-oxide semiconductor gas sensors

Metal-oxide semiconductor gas sensors are used to monitor the content of oxidising and reducing gas molecules in a surrounding medium (usually air). The operational principle of such a device is to transform, directly, the value of adsorption and desorption of oxygen into an electrical signal. The electrical signal is the conductivity of the sensing layer which changes due to the attendance of different gas ambients.

Originally, gas sensors were available in the form of pellistors, whereby energy was liberated in the oxidation process of a combustible gas at operating temperatures of about 500 °C. Nowadays, chemical sensors are used in thick film or bulk form. They have migrated to thin films where they can, in principle, be combined with silicon circuitry to form an integrated system of the sensor itself, along with the electronics necessary to measure the sensor response and to provide the appropriate signal; this device is called a 'transducer'. A schematic of a measurement chain to detect gases by means of metal-oxides is shown in Figure 2.1. The chemisorption mechanism describes the reaction process resulting in a resistance change. A transducer, which consists of the gas-sensing film and the substrate including electrodes and heating elements, converts a chemical quantity into an electrical quantity for purposes of a measurement. The display shows the resistance change, i.e. the sensitivity of a given gas-sensing device. The principle gases for which

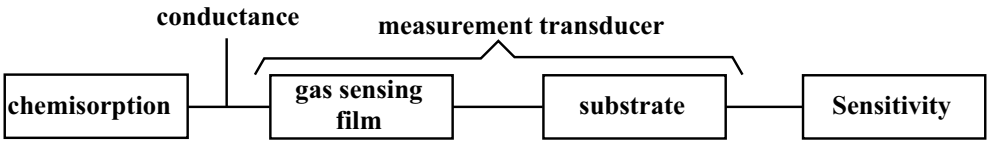

Figure 2.1: Schematic of the measurement chain for gas-sensing applications by means of metal-oxides.

this type of sensor has found most widespread application are the lower hydrocarbons. However CO, H_2, NO_x and other gases have also been measured using this technique.

The principle manner in which these sensors operate can be summarised as follows: there is a finite density of electron donors (e.g. adsorbed hydrogen) and/or electron acceptors (e.g. adsorbed oxygen) bound to the surface of a wide bandgap semiconducting oxide, such as tin oxide (SnO_2, band gab: 3.6 eV). The electron donors or acceptors cause the formation of surface states followed by an exchange of electrons within the interior of the semiconductor, thus forming a space charge layer close to the surface. By changing the surface concentration of the donors/acceptors, the conductivity of the space charge region is modulated. Göpel et al. showed a schematic representation of elementary steps in chemical sensors and catalysts with charge-transfer reactions at interfaces by using bulk oxides charge carriers [Göpel et al. [32]].

In comparison to other sensor types, e.g. electrochemical gas sensors, the production of metal-oxide gas-sensing materials is very cheap and their lifetime is longer. SnO_2, an n-type metal-oxide semiconducting material which is usually oxygen-deficient as-deposited, is one of the most investigated materials. The charge carrier transport for SnO_2 is described by means of free electrons [Zemel [94]]. Zemel demonstrated the first step in determining experimentally whether the interaction of oxygen with a film containing oxygen vacancies is fully equivalent to that arising from a classical charge-exchange-adsorption model [Weisz [88]]. Weisz assumed that a depletion region is built due to the difference between the bulk and adsorbed surface oxygen Schottky defects.

SnO_2 gas sensors can, to some extent, differentiate various gases, but are much more successful in determining the concentration of known gases. The tin oxide gas sensor does so by undergoing a resistance change which can be easily detected and either monitored or applied to actuate a gas alarm or controller for domestic, commercial and industrial use [Figaro Eng. Inc.[27]

and Ihokura et al. [39]].

The gas-sensing mechanism having SnO_2 can be described in detail via a chemisorption process combined with a charge transfer process at the n-semiconductor surface at temperatures above 100 °C. This process makes it possible to use semiconducting gas sensors having a fast and appreciable interaction of the surrounding gas molecules with the surface. At temperatures below 100 °C, the oxygen molecules are adsorbed by a physisorption process. At room temperature, the coverage of physisorbed molecules is less than one monolayer. This process is accomplished by weak van der Waals forces. The binding forces are very small (20 kJ/mol ∼ 0.2 eV per molecule) and the molecules are mobile on the surface of the semiconductor without changing their electrical properties. The low value of the physisorption enthalpy of about 20 kJ/mol causes physisorption to disappear almost totally at higher temperatures. The activation energy for diffusion jumps of physisorbed molecules is smaller than the adsorption energy. Consequently, the probability that a molecule jumps to a neighbouring site is greater than in the desorption process [Fromm [28]].

Where a metal-oxide semiconducting gas sensor is used at temperatures below 100 °C, additional equipment is required. It has been demonstrated that UV light illumination can be used to enhance the sensitivity of SnO_2 thin film gas sensors to nitrogen dioxide (NO_2) [Comini et al. [15]]. Photoexcitation can effect the charge carrier transport across grain boundaries by increasing the density of free carriers throughout the material and decreasing the intergrain barrier height. Nevertheless, this method is suitable only if a heating device cannot be integrated into the gas sensor because higher operating temperatures lead to higher sensitivity values. The dynamic behaviour is also more unfavourable using this method instead of the conventional gas-sensing device with an integrated heating system.

At higher temperatures (> 100 °C), oxygen molecules are dissociated via a chemisorption process. Firstly, oxygen is connected via dipole bonding to the semiconductor surface atoms. Under this condition, electrons are removed from the semiconductor surface via a charge transfer mechanism; this is followed by the formation of chemical bonds with the semiconductor surface atoms. The bond and activation energy of the surface reaction depends on the lattice and defect structure of the surface. Active sites for a chemisorption reaction can be normal sites, adatoms, dislocation cores or impurity atoms. The reactants can be impinging gas molecules, electrons, and atoms or defects on the regular charge or on specific sites of the substrate. The

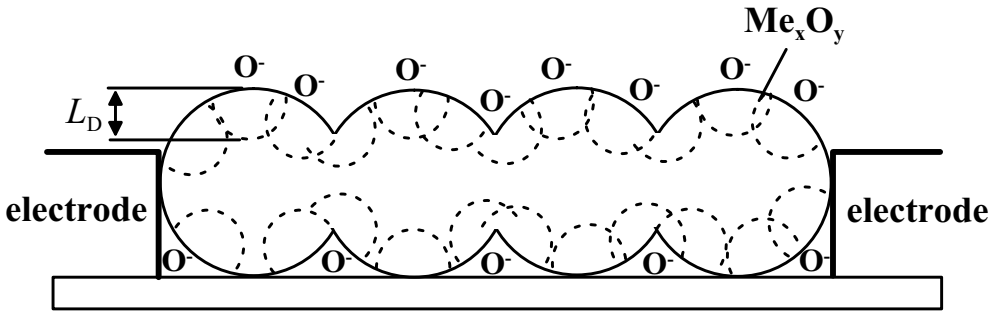

Figure 2.2: Schematic view of the formation of oxygen adsorbates on the surface of a metal-oxide semiconductor, based on monodisperse metal-oxide nanoparticles, resulting in an charge depletion region determined by L_{SC} at temperatures above 100 °C.

chemisorption species can have an electrical charge and consist of one or more atoms. In the case of tin oxide, which is the material used in this investigation, it is assumed that oxygen vacancies are primarily responsible for the chemisorption reaction. Typical chemisorption species on the surface of tin oxide are $O_2{}^-$ and O^- [Chang [8]]. The formation of these species leads to an increased resistance. A space charge region on the surface of the metal-oxide nanoparticles is built, resulting in an electron-depleted surface layer due to the electron transfer from the semiconductor surface to oxygen (Figure 2.2). The Debeye length L_D was calculated to be 3 nm at 250 °C [Ogawa et al. [67]]. Accordingly, the conductivity of the semiconductor changes inversely to the density of the chemisorbed oxygen atoms on the semiconductor surface and decreases as the oxygen partial pressure increases [Herrmann et al. [37]]. For bulk SnO_2, the thermodynamic equilibrium is generally achieved between the oxygen partial pressure and the oxygen deficiency in the SnO_2 crystal lattice at operating temperatures above 250 °C. Reducing gases (R), i.e. gases which cause a reduction of the chemisorbed oxygen on the surface of the metal-oxide, react as expressed as follows:

$$R + O^- \rightarrow RO + e^- \tag{2.1}$$

As an example, the reaction of ethanol with the surface of tin oxide is shown thus:

$$C_2H_5OH + O^- \rightarrow CH_3CHO + H_2O + e^- \tag{2.2}$$

Due to the reaction with a reducing gas, free charge carriers are replaced within the conduction band, whereas the reaction product desorbs thermally from the semiconductor surface. A lower surface coverage of the oxygen adsorbates is obtained, leading to a drop in resistance (Figure 2.3). As long as

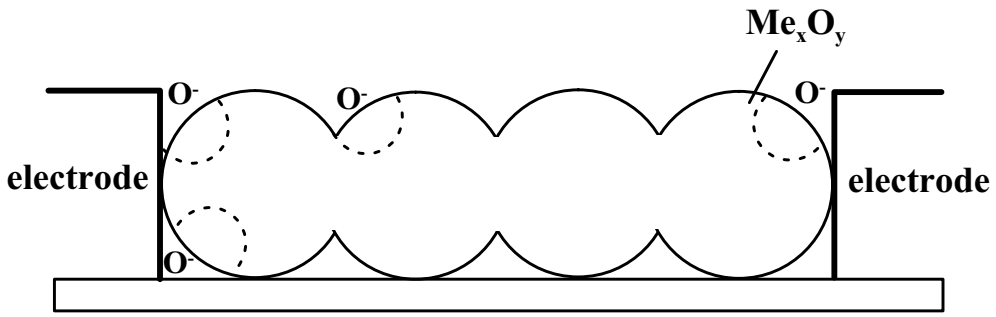

Figure 2.3: Schematic view of the sensing layer after exposure to a reducing atmosphere. The oxygen adsorbates are consumed by subsequent reactions so that a lower surface coverage of oxygen adsorbates is obtained.

the oxygen partial pressure is constant, the conductivity of the semiconductor is proportional to the concentration of the reducing gas in the atmosphere, and the gas sensor can be used for detection. SnO_2 can also react with so-called oxidising gases such as ozone (O_3), NO and NO_2. It is assumed that NO gas in the presence of oxygen in air tends to oxidise into NO_2 which can be adsorbed or can interact with the oxygen adsorbed on to the sensor surface as expressed hereunder [Capone et al. [6]]:

$$NO_{2g} + e^- \rightarrow NO_2^- \tag{2.3}$$

$$NO_{2g} + O_2^- + 2e^- \rightarrow NO_2^- + 2O^- \tag{2.4}$$

The NO gas molecules that have not reacted with the oxygen in air can, at the same time, be adsorbed on to the oxide surface; they then react with the adsorbed oxygen. In this case, the reaction will be:

$$NO_g + O_2^- + e^- \rightarrow NO_2^- + O^- \tag{2.5}$$

These reactions reduce the electron concentration and, therefore, an increase in the electrical resistance occurs.

In general, the donation of adsorbates will continue until the resulting charge transfer has raised the Fermi level of the solid to coincide with that of the adsorbate so that an equilibrium state is reached. This phenomenon will be described in more detail in Section 2.1.1.

As the processes mentioned above are mainly on the surface of a semiconductor and scarcely influence the deeper areas, semiconductor gas sensors are, nowadays, produced either out of porous sintered material or via thin film

techniques in order to achieve the highest possible ratio between depleted and undepleted areas in the sensing material after adsorption of oxygen.

2.1.1 Physical effects on the crystal surface of metal-oxide materials

As described in Section 2.1, the surface conditions for the chemisorption of oxygen lead to charged oxygen species inducing band bending in the semiconductor. The value of the surface charge changes due to a localisation of free electrons on the adsorption-related surface states. Creation of or change in the value of the charge on the surface leads to a change in the bending at the bottom of the conductivity band and at the ceiling of the valence band (Figure 2.4).

Figure 2.4(a) shows the initially neutral surface and 2.4(b) the equilibrium occupation of surface states corresponding to the chemisorbed oxygen. E_{vac} is the vacuum level; E_{C} and E_{CS} are the positions at the bottom of the conductivity band with respect to the vacuum level in volume and on the surface of the semiconductor; E_{V} and E_{VS} are the ceiling of the valence band in volume and on the surface; E_{F} is the Fermi level; E_{t} is the energy position of the surface level corresponding to the chemisorbed oxygen; eV_{s} is the value of the surface barrier caused by surface charging; χ is the value of the affinity to the electron of the semiconductor surface; $e\varphi$ is the electron work function; δ is the dope parameter which influences the position of the Fermi inside the semiconductor; and L_{SC} is the thickness of the space charge region controlling the degree of penetration of the field of surface charges into the semiconductor. In more general cases, the surface is characterised by a specific charge situated on well known surface states, resulting in the existence of an a priori surface band bending [Kupriyanov [49]]. If an equilibrium state has been reached, a surface charge eN_{s} is generated, whereby e is the elementary charge and N_{s} is the number of occupied adsorbed places on the surface. Accordingly, a charge depletion layer is built directly below the surface, the so-called space charge region. The band bending referred to above can be described by means of the Poisson equation in 1-dimensional form:

$$\frac{\partial^2 \phi}{\partial \mathrm{x}^2} = -\frac{\rho}{\varepsilon_r \varepsilon_0} \tag{2.6}$$

ρ represents the charge carrier density in the bulk; x the distance to the surface; ε_{r} the permittivity of the semiconductor; ε_0 the permittivity of the vacuum ($8.8\mathrm{x}10^{-12}$ As/Vm); and ϕ the electrical potential. The position of

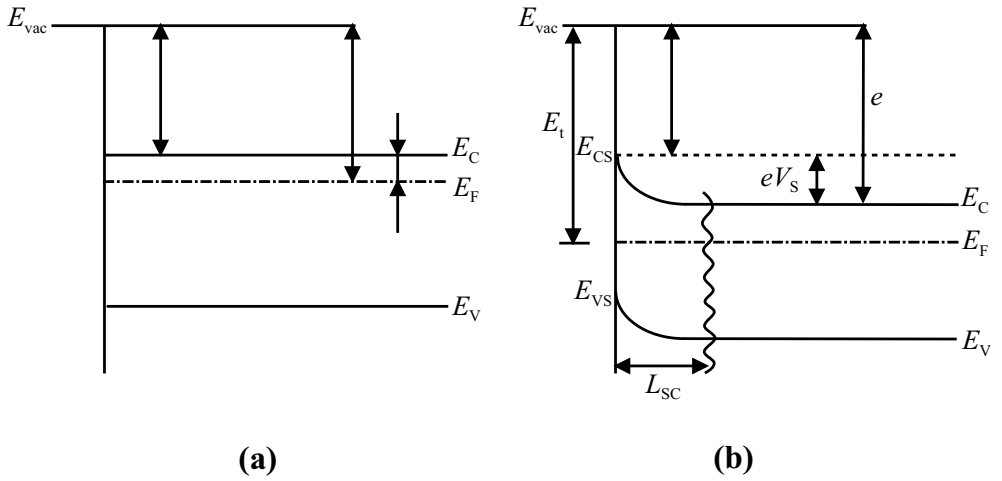

Figure 2.4: Energy bands of a semiconductor (a) before and (b) after adsorption of an electron acceptor, such as oxygen at an elevated temperature. L_{SC} denotes the thickness of the charge depletion layer at the surface.

the surface state relative to the Fermi level of the semiconductor depends on its affinity to the electrons; in this case, its affinity is high and is termed an acceptor. Accordingly, it will be positioned above the Fermi level and extract electrons (oxidising agents) from the space charge region. This band bending leads to a limitation of oxygen adsorption on the surface. As soon as the level of the surface acceptors (oxygen) reaches the electrochemical potential of the bulk, no further chemisorption processes are possible. This equilibrium process is called "Fermi level-pinning" when the resulting charge transfer has decreased the Fermi level of the solid to coincide with that of the adsorbate. Thus, the energy level of the surface state E_t defines the Fermi energy of the system and limits the value of $e\varphi$ to approximately 0.5-1.0 eV.

If the Poission equation is integrated twice, it is possible to calculate the Schottky-barrier height by taking the following boundary conditions into account, where at $x = L_{SC}$, $V = V_n$ and $dV/dx = 0$:

$$V_B = \frac{eN_d L_{SC}^2}{2\varepsilon_r \varepsilon_0} \tag{2.7}$$

N_d represents the donator density and L_{SC} the thickness of the charge depletion layer. If the Poisson equation is solved by replacing $N_d L_{SC}$ by N_s, the Schottky approximation of the surface potential is obtained thus:

$$V_B = \frac{eN_s^2 L_{SC}^2}{2\varepsilon_r \varepsilon_0 N_d} = V_s \tag{2.8}$$

The Schottky-barrier V_s describes the potential which has to be reached to have a charge transfer of an electron from the surface to the adsorbed oxgyen. As a result, the limitation of eV_s leads to a limitation of N_s, i.e. to a surface coverage limitation. Oxygen creates a maximum surface potential of $e\varphi \sim 1\,\mathrm{eV}$; its maximum surface coverage is N_d=10^{12} to $10^{13}\,\mathrm{cm}^{-2}$ (Weisz-limit) to be formed in one second, depending on the initial impurity concentration and the temperature [Weisz [88]]]. If the impurity concentration increases, the activation energy for the maximum surface coverage rate also increases.

The space charge region thickness is, typically, 10-100 nm, depending on the doping and the temperature. For SnO_2 it was determined to be in the range of 10-30 nm [Zemel [94] and Ogawa et al. [67]]. Applying equation 2.8, the thickness can be calculated as follows:

$$L_D = \sqrt{\frac{2\varepsilon_r\varepsilon_0 N_d V_s}{eN_s^2}} \tag{2.9}$$

The above equation demonstrates clearly that the thickness of the space charge region increases if the number concentration of the donator density increases. This occurss if a charge transfer takes place at the surface of the metal-oxide; this means that the charge carrier concentration at the surface and, therefore, the stoichimetry can influence the thickness of the depleted zone when the stoichiometry value indicates N_d qualitatively.

In an n-type semiconductor such as SnO_2 the majority carriers are electrons so that the change in surface conductivity $\Delta\sigma_s$ is given in the form of

$$\Delta\sigma_s = e\mu_s\Delta n_s \tag{2.10}$$

where e is the elementary charge and μ_s is the electron mobility at the surface.

The excess density Δn_s of the charge carriers in the space charge region of thickness d is obtained by integrating the difference between the electron density in the space charge region and the bulk (n_b) over the thickness d:

$$\Delta n_s = \int_o^d [n(z) - n_b]dz \tag{2.11}$$

The change in surface conductance ΔG_s is then:

$$\Delta G_s = \Delta\sigma_s \frac{W}{L} \tag{2.12}$$

where W is the width and L the length of the sample.

The bulk conductance which is not modulated by the surface reactions can be represented by a parallel conductor:

$$\Delta G_{\mathrm{b}} = n_b \mu_{\mathrm{b}} \frac{Wd}{L} \tag{2.13}$$

Subscript b refers to the bulk quantities while d is the total thickness of the oxide layer. Since the overall conductance is measured, it is advantageous to have the films as thin as possible.

The relative change in the conductance of the whole device is obtained from equations (2.10), (2.12) and (2.13) and by assuming that $\mu_{\mathrm{b}} \sim \mu_{\mathrm{s}}$. Hence:

$$\frac{\Delta G_{\mathrm{b}}}{G_{\mathrm{b}}} = \frac{\Delta n_{\mathrm{s}}}{n_{\mathrm{b}} d} \tag{2.14}$$

For a high value of the relative conductance change (high sensitivity), it is necessary to have a low density of bulk carriers and a thin film [Williams et al. [89]]. As an example, one can consider a typical value of the excess surface-state density n_s=10^{12} electrons cm^{-2} and the bulk density n_{b}=10^{17} electrons cm^{-3}. This leads, for a 100 μm thick film, to the relative conductance change $\Delta \mathrm{G}_s/G_{\mathrm{b}} = 10^{-3}$. However, if d=100 Å, the change is 10; and for thin films ($<$ 100 Å) the space charge region extends throughout the whole film thickness.

The first experiments which assumed fully depleted nanostructured sensing layers were carried out by Xu et al., who have shown that the resistance of SnO_2 in dry air at 300 °C increases steeply for crystallite sizes below 10 nm [Xu et al. [91]], particularly those with diameters below 6 nm. From these investigations, L_{D} was estimated to be $\sim$3 nm: this accords with the results calculated by means of Hall measurements [Ogawa et al. [67]]. Nevertheless, the developement of the crystallite size distribution during calcination to vary the grain size has not been demonstrated.

With respect to practical sensors, these devices are prepared by techniques which yield polycrystalline layers. For the dimensions of the film at which the surface conductance begins to dominate the overall conductance, the film morphology becomes the most important parameter. A schematic representation of three types of intergranular connection and their corresponding types is shown in Figure 2.5.

The conductivity of the different connection types is modulated by the den-

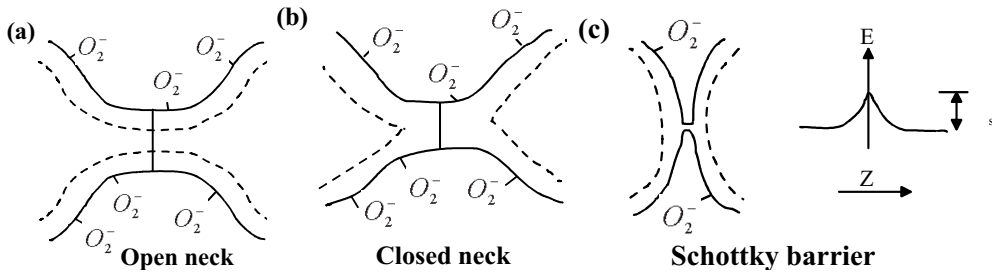

Figure 2.5: Effect of the morphology of a semiconductor oxide on conductivity. The depth of the space charge region is indicated by a dashed line. The Schottky barrier model assumes a tunnelling mechanism for the electrons.

sity of the surface states [McAleer et al. [59]]. All types assume that a sensor consists of a chain of uniform crystallites of size D connected in three different ways [Shimizu et al. [81]]. When D is less than $2L_D$, the grain resistance dominates the resistance of the whole chain and, in turn, the sensor resistance, so that the sensitivity is controlled by the grains themselves (open neck). The other two types do not allow a grain-controlled sensing mechanism; they allow only a neck-controlled or a Schottky barrier controlled mechanism. In this investigation, measurements have been carried out taking only the open neck type of connection of tin oxide nanoparticles into account.

2.1.2 The physisorption and chemisorption mechanisms

Physisorption describes an adsorption process without any change in the geometric structure and in the electrical properties of free particles or free surfaces. This process is driven by electrostatic dipole (van der Waals) forces. The physisorption potential can be characterised by a two-particle model applying of the Lennard-Jones potential which describes the attractive and repulsive forces between two particles as follows [Atkins [2]]:

$$V = E_{attr} + E_{rep} \propto 4\varepsilon\left[-(\frac{\sigma}{\mathrm{r}})^6 + (\frac{\sigma}{\mathrm{r}})^{12}\right] \tag{2.15}$$

where σ is the distance between the interacting particles, r is the atomic distance and ε is the depth of the potential cavity. If the binding energy exceeds 0.5 eV, a chemisorption process takes place.

Basically, two different chemisorption mechanisms exist [Hagen [34]]:

- molecular and associative chemisorption, where all atomic bondings are

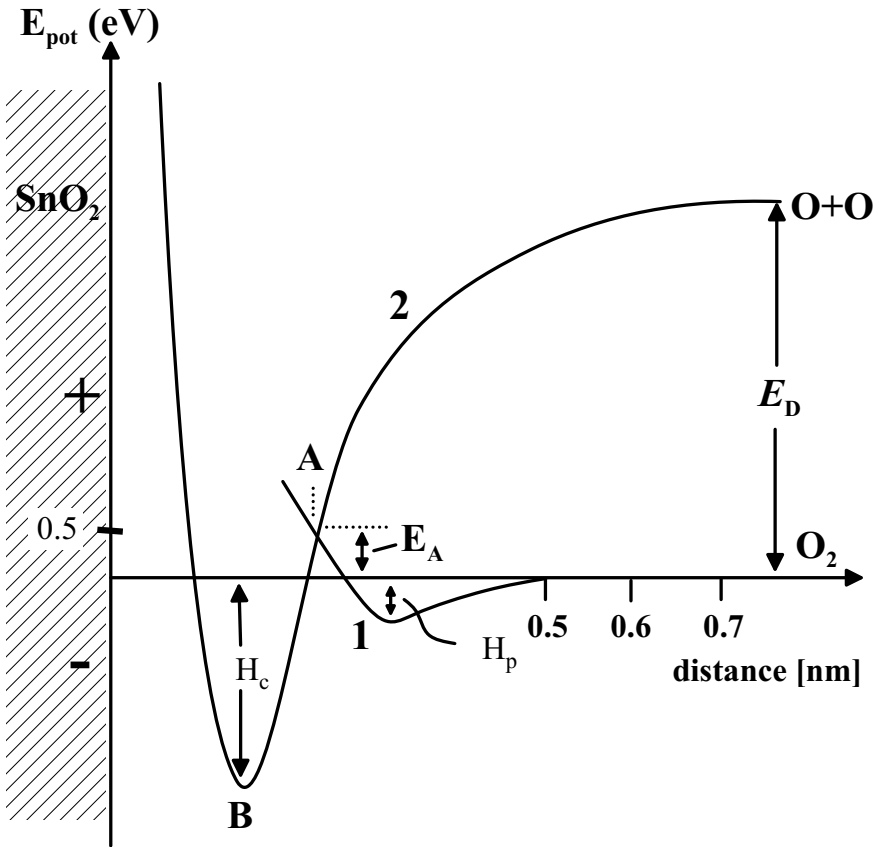

Figure 2.6: Potential energy and atomic distance at the adsorption of oxygen on tin oxide.

kept in the adsorbed molecule; and

- dissociative chemisorption, where the bonding of the adsorbed molecule is decomposed and individual molecule fragments are bonded on the metal-oxide surface.

If molecules have free electrons or multiple bonding, molecular chemisorption is then, in most cases, obtained, while molecules with single bonding react via a dissociative chemisorption. Figure 2.6 shows the potential diagram of a dissociative chemisorption of oxygen on tin dioxide [Hagen [34]]. It consists of two overlapping curves. The flat curve corresponds to the physisorption of the molecular oxygen. The molecular oxygen runs along curve 1 over the physisorption status to intercept at point A with curve 2 of the atomic oxygen, where the dissociation of oxygen starts. The chemisorption status is

separated from the physisorbed status by an activation barrier. It is possible to distinguish between both types of status via the bonding energy between the adsorbent and the surface. If the energy is above 0.5 eV per particle, it is a chemisorption; this effect is normally thermally activated. After a transition state the O-O bonding becomes weaker and a new Sn-O bonding is formed. Both atoms are bonded at a defined distance from the surface. ΔH_{p} is the free energy after physisorption and ΔH_{C} after chemisorption; E_{D} is the dissociation energy for the oxygen molecule and E_{A} the activation energy for the adsorption. The chemisorbed oxygen has the lowest potential energy and is located closest to the metal-oxide surface at B. It should be emphasised that two Sn-O bondings are developed from one chemical bonding in the oxygen molecule on the surface. The dissociative chemisorption always increases the amount of chemical bonding so that the overall process becomes exothermic.
The total process is shown schematically in Figure 2.7.

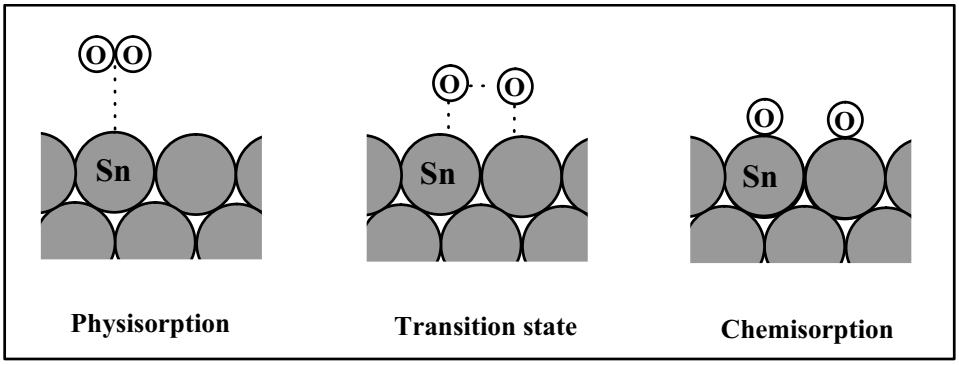

Figure 2.7: Adsorption process of oxygen on a SnO_2 surface. Two Sn-O bondings are developed from one chemical bonding in the oxygen molecule on the surface.

The desorption mechanism

Desorption is the opposite to adsorption, i.e. the chemical bonds break followed by the removal of the adsorbed atoms from the surface. This can be achieved either by thermal stimulation up to a desorption temperature or by stimulation of a specific electronic status.

If desorption is isothermal, the adsorbates solubilise on the surface at a constant temperature, due to a gradient of the chemical potential between adsorbates in the gas phase and in the adsorbed particles. For instance, it

appears that after the formation of oxygen adsorbates, the sensing layer is exposed to a reducing gas. Oxygen is consumed (desorbed) by a subsequent reaction so that a lower surface coverage of adsorbates is obtained.

2.1.3 Calculation of the surface coverage degree by the Langmuir-Isotherm

Probably the most simple model for describing the adsorption of gases on the surface of a solid material is to use the Langmuir-Isotherm which allows the calculation of the surface coverage degree Θ that depends on the partial pressure of the gas at a constant temperature (Figure 2.8). The surface coverage degree is defined by the ratio of occupied adsorbed places to available adsorbed places. The Langmuir-Isotherm assumes the following:

- the surface of the solid material has a certain number of indistinguishable adsorbed places, i.e. the adsorption takes place homogeneously without any island formation;

- the possibility of the adsorption at an adsorption place is independent of the surface coverage degree Θ; and

- the maximum coverage degree is 1, equal to one monolayer.

In an equilibrium state, identical adsorption and desorption rates are assumed; these depend on the surface coverage degree and the temperature-dependent adsorption and desorption constants k_{ads} and k_{des}. The adsorption also depends on the partial pressure p of the gas type:

$$k_{\text{ads}} = (1 - \Theta)p = k_{\text{des}}\Theta \tag{2.16}$$

If 2.16 is solved, the Langmuir-Isotherm can be calculated thus:

$$\Theta = \frac{k_{\text{ads}}p}{k_{\text{ads}}p + k_{\text{des}}} = \frac{Kp}{1 + Kp} \tag{2.17}$$

where

$$K = \frac{k_{\text{ads}}}{k_{\text{des}}} \tag{2.18}$$

At first the surface coverage increases linearly with the partial pressure of the adsorbate, then flattens and moves asymptotically to a value of 1. In the case of chemical sensors, the linear range is most important because the measured

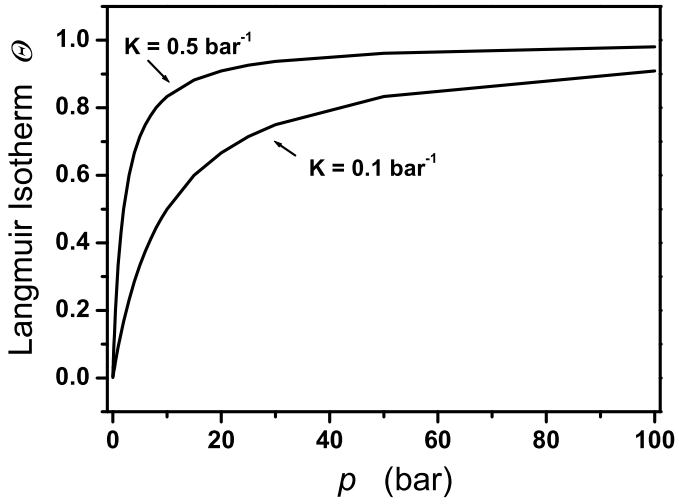

Figure 2.8: The Langmuir-Isotherm for different values of K.

effect should be linear to the gas concentration. The surface reaction process is therefore controlled by the specific surface, i.e. the contact area between each nanoparticle, and the diffusion properties of the gas molecules; this increases as the particle size decreases.

2.2 Overview of commercially available SnO_2 gas sensors

Although measurement of the change in electrical resistance during gas-sensing measurements is straightforward, there are only a few sensor fabricators. One main reason is that metal-oxide gas sensing materials do not offer sufficient long term stability. Figaro is the best known company [Figaro Eng. Inc.[27]]. In Germany, Umweltsensortechnik (UST) is a well known metal-oxide gas-sensing fabricator [Umweltsensortechnik [85]].

Figure 2.9 shows a typical basic measuring circuit for commercially available metal-oxide gas sensors. The sensor generally requires two voltage inputs: heater voltage (V_{H}) and circuit voltage (V_{C}). The heater voltage V_{H} is applied to the integrated heater in order to maintain the sensing element at a specific temperature optimal for sensing. Circuit voltage V_{C} is applied to allow measurement of voltage $\mathrm{V_{RL}}$ across a load resistor R_{L} which is con-

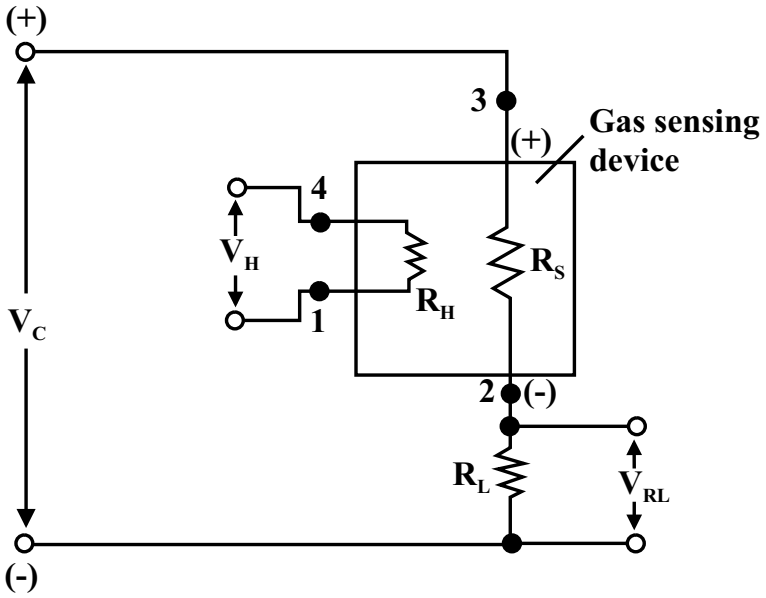

Figure 2.9: Basic circuit diagram of commercially available SnO_2 gas sensors.

nected in series to the sensor. A common power supply circuit can be used for both V_C and V_H to fulfil the electrical requirements of the sensor. The value of the load resistor R_L should be chosen to optimise the alarm threshold value, keeping power consumption (P_S) of the semiconductor below a limit of 15 mW. Power consumption will be highest when the value of R_S is equal to R_L on exposure to gas [Figaro Eng. Inc.[27]]. Contacts 1 and 4 are for heating and contacts 2 and 3 are the sensor electrodes.

Usually the size of the gas-sensing elements is approximately 4x4x1 mm and the elements are bonded into a TO-5 metal can. A typical detection range for ethanol is 50-5,000 ppm, the heater and circuit voltage is ∼5 V and the power consumption is ∼0.3 W. The sensor resistance R_S is calculated with a measured value of V_{RL} by using the following equation:

$$R_S = \frac{V_C - V_{RL}}{V_{RL}} \cdot R_L \tag{2.19}$$

The fabricators's objective is to miniaturise the gas-sensing device. Many different approaches have been tried up to now (Chapter 1.1) but, in most cases, the miniaturised devices did not fulfil the requirements for the reproducibilty and stability of the gas-sensing film. One reason is that the correlation between process parameters during synthesis, leading to certain

material structures and gas-sensing properties, is not properly understood.

The relationship between sensor resistance and concentration of the deoxidising gas can be expressed by the following equation over a certain range of gas concentration including the sensor aging or the effect of humidity.

$$\mathrm{R_S} = \mathrm{A}[\mathrm{C}]^{-\alpha} \tag{2.20}$$

whereas R_S is the electrical resistance of the sensor; A is a constant, $[C]$ is the gas concentration and α is the slope of the R_S curve [Figaro Eng. Inc.[27]].

2.3 Basic gas-sensing characteristics

In order to evaluate the quality of a sensor, sensitivity S and dynamic behaviour τ of a gas sensor are of predominant importance. Nevertheless, it is necessary to mention that these values always have to be determined in combination with the material and operating parameters, such as crystallite size, doping concentration, film thickness, operating temperature, gas type and gas concentration.

Different calculation methods have been used to determine the sensitivity and, thus, the quality of metal-oxide semiconductor gas sensors. For instance, Choi et al. [Choi et al. [12]] determined the H_2 gas-sensing characteristics of his samples by

$$S(\%) = (\frac{R_\mathrm{air} - R_\mathrm{hydrogen}}{R_\mathrm{air}}) \cdot 100 \tag{2.21}$$

Others defined sensitivity as the conductivity value in different atmospheres.

Another calculation method has been presented by Faglia et al. [Faglia et al. [25]], who calculated sensitivity towards NO_2 of SnO_2 thin films by

$$S = \frac{R_{\mathrm{NO_2}} - R_\mathrm{air}}{R_\mathrm{air}} \tag{2.22}$$

However, every calculation includes the electrical resistance value in different atmospheres. The most used method for determining sensitivity S is by calculating the ratio of the resistance of the metal oxide in air (R_a) to the resistance in a reducing atmosphere (R_g):

$$S = \frac{R_\mathrm{a}}{R_\mathrm{g}} \tag{2.23}$$

This method is used in this investigation.

The response time τ of a gas sensor is also described in manifold ways. One possibility is to define the response time as the time needed to reach 70 % of the final current value after gas introduction. The recovery time can be defined as the time needed to return to 70 % of the initial current value after recovering to a dry air flow as opposed to the operating temperature [Faglia et al. [25]]. Onother possibility is to use a 90 % response and 90 % recovery time at the time of switching the detectable gas on and off [Cukrov et al. [16], Baik et al. [3]].

In this investigation, time constant τ is determined from the measured dynamic behaviour by establishing the time at which the sensor attains 63 % of the stabilised final value of the electrical resistance after changing the concentration of the detectable gas type. This calculation is used due to an approximation of the slope of the response transients to a measuring system which has a single energy storage characterised by a differential equation of first order.

One tendency in current research in this field is to increase the sensitivity and selectivity of the surface reaction by introducing an additional catalytic control, e.g. by the incorporation of catalytic metals, metal clusters and other surface modifiers. However, for gas-sensing measurements the electrode material can affect the chemical reaction between the SnO_2 semiconductor and the sensing gas by catalytic reaction. It has been found that the electrodes may have a strong effect on the total resistance and also on the gas-sensing properties of the sensor [Lantto [50]].

In this investigation, the measurements concentrate on the influence of size and chemical composition on the gas-sensing characteristics.

2.4 Nanoparticle gas sensor characteristics

Different phenomena have been investigated to find out the reasons for size-dependent gas-sensing properties. As the gas-sensing mechanism takes place predominantly at the surface of the sensing material, the primary reasons have to be related to the surface. The first phenomenon is a geometric effect: if the particle size of the gas-sensing layer decreases, the surface to volume ratio increases; this causes an increase in the reactive surface and, accordingly, an increase in the sensitivity if the total particle layer volume is constant.

Physical effects have also a significant influence (Section 2.1). The improved sensitivity of a nanostructured gas sensor cannot be explained only by reference to the increase in the specific reactive surface; the full depletion of the metal-oxide semiconductor as the nanoparticle size approaches the thickness of the space charge region is also important [Ogawa et al. [67]]. This effect has been demonstrated experimentally by Xu et al. who found size-dependent gas-sensing properties for SnO_2 thin layers in the range of 5-35 nm [Xu et al. [91]]. Nevertheless, as already mentioned, the explanation of Xu's results cannot be carried out only by taking size-dependent causes into account because Xu et al. changed the particle size by means of changing the chemical composition (doping and calcination).

Chemisorbed oxygen species from air act as electron acceptors and lead to the formation of a depletion layer extending to the SnO_2 particles. The oxygen species also act as a surface barrier. This surface barrier is caused by the charge transfer between oxygen species and SnO_2 and also, in part, by the formation of surface states induced by the oxygen. Malagu et al. developed a model for Schottky contacts, based on the Poisson equation, for application to nanocrystalline n-type semiconductor materials [Malagu et al. [57]]. The Schottky barrier height can be established through the determination of surface states as a function of the mean grain size. At grain size values below 50 nm, the surface state density starts decreasing, and decreases further at grain sizes below 30 nm. Malagu et al. assumed that size-dependent gas-sensing properties are linked to the density of surface states induced by the chemisorbed oxygen species which leads to a lower degree of Fermi level-pinning. Less Fermi level-pinning means that the surface barrier and, accordingly, the overall resistance, can undergo large variations [Stiles et al. [82]]. This accounts partly for the increased sensitivity of SnO_2 sensing devices fabricated from nanosized particles.

2.4.1 Geometric effects: contacts and crystallinity

SnO_2 gas sensors operate generally under conditions where the overall conductivity is determined mainly by nanocrystals with a crystallite radius larger than the Debeye length L_D [Schierbaum et al. [76]]. Göpel et al. emphasised that, for practical applications, it is of great importance that SnO_2 nanocrystalline samples with crystallite diameters are smaller than the Debeye length [Göpel et al. [33]]. In particular, emphasis should be placed on preparing thin films of SnO_2 with homogeneous particle sizes in the nanometre range. There should be evidence that an atomistic understanding of conductivity

includes the description of the conduction path across grain boundaries of well controlled geometry [Göpel [31]]. Initial research has been carried out to obtain a percolation model of nanocrystalline gas sensitive layers [Ulrich et al. [86]]. As discussed in Section 2.1.1, the height of an energy barrier to an electron transport between neighbouring grains in SnO_2 is a significant factor which determines the sensitivity of the material.

The temperature dependence of the conductivity of a semiconductor can be approximated by the Arrhenius equation [Lantto et al. [51]]:

$$\sigma = \sigma_0 exp(\frac{-eV_s}{k_B T}) \tag{2.24}$$

where σ_0 is a factor that includes the bulk intragranular conductance; k_B the Boltzmann constant; T the absolute temperature; and eV_s the potential energy barrier at the interface between two neighbouring particles. The potential energy barrier is expressed via (2.8) to be

$$eV_s = \frac{e^2 N_s^2}{2\varepsilon_r \varepsilon_0 N_d} \tag{2.25}$$

where N_s is the surface density of adsorbed oxygen ions (O_2^- or O^-).

The energy barrier is a function of the temperature and atmosphere (oxygen partial pressure). Each of these parameters influences the energy barrier, the conductivity and, thus, the sensitivity. Furthermore, eV_s depends on the particle size, especially if the particle size is reduced to nanometres or to the thickness of the space charge region. Different particle sizes correspond to the different ratios of L_D compared to the radius of the particles. If the particle size is much larger than L_D the charge depletion occurs in a relatively small surface region of the particle. However, if the particle size is reduced to nanometres, the properties of all particles change dramatically due to solid-gas interactions, leading to a substantial improvement in sensor response. Thus, sensitivity depends critically on particle size. It is to be expected that both surface area and the ratio of the charge depletion region to the radius of the particle will influence sensor responses. The dependence of the energy barrier on particle size has been studied as follows [Zhang et al. [95]]: the conductivities of SnO_2 samples with different particle sizes were measured in pure argon at temperatures from 150 to 250 °C. It was found that the energy barrier decreases as particle size increases: this implies that the sensitivity of SnO_2 increases as the particle size decreases. In this investigation, sensitivity is measured directly for different particle sizes of undoped SnO_2 to demonstrate size-dependent gas-sensing properties.

2.4.2 Nanoparticle gas-sensitive porous media

Gas-sensing layers built out of nanoparticles have stimulated renewed interest during the past ten years in the gas-sensing properties of metal oxide semiconductors. One of the great advantages of nanoparticle gas sensors is that these devices are used to differentiate gases. Typical examples for SnO_2 include the detection of the refrigerant R134a (Forane) in the presence of H_2O [Delpha et al. [18]]. In work done up to now, differentiation has relied on the chemical properties of the target gas. Typical results use an array of sensors with a variety of gas-sensing materials and/or dopants [Delpha et al. [19] and Joo et al. [43]]. Cavicchi et al. have studied a selective sensor via an array of microhotplates. Using a linear ramp of temperature pulses, it was possible to identify three gases in the same measurement volume [Cavicchi et al. [7]]. First efforts to detect the gas type by means of different diffusion coefficients for different gas molecules have been carried out [Sakai et al. [74]]. It is assumed that the sensor is made from hollow cylinders of radius r and length L, where r is assumed to be much less than L_D. Using the diffusion equation of first order, together with the Knudsen diffusion coefficient, the sensing behaviour becomes dependent on the molecular mass of the target gas and, thus, can be detected selectively. The Knudsen diffusion coefficient (D_K) is expressed as follows for a straight round pore [Satterfield [75]]:

$$D_K = 9700 r_p \cdot \sqrt{\frac{T}{M}} \tag{2.26}$$

where r_p is the pore radius (cm); T the temperature (K); and M the molecular weight of the target gas (g/mol). The Knudsen diffusion can be applied if the mean free path of the gas molecule is smaller than the pore size. D_K is determined by the molecular weight when the pore size and temperature are fixed.

Nevertheless, most approaches still have a number of limitations, including an inability to detect gases that have not been programmed into the device.

2.4.3 Preparation of nanoparticle porous media for an integrated gas sensor

For thin film and nanoparticle film development, the preparation of gas sensors is combined with silicon circuitry to establish a system for the sensor itself along with the electronics necessary to measure the sensor response and provide the appropriate signal. In micro gas sensors, passivated silicon is used as a substrate on which a heater layer, an insulation layer, a pair

of electrodes, and a gas-sensing layer are stacked successively. Often the electrodes are interdigitately patterned to decrease the effective resistance of thin layers to measurable values. Park et al. developed a highly sensitive and mechanically stable microhotplate gas sensor using microfabrication and micromachining techniques [Park et al. [71]]; almost five masks were needed to produce the microhotplate gas sensor. This method could be optimised by using only three masks for the photolithographic process, combined with removing the underside of the wafer. Finally, a 95 nm thick square diaphragm was obtained [Chung et al. [13]]. Using such a thin membrane, achieved by the use of a double layer structure of 0.2 μm thick silicon nitride and a 1.4 μm thick phosphorsilicate glass (PSG), the power consumption was reduced from 55 mW to approximately 25 mW. However, a single chemical metal-oxide sensor device could not be used, up to now, to distinguish between similar gases.

Annealing of the deposited nanoparticles is essential to form conducting necks between individual particles while retaining the initial particle size. The neck growth rate $\dot{x}$ is a function of material constants, such as surface tension γ, solid-state diffusion coefficient D, initial particle radius a, and are expressed as follows [Coblenz [14]]:

$$\frac{\dot{x}}{a} = \frac{CD\gamma}{RTa^m} = (\frac{x}{a})^{-n} \tag{2.27}$$

where C is a constant, the exponent m is 3 for lattice diffusion and 4 for surface diffusion and the exponent n is 3.78 and 5 respectively. The neck growth rate is thus a function of the primary particle size. The use of particles of equal size ensures that the necks between the particles will be of comparable size. The extent of necking can be controlled through the annealing time and temperature. The annealing temperature in this investigation can be relatively low in comparison to that for other methods where the crystallite size is increased by annealing. This is advantageous when, as in this investigation, prefabricated microelectronic structures, such as interdigitated structures or heating circuits combined with thin films based on monodisperse tin oxide nanoparticles are used. Furthermore, changes, such as in the rate of grain growth during the gas-sensing process, can be prevented if the annealing temperature is the same or more than the maximum operating temperature. In most cases, the annealing temperature is approximately 100-200 °C above the operating temperature.

2.4.4 Requirements for optimisation of nanoparticle gas sensors

In general, a semiconducting metal-oxide gas sensor has to meet certain criteria: high sensitivity, good selectivity, stability and a fast response. In addition, a large measurement range (four decades) and a low detection limit (nowadays ~ 1 ppm) are required. The sensing layer should be in the form of a porous media so that as many reactive zones as possible can be reached by the gas molecules for adsorption and desorption of the oxygen adsorbates. Current research has not produced a sensing material which fulfils all requirements. One of the reasons for this is that the sensing mechanism is still not fully understood and the optimum material configuration has not yet been found. Nanoparticle thin layers offer a solution for the optimisation and understanding of the sensing mechanism of gas-sensing materials.

Size-dependent gas-sensing properties need to be properly understood. The morphology of nanostructured layers must be optimised. This can be done by providing a thin layer made out of metal-oxide nanoparticles with a very small standard deviation of the particle size distribution, i.e. monodisperse nanoparticles. A layer comprising particles of the same size would provide optimum conditions. The use of particles of equal size ensures that the necks between the particles and, consequently, the pores will be of comparable size after annealing. The annealing temperature can be relatively low in comparison to that for other methods where the crystallite size increases due to annealing. A further control and, therefore, a possible interpretation of the gas-sensing properties can be obtained if the stoichiometry and crystallographic structure (chemical composition) of the nanoparticle layer are adjustable. This means that if the morphology of the sensing film is optimised by means of having monodisperse nanoparticles, it is possible to control and to explain the gas-sensing properties of a specific material. This investigation has concentrated on monodisperse tin oxide (SnO_2) nanoparticle films as the gas-sensing material with particle sizes in the range of 10-35 nm and different chemical compositions, but keeping the film thickness constant.

Chapter 3

Fabrication and characterisation of nanoparticle gas-sensing devices

This chapter provides an overview of the synthesis and the material and gas-sensing characterisation methods for processing and investigation of thin layers based on monodisperse SnO_x ($1 < x < 2$) nanoparticles. The processing steps applied are thermal evaporation and recondensation, size fractionation and in-flight oxidation combined with crystallisation and layer formation.

Various existing SnO_2 nanoparticle synthesis methods, together with their gas-sensing characteristics, have been presented and compared in Section 1.1. In order to achieve size-dependent gas-sensing results without changing the material properties before and during the measurement, well defined and stable sensing layers are needed. For this reason, a synthesis technique used in this investigation and fulfilling these requirements has been developed. It applies aerosol technology to produce monodisperse particle size fractions of furnace-generated SnO nanoparticles using a Nano Differential Mobility Analyser (NDMA).

Before measuring the gas-sensing properties of SnO_2 particle layers of different particle sizes and different chemical compositions, it is important to characterise in detail the particle layers generated. The following material characterisation methods and their achievable nanoparticle layer information are used in this investigation (Table 3.1): a Differential Mobility Nano Particle Sizer (DMNPS), Scanning Tunnelling Microsope (STM) and Transmission Electron Microscope (TEM) are used predominately to monitor particle size distributions of as-deposited SnO_x nanoparticles.

Material characterisation method	Achievable information
Differential Mobility Nano Particle Sizer (DMNPS)	Particle size; particle size distribution
Scanning Tunnelling Microsope (STM)	Particle size; particle size distribution
Transmission Electron Microscope (TEM)	Particle size; morphology; crystallographic structure
Scanning Electron Microscope (SEM)	Particle size; morphology;
X-ray diffraction (XRD)	Mean crystallite size; crystallographic structure
Auger Electron Spectroscope (AES)	Stoichiometry of particle layer surface
Rutherford Backscattering Spectroscope (RBS)	Stoichiometry of particle layer volume

Table 3.1: Material characterisation methods for SnO_x particles and achievable information.

Scanning electron microscope (SEM) is used mainly to show the morphology of as-deposited and annealed nanoparticle layers and provides information about the design of the microhotplates used for gas-sensing measurements. Electron diffraction using TEM together with X-ray radiation from synchrotron sources, gives information about the crystallographic structure of the particles and particle layers. XRD enables also the investigation of the crystallite size and is used to characterise as-deposited and annealed SnO_x nanoparticle layers.

The stoichiometry of the particles generated is an important parameter for gas-sensing characteristics. Therefore, Rutherford Backscattering Spectroscope (RBS) was used to monitor the film stoichiometry of as-deposited SnO_x nanoparticles and Auger Electron Spectroscopy (AES) to monitor surface stoichiometry of as-deposited and annealed SnO_x nanoparticle layers; this is crucial because the main sensing mechanism occurs at the surface of the sensing material, as discussed in Section 2.1. All material characterisation methods are described in more detail in Section 3.3

The preparation of gas-sensing devices requires sufficient number of microhotplates to ensure that electrical measurements at different operating temperatures can be obtained. A detailed description of the microhotplate and microhotplate holder used is presented in Section 3.1.

In order to obtain information about the gas-sensing properties of SnO_2 particle layers and compare them with material characteristics, a gas-sensing measurement system was established. Electrical characterisation and achievable information are shown in Table 3.2. The I-V characteristic curve is used to

Electrical characterisation	**Achievable information**
I-V characteristic curve	Characterisation of electrical contact type
Resistance vs temperature	Oxygen adsorption and desorption temperature
Resistance vs time in different atmospheres	Sensitivity and dynamic behaviour

Table 3.2: Electrical characterization for SnO_2 particle layers and achievable information.

obtain information about the electrical contact type between deposited particles. The objective is to achieve an ohmic contact between the particles so that the contact type (see Section 2.1.1) will not influence the gas-sensing properties. Subsequently, the adsorption and desorption process of oxygen at the surface of the particles has to be investigated (see Section 2.1.2). This is done by measuring the resistance as a function of the temperature; the temperature at which the chemisorption mechanism appears can then be detected for different sensing layers and for different gas ambients. Finally, the principal sensor characteristics, sensitivity and dynamic behaviour, are investigated to understand and to improve SnO_2 gas sensors by recording the resistance change in the gas-sensing layer as a function of time in different gas atmospheres.

3.1 Microhotplate configurations for electrical and gas-sensing measurements

Certain microhotplates were designed to measure the electrical properties of SnO_2 nanoparticle layers at different temperatures. A distance of $2\,\mu$m between the embedded electrodes (electrode width=$2\,\mu$m) is chosen for the measurement of the electrical resistance of nanoparticle SnO_x films. The microhotplates in this investigation have an embedded layer for heating which, together with a temperature sensitive resistance (TSR), enables the temperature to be controlled. The uniformity of the particle layer is significant; thus,

the electrodes are buried. The design of the microhotplates is described in detail below.

3.1.1 Design of suitable microhotplates

The electrical characterisation of nanoparticle layers requires microhotplates with special electrode configurations. A miniaturised electrode area can help to decrease the effective resistance of the nanoparticle layer, and an embedded heating layer can reduce power consumption to reach different operating temperatures. A microhotplate with interdigitately patterned electrodes was developed in cooperation with the Fraunhofer Institut, IMS in Duisburg/Germany. The schematic diagram showing the electrode structure of these microhotplates is presented in Figure 3.1. In order to be able to make electrical measurements of SnO_x nanoparticle films up to resistance values of 1 GΩ, a 1 mm^2 structure, consisting of 160 interdigitated fingers with a width of 2 μm and identical separations, is fabricated on a chip of 3x3 mm^2. The electrodes are buried in phosphor-doped silicate glass (PSG) having a resistance much higher than that of the nanoparticle sample and viscous behaviour required for processing. The buried electrode structure is especially designed to eliminate the influence of electrode walls on the particle deposition. It has been observed that during nanoparticle deposition from the gas phase a region of low particle concentration is obtained close to the electrodes [Prost et al. [72]]. This would have an adverse affect on the electrical contact between the nanoparticle layer and the electrode materials and also destroy the uniformity of the nanoparticle layer.

A poly-silicon layer is embedded in the structure and serves as a heating element allowing a maximum operating temperature of 300 °C. Each contact window has an area of 4x4 μm^2, a distance of 2 μm to the next window and allows a maximum current of ∼5 mA. Altogether, each microhotplate has 32 contact windows for passing the current through the poly-silicon layer.

A TSR close to the interdigitated electrodes allows measurement of the microhotplate surface temperature. The microhotplate fabrication process and a detailed description of the different layers and their functions are presented in Appendix A.

To ensure reliable measurement results, the electrical resistance between the microhotplate electrodes must be a at least one order higher than the resistance of the particle layer. Consequently, the electrical resistance was measured at the maximum operating temperature of 300 °C. The resistance

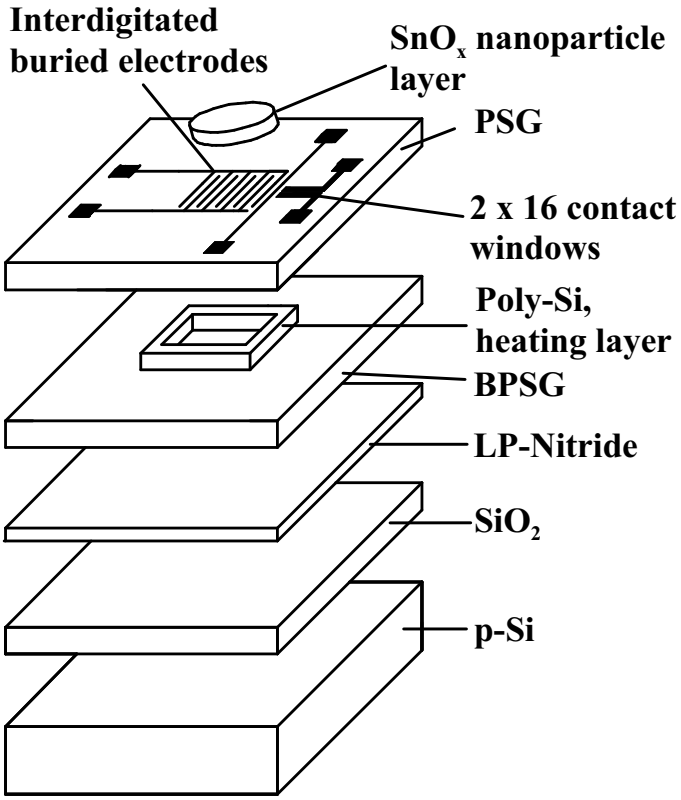

Figure 3.1: Microhotplate for gas-sensing measurements.

of the microhotplate used without deposited layer could not be measured at room temperature, thus indicating a high resistance ($> 10\,\mathrm{G\Omega}$). Figure 3.2 shows a measurement, taken over a long period, of the electrical resistance of the microhotplate without the presence of any particles. The mean resistance of the sample is about $1\,\mathrm{G\Omega}$ with a minimum value of $\sim 200\,\mathrm{M\Omega}$ at 300 °C during a measurement time lasting nearly 120 hours. Thus, the microhotplates are suitable for the investigation of high resistance nanoparticle layers below 100 MΩ at 300 °C.

Figure 3.3(a) shows an SEM micrograph of the microhotplate used, after the deposition of monodisperse SnO_x nanoparticles. The contacts for the heating layer and the TSR are shown on the micrograph. The width of the thermo channel is $2\,\mu$m and the meandering distance is $4\,\mu$m as depicted in Figure 3.3(b), including the contact windows to the heating layer. The structures are bonded to a DIL8 chip carrier in order to connect the sample to the measurement devices. The DIL8 chip carrier connector and the connection

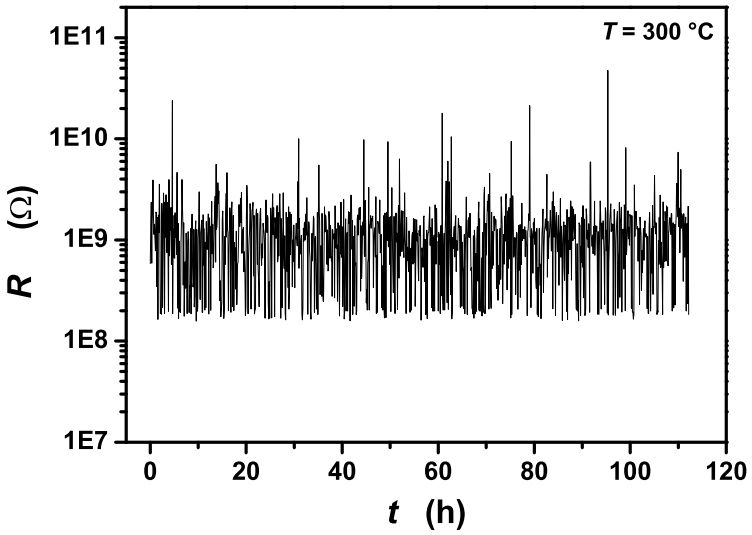

Figure 3.2: Measurement over a long period of a microhotplate without a particle layer used for gas-sensing measurement at 300 °C.

inside the measurement chamber are described in Section 3.4.2.

3.1.2 Temperature calibration of microhotplates

Operating temperature is one of the most significant parameters because both the gas-sensing characteristics and the basic electrical parameters of a given gas-sensing material depend on it. In fact, the complete gas sensor operation is based on the cyclic variation of the sensor temperature in a defined gas ambient. The temperature dependence of basic electrical parameters gives information about, for instance, the activation energy of conduction. This can be helpful in understanding the size-dependence of the electrical characteristics of the SnO_x nanoparticle samples. Thus, an accurate and reliable control of the microhotplate temperature is the key to the reliability of the gas sensor and electronic parameter measurements.

Before carrying out electrical measurements, the temperature control unit of the microhotplate is calibrated in two steps. The chip carrier, including the bonded microhotplate, is fixed together with a thermocouple on a heating plate. During annealing, the temperature of the heating plate and the resistance of the TSR are recorded simultaneously. After this external calibration, the internal heating is calibrated by recording the current flow

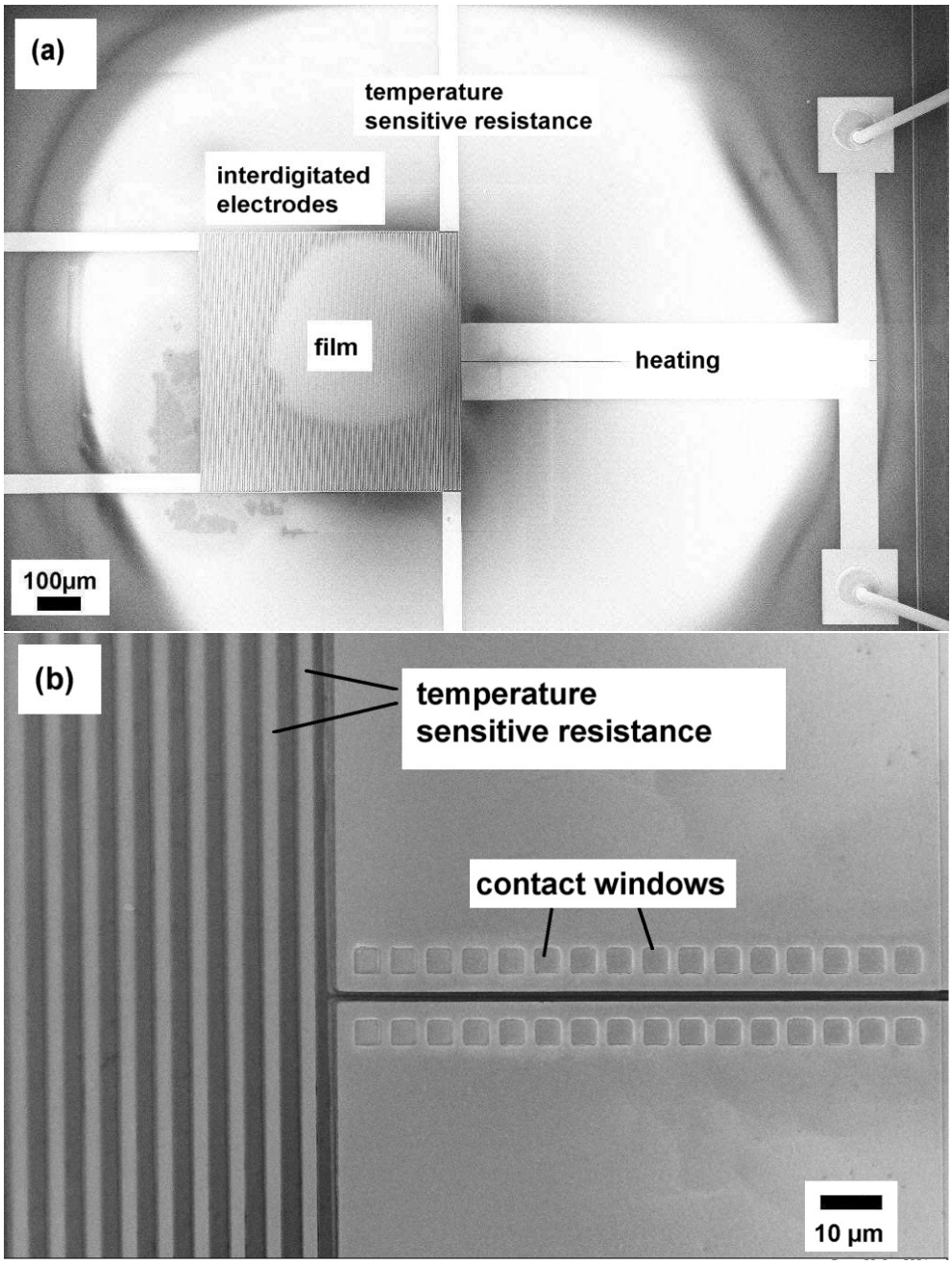

Figure 3.3: SEM micrograph of (a) the microhotplate device after deposition of monodisperse SnO_x nanoparticles and (b) the contact windows for passing the current through the embedded poly-silicon layer for heating and the temperature sensitive resistance (TSR).

through the heating layer and the temperature (resistance) of the TSR. In order to eliminate any error arising from convection cooling resulting from the gas flow, the calibration is carried out in the presence of the gas flow to be used during the measurements (150 ml/min). The resistance of the TSR as a function of the temperature shows a linear dependency in the range of 25-300 °C. Additionally, the microhotplate is heated up in a tube furnace. During heating the resistance value of the TSR is also recorded simultaneously. The maximum resistance difference between both methods is 3% at the maximum operating temperature of 300 °C, so that the temperature measurement using the TSR can be regarded as reliable.

The microhotplate can be heated up to a particular temperature by flowing the pre-calibrated current through the heating element. To illustrate: a current flow of ~ 80 mA through the heating layer of the microhotplates used in this investigation is required for an operating temperature of 300 °C. This is equal to a maximum power consumption of 4.5 W. This value is higher than the power consumption of commercial gas sensor devices due to the relatively high resistance of the poly-Si ($\sim$550 Ω) used as a heating layer (Section 2.2). The temperature of all samples can be controlled during the measurement to an accuracy of under 1 %. The typical time required for changing the temperature by 50 K is of the order of 5 minutes and the control unit waits, during this time interval, before carrying out further measurements.

3.2 Preparation of monodisperse SnO_x nanoparticle layers

The use of metal-oxide layers having well defined and stable nanoparticle sizes is a primary requirement for the fabrication of nanoparticle-based gas sensors having superior characteristics, and for understanding the size dependence of the gas-sensing mechanism. Several methods have been introduced to prepare SnO_2 nanoparticle layers (Section 1.1) and size-dependent measurements have also been done. However, no experimental investigations have been carried out up to now on size-dependent measurements without changing the microstructure of the sensing layer. Usually a calcination process is used to vary the grain size of a given layer but, as the annealing temperatures (usually 500-800 °C) change the microstructure and, therefore, the size distribution, such size-dependent gas-sensing measurements are not reliable within small size ranges. This section describes the process parameters to produce SnO_x nanoparticles with a small standard deviation of the

particle size distribution, different chemical composition and post-treatment to avoid grain growth, in the range of 10-35 nm.

The gas-phase synthesis method seems to be the most promising technique for the preparation of monodisperse tailored SnO_2 nanoparticles with different particle diameters using a NDMA (Model 3080N, TSI, Minnesota/USA). Therefore, it is possible to investigate size-dependent gas-sensing properties without any additional treatment such as calcination or doping. Adachi et al. developed an evaporation-reaction type aerosol generator for SnO_2 particles [Adachi et al. [1]]. It was found that the mean particle size can be varied by changing the evaporation temperature, but for the preparation of monodisperse nanoparticles the standard deviation values were too high ($\sigma = 1.6$). An effective method to provide well defined SnO_x particle layers is the fractionation of nanoparticles in the gas-phase using a Nano-DMA [Chen et al. [9]], as applied in this investigation [Kennedy et al. [44]]. A low pressure impactor or an electrostatic precipitator is used to deposit the size-fractionated nanoparticles.

3.2.1 Gas-phase synthesis of SnO_x nanoparticles

SnO is used as the evaporation material for the synthesis of SnO_x as it has significant advantages over Sn or SnO_2. If SnO_2 is used, large particles are formed above 1,650 °C. Below this temperature, SnO is formed by a disproportionation reaction $2SnO_2(s) \longrightarrow 2SnO(g) + O_2(g)$ which is unwanted in this investigation [Thiel et al. [84]]. Evaporation of Sn is only feasible at high evaporation temperatures due to the low vapour pressure of Sn. Also, this requires costly high-vacuum equipment because traces of oxygen will lead to the formation of SnO or SnO_2. The change in the composition of the evaporant, both with SnO_2 and Sn, leads to unreproducible and unstable results. Alternatively, since SnO has a higher vapour pressure than either Sn or SnO_2, a lower evaporation temperature can be used. This is advantageous because less impurities in the furnace walls will be incorporated in the condensed phase. It, however, necessitates, a subsequent oxidation step to SnO_2.

A gas-phase synthesis method, originally devised for the synthesis of PbS nanoparticles, was modified for the preparation of crystalline, quasi-spherical, monodisperse SnO_x particles by introducing an additional oxidation step [Kruis et al. [48]]. This method is based on particle formation by homogeneous nucleation induced by the cooling-down of the SnO vapour and subsequent aggregation by Brownian motion, followed by a size-fractionation step and a sintering/crystallisation step. The experimental set-up is presented

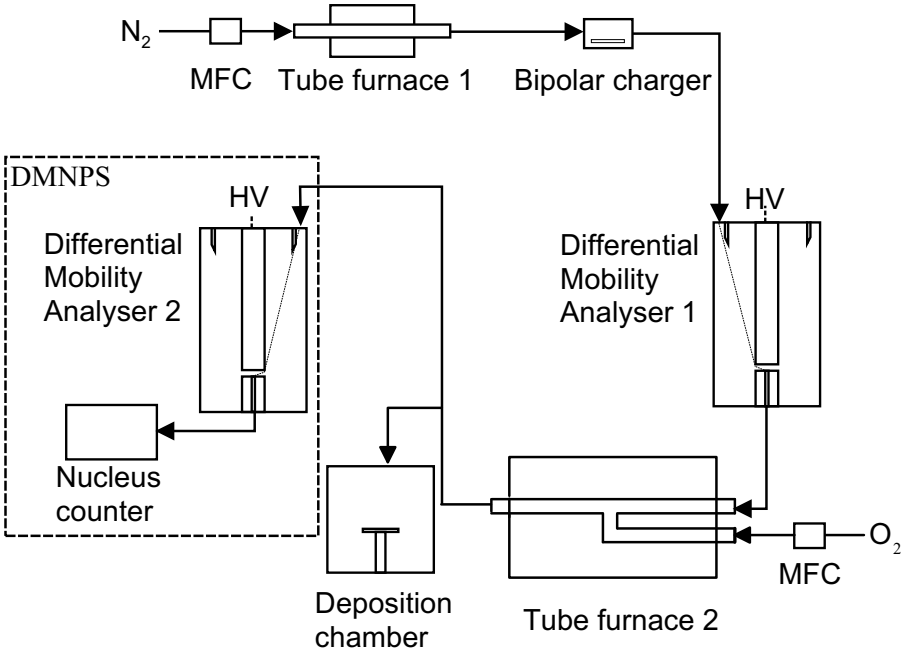

Figure 3.4: Schematic of the experimental set-up for the synthesis of monodisperse tin oxide nanoparticle films.

schematically in Figure 3.4. It contains six elements: a nanocrystal source in the form of a evaporation furnace; a radioactive β-source (Kr^{85}) which acts as a bipolar aerosol charger; the DMA used as a size-classifier; a second tube furnace for the sintering and crystallisation of the SnO aggregates; a deposition chamber; and a particle size measurement system consisting of a DMA and a condensation nucleus counter (Model 3025, TSI, Minneapolis/USA), the so-called DMNPS measurement system. The nanoparticles need to be charged as the fractionation inside the DMA is due to the existence of an electrical field [Chen et al. [9]]. As the sintered particles are still charged, a second DMA together with the nucleus counter, allows the online detection of the change in the mobility diameter arising from the passage through the second furnace. In a DMA, the charged particles are size-selected on the basis of their electrical mobility: this is a function of their charge level, size and shape. The DMA is capable of delivering monodisperse aerosols with sizes adjustable between D_{ms}=2 and 50 nm and geometric standard deviations as small as σ_{g}=1.05, depending on the flow conditions in the apparatus [Chen et al. [9]].

Nitrogen obtained from evaporating liquid nitrogen, purified by passing it

through a getter (MonoTorr PS4-MT3-N2, SAES Getters, Cologne/Germany), is used as a carrier gas. The total gas flow is kept at 1.6 l/min, the sheath air at 16 l/min by means of mass flow controllers (MFC) and the system is operated at atmospheric pressure. In the second half of the sintering/crystallisation furnace, a flow of pure oxygen is added in order to oxidise the SnO nanoparticles to SnO_x nanoparticles of $1 < x \leq 2$.

An overall view of the synthesis set-up, indicating tube furnace 1, the bipolar charger, the DMA, tube furnace 2 and the deposition chamber is shown in Figure 3.5.

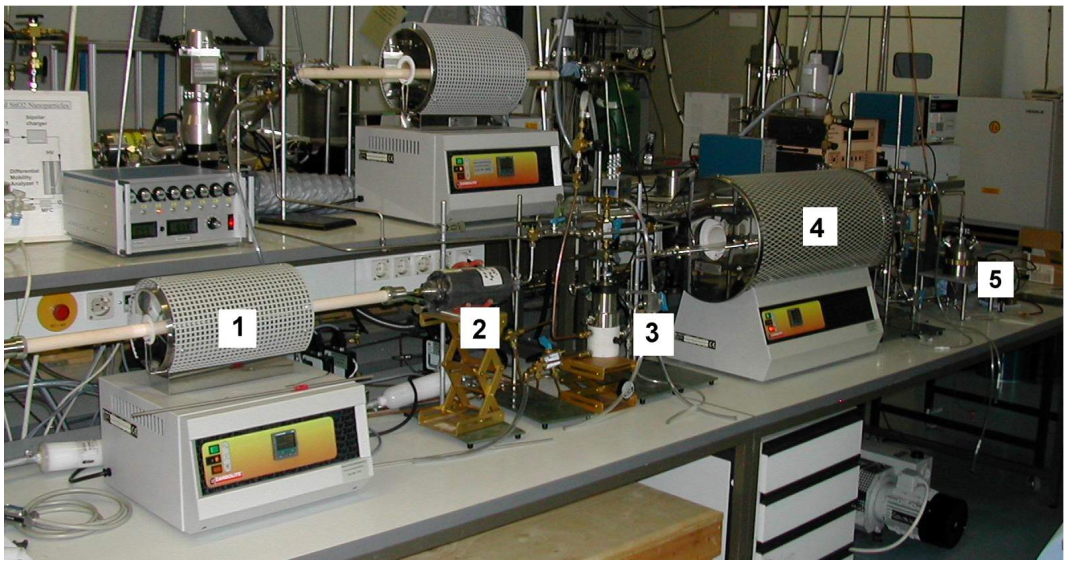

Figure 3.5: Overall view of the synthesis set-up for monodisperse nanoparticle films: (1) shows the evaporation furnace (2) the bipolar charger (3) the DMA (4) the sintering furnace and (5) the deposition chamber.

3.2.2 Deposition of SnO_x nanoparticles

For layer deposition, two methods are used: the first method requires an electrostatic precipitator having an electrical force directed mainly to the nanoparticles; the second requires a low pressure impactor increasing the velocity of the nanoparticles resulting in an inertial force.

An electrostatic precipitator enables the aerosol to be deposited with nearly 100 % efficiency on a substrate placed in a high-voltage field [Dixkens et

al. [23]]. The distance between the nanoparticle inlet and the substrate placed on the electrode at $\sim 5\,\mathrm{kV}$, is 4 cm and the area for uniform deposition is $1\,\mathrm{cm}^2$. This method is used to deposit layers for characterisation requiring larger areas, such as XRD and RBS, and for depositing nanoparticles in submonolayer thicknesses for TEM analysis. For the measurement of gas-sensitive properties, interdigitated electrode structures, having an active area of $1\,\mathrm{mm}^2$, are used (Section 3.1). For this purpose, the existing deposition method was improved for a more localised deposition than is otherwise possible in order to accelerate the deposition process. The electrostatic precipitator is, therefore, changed into a low-pressure impactor (LPI) by adding a nozzle with an inner diameter between 0.5 mm and 2 mm which is positioned 2 mm above the substrate, a critical nozzle placed above the inlet and evacuating the deposition chamber down to 1 mbar (Figure 3.6). The maximum pressure in the LPI during the deposition is 2.7 mbar.

The inertial focusing of the nanoparticle aerosol results in a deposition spot with a diameter of 500 μm when using an 0.5 mm nozzle so that a deposition area of $2\mathrm{x}10^{-7}\mathrm{m}^2$ can be assumed as a mean value. Consequently, layers with a thickness of more than 100 nm can be formed rapidly. Two window caps, together with a movable table, are necessary to control the position of the substrate below the nozzle. If a SnO_2 nanoparticle film with a particle diameter of 20 nm and a layer thickness of 1 μm is to be generated, this would need approximately 4 hours for a particle number concentration of 10^{10} particles/cm^3. Figure 3.7 shows an overall view of the deposition chamber and the window caps.

3.3 Material characterisation of SnO_2 nanoparticle layers

Material characterisation is carried out to obtain detailed information about the nanoparticles and nanoparticle layers and interpret the resultant gas-sensing characteristics. It is, thus, critical to have knowledge about the basic properties, such as the particle size distribution and morphology, the amount of deposited particles and the particle film formation, as well as the particle stoichiometry and crystallographic structure, i.e. the chemical composition. An overview of the methods used in this investigation to characterise the material properties of SnO_x nanoparticles and nanoparticle layers is provided below.

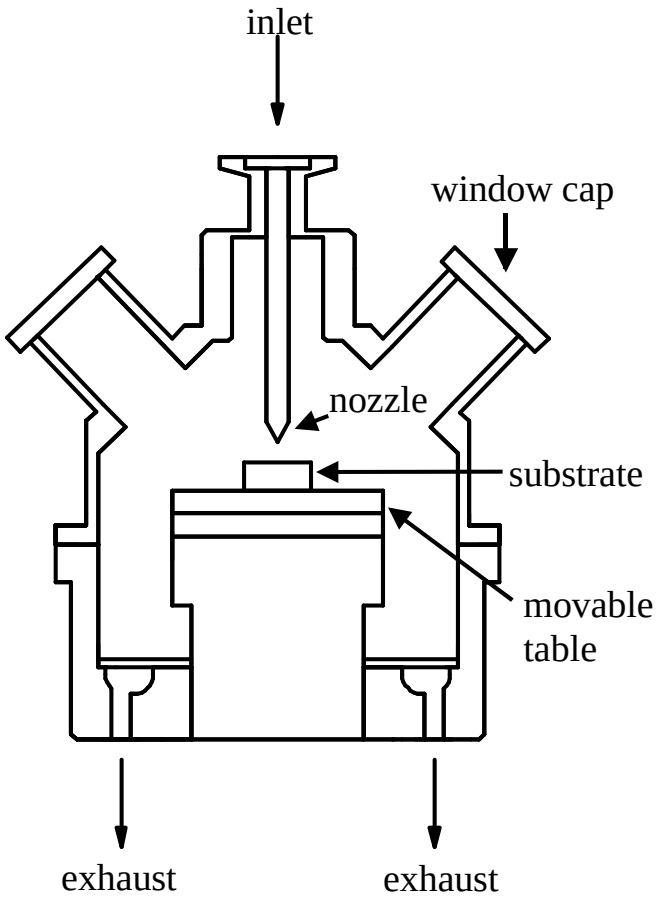

Figure 3.6: Schematic of the advanced electrostatic precipitator for a more localised deposition of nanoparticles. The window caps and movable table are needed to adjust the position of the substrate accurately.

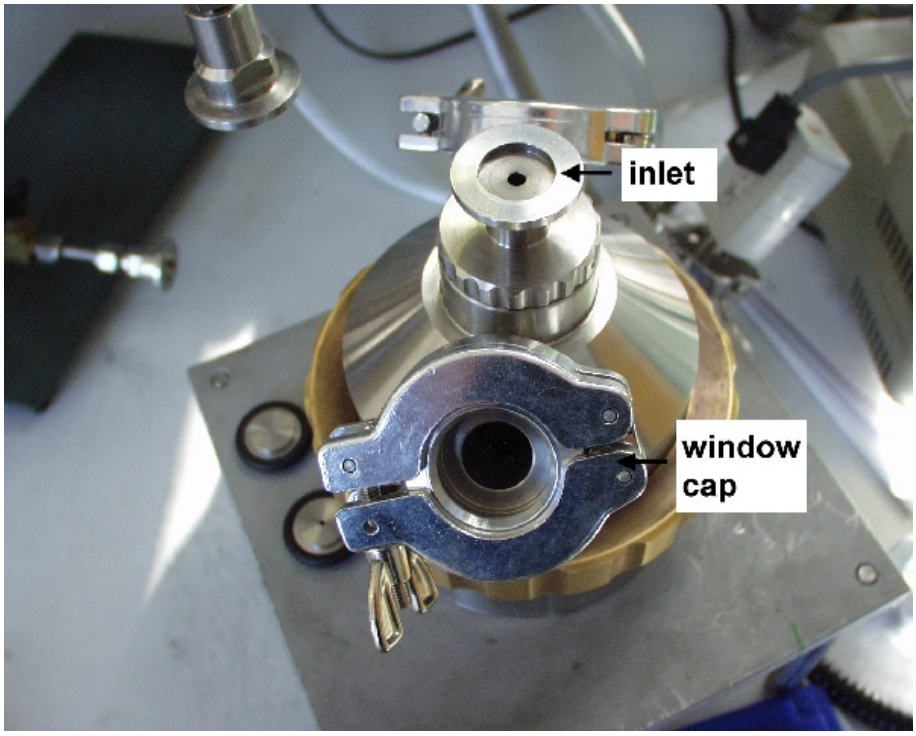

Figure 3.7: Overall view of the deposition chamber with two window caps.

3.3.1 Characterisation methods for particle size distribution

Different methods can be used to measure particle size and particle size distribution. So far, mainly Atomic Force Microscopy (AFM) work has been reported [Zhu et al. [96]]. The disadvantage of AFM is the small sampling statistic because this makes the study of size distribution difficult. In this section, four methods for analysing the particle size and size distribution used in this investigation are presented: DMNPS, TEM, STM and XRD from synchrotron sources. Electron diffraction by means of the TEM apparatus and XRD also give information about the crystallographic structure.

DMNPS can be used to measure the particle size distribution during the synthesis process. A DMNPS consists of a DMA combined with a condensation nucleus counter; the nucleus counter measures the amount of particles leaving the DMA. The advantage of DMNPS is that the particle size distribution can be obtained quasi online during the synthesis. For instance, Maisels et al. applied this method to monitor tailored nanoparticle aggregates of two components in the gas phase [Maisels et al. [56]]. Together with TEM

measurements for off-line analysis, it is possible to determine the optimum synthesis conditions for tailored nanoparticles and particle layers.

TEM investigations use electrons to measure the size, crystallographic structure and crystallinity of individual particles. TEM is used - similarly to a light microscope - to illustrate a sample. Magnetic lenses focus the electron beam arising from the Lorentz force. Electrons can irradiate through a thin layer with a thickness of less than 100 nm. Those electrons which have been Bragg reflected at the lattice planes are collected and illustrated. Usually the energy of the electrons is of the order of 100 keV. Accordingly, the deBroglie wavelength is ~ 3.4 pm. This makes very large amplification possible (factor $5x10^5$). The resolution of a conventional TEM is ~ 0.5 nm because the resolution depends on the quality of the magnetic and collection lenses. TEM measurements have become a powerful tool for describing the geometric and structural properties of nanoparticles for the development of new types of gas sensors [Jiménez et al. [41] and Diéguez et al. [21]].

In this investigation, a Philips CM12 scanning transmission electron microscope with an LaB6 cathode was used. The acceleration voltage was adjusted to 120 kV. The samples were supported on conventional carbon coated copper TEM grids. The electron diffraction results were compared to a gold reference substrate to determine the crystallographic structure.

STM images the surfaces of materials with a very high magnification so that individual atoms become visible. The principle of STM is remarkably simple: the instrument uses a sharp needle, referred to as a "tip", to interrogate the shape of the surface. The STM tip does not touch the surface. A voltage, which lies, typically, between a few millivolts and a few Volts, is applied between the metallic tip and the specimen. When the tip touches the surface of the specimen, the voltage will result in a current; if the tip is far away from the surface, the current will be zero. STM operates in the regime of extremely small distances of only 0.5 to 1.0 nm, i.e. 2 to 4 atomic diameters, between the tip and the surface. At these distances, the electrons can tunnel from the tip to the surface or vice versa.

SEM is used to study the microhotplates prepared and the particle film morphology of as-deposited and annealed tin oxide nanoparticle films. The electron beam generates different signals; these can be used for the analysis of thicker samples than those used applying the TEM method. Secondary electrons (SE) arise from the inelastic interaction near the surface; they are used to illustrate the surface topography.

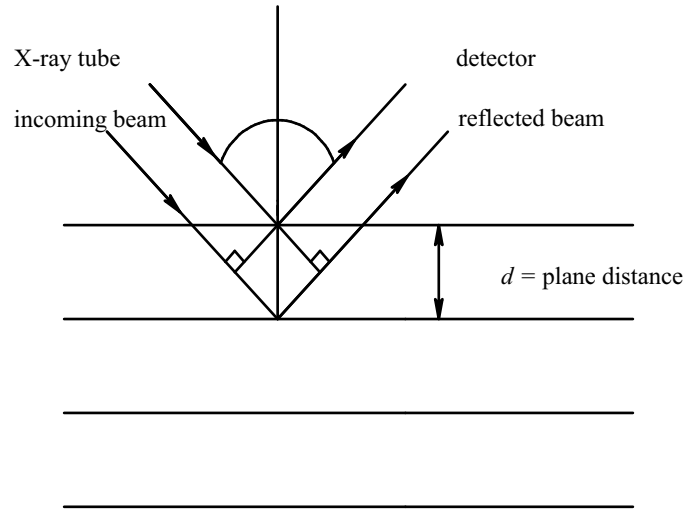

Figure 3.8: Schematic of a scattering X-ray which fulfils the Bragg condition.

3.3.2 Analysis of the nanoparticle film crystallographic structure

An alternative to the diffraction of electrons by TEM is to use X-rays to analyse crystallographic phases in layers or powders. Basically, X-ray diffraction measurements are carried out in the following way: when an X-ray beam falls on an atomic layer, two processes may occur: the beam may be absorbed with an ejection of electrons from the atoms or the beam may be scattered. The primary incident X-ray beam is scattered at parallel lattice planes at a distance d (Figure 3.8). This scattered X-ray beam can be detected. A constructive interference appears at an angle Θ if the path difference is exactly a multiple n of the incident wavelength λ. The scattering angle 2Θ is set to fulfil a Bragg condition of the lattice and the position sensitive detector (PSD) is rotated along the diffraction angles:

$$n\lambda = 2d \cdot \sin\Theta \tag{3.1}$$

By applying the Bragg principle, a diffraction in terms of a set of crystallographic planes hkl is taken into account. Strains, defects, finite size effects and instrumental resolution cause a broadening of the diffraction peaks. The width of the X-ray reflection peaks is determined by the number of the reflecting lattice planes and increases as the crystallite size decreases. The mean crystallite size is calculated by the Scherrer equation using the Bragg

peak broadening effect:

$$d = \frac{K \cdot \lambda}{\beta \cdot \cos\Theta} \tag{3.2}$$

where d is the mean crystallite size; K is a grain shape dependent constant (here assumed to be 1); λ is the wavelength of the incident beam; Θ the Bragg reflection peak; and β the full width of half maximum. The measured Bragg peak width value consists of the full width of half maximum β and a value b given by the resolution of the diffractometer. b is determined by a diffraction phenomenon at the aperture:

$$\beta = \sqrt{(b^2 + \beta_{\text{real}}^2)} \tag{3.3}$$

It has been demonstrated that the strain and shape of quantum dots can be separated by means of grazing incidence X-ray scattering. In this case, the intensity along the angular direction at different positions is analysed [Metzger et al. [61]]. If the diffraction peak broadening has a Lorentz profile, this is caused mainly by crystallite size effects. A Gauß profile would indicate microstrains inside the crystal lattice [de Keijser et al. [17]]. X-rays from synchrotron sources have the advantage that the incoming beam has such a high energy that the measurements can be done on small amounts of nanoparticle layers.

In this investigation, $\Theta/2\Theta$-scans of gas phase synthesised monodisperse SnO_x nanoparticle films on silicon substrates are measured under a gracing incidence angle of 1°. X-ray diffraction from synchrotron sources at the European Synchrotron Radiation Facility (ESRF) in Grenoble/Switzerland was carried out (incoming beam energy 8 keV) with different mobility-equivalent diameters in the range of $D_{\text{ms}} = 8$-25 nm after in-flight sintering. As-deposited nanoparticles as well as annealed nanoparticle layer were investigated. The mean crystallite size was compared with the TEM, STM and DMNPS results.

3.3.3 Study of nanoparticle volume and surface chemical composition

The chemical composition of tin oxide nanoparticle samples is investigated to obtain information about the chemical and structural evolution of the synthesised particles. This information can be used to explain the effects of the in-situ and ex-situ treatment of the gas-sensing properties of tin oxide nanoparticle thin films.

In this section, two different methods are introduced: AES to measure the

chemical composition on the surface of the nanoparticle films and RBS to obtain information about the volume stoichiometry. The surface stoichiometry, in particular, is a significant parameter because the ratio of oxygen atoms to tin atoms gives information about the number of oxygen vacancies, i.e. the amount of reactive zones, if the crystallographic structure is known. The chemisorption process was mentioned in Section 2.1.2. If the oxygen content of a metal-oxide semiconductor decreases, where there is a stable lattice structure, the number of reactive places increases.

Analysis of the surface stoichiometry

AES is a powerful tool to identify the elements present and the concentration on the surface of conducting and semiconducting solid samples. AES characterises the top 10-50 Å of the material with detection limits of 0.25 atomic%. The Auger process is a multi-electron process which involves transition between the core and valence energy states. It can be summarised in the following manner: a focused beam of electrons (2-25 keV in energy) is used to excite atoms on a solid surface, generating an initial core hole (K or L shell). Both primary and core electrons leave the system with well defined energy, whereby the escaping primary electron loses its memory due to the complexity of the scattering process. The electronic structure of the ionised atom rearranges itself so that the initial hole in the core level is filled by an electron from a higher-energy shell. The relaxation process of this atom can be accomplished either by the emission of a characteristic X-ray photon (X-ray fluorescence) or through a radiationless Auger transition in which the energy gained by the electron that "falls" into a deeper level is transferred to an electron in the same or different shell. The later electron is then emitted with a characteristic Auger energy, leaving the atom in a double ionised state (two holes at different or the same core levels). This electron carries a well defined energy used to identify that atom. All elements, except hydrogen and helium, can emit an Auger electron.

To determine the surface stoichiometry, the samples are transferred under ambient atmosphere to an ultra high vacuum chamber for electron-induced AES. The base pressure in the analysis chamber is below $1{\cdot}10^{-9}$ hPa. AES spectra are recorded in the first derivative mode and the energy of the primary electron beam is adjusted to 3 keV. The oxygen stoichiometry is estimated from the ratio of the Auger peak-to-peak heights of the O(KLL) line at a kinetic energy of 510 eV and the low-energy feature of the Sn(MNN) doublet at 421 eV. An AES spectrum of sintered SnO_2 powder is used as a calibration reference for determining the SnO_x nanoparticles oxygen content.

For in-flight oxidation of SnO particles, oxygen is supplied to the carrier gas flow at concentrations of 10, 20 and 35 vol% at the sintering stage. The SnO particles are then collected on to a small spot of 1-2 mm in diameter on a Si(111) substrate in the deposition chamber at room temperature applying the LPI method. The Si substrate is etched with hydrofluoric acid to remove the native oxide (Section 3.2.2). However, a small amount of oxygen contamination is still observed.

Post-annealing of the samples occurs at 300 °C for 1 hour in a continuous flow of synthetic air (20 vol% oxygen; 80 vol% nitrogen). After the annealed samples are measured by AES, they are once again annealed under the same conditions to study the variation of the oxygen stoichiometry resulting from the multiple heat treatment. The post-annealing parameters are selected to match the working conditions of typical SnO_2 gas sensors.

Analysis of layer stoichiometry

The stoichiometry of SnO_x nanoparticle films is detected by means of RBS. It is a non-destructive method where irradiation of the sample with light ions (projectiles, H^+ or He^+) and detection of the elastically backscattered projectiles at large angles take place. RBS gives information about the depth profile and density of thin films [Nagel et al. [62]]. The mass identification of the target atoms in the sample results from the energy of the backscattered projectiles, typically measured by means of a surface-barrier detector. The thickness of the layer and concentration profile are determined from the energy difference between the backscattered projectiles and the corresponding maximum energy for the scattering of surface atoms given by the kinematical factor k_p:

$$E_1 = k_\mathrm{p} E_0 \tag{3.4}$$

where E_1 is the energy of the backscattered ion and E_0 is the energy of the accelerated projectiles. The kinematical factor can be calculated thus:

$$k_p = \Big[\frac{M_\mathrm{p}/M_\mathrm{r}\cos(\theta) + \sqrt{1-(M_\mathrm{p}/M_\mathrm{r})^2\sin^2\theta}}{1+M_\mathrm{p}/M_\mathrm{r}}\Big]^2 \tag{3.5}$$

where M_p is the mass of the projectile (in this work H^+-ions); M_r the mass of the corresponding element; and θ the backscattering angle.

In this investigation, RBS measurements were carried out using He-ions with an energy of 3.05 MeV. Glassy carbon was used as the substrate material. The investigations were done with as-deposited unoxidised and with

10 vol% oxygen in-situ oxidised SnO_x nanoparticles with a mean particle size of D_{ms}=20 nm. An element depth profile of the atoms was determined by means of the fit program "Rump" [http://www.genplot.com/]. This program is an RBS plotting, analysis and simulation package.

3.4 Basic electrical parameter and gas-sensing characterisation of SnO_2 nanoparticle layers

Measurement of the gas-sensing and electrical properties of nanoparticle layers produced in the gas phase, requires a porous media with measurable resistance values. Therefore, the nanoparticles are deposited by means of a low pressure impactor (Section 3.2.2). This method ensures a relatively short preparation time. Furthermore, special microhotplates with an interdigitated electrode pattern area in the size range of the particle deposition spot, are designed (Section 3.1.1). The gas-sensing mechanism occurs predominantly at temperatures above 150 °C (Section 2.1). With the aid of a TSR, the temperature can be controlled by a personal computer on the microhotplate itself. The gas-sensing device is put in a measurement chamber to achieve a well defined atmosphere.

Different kinds of gas sensor testing systems with different degrees of complexity have been reported [Endres et al. [24] and Harvey et al. [36]]. In this investigation a measurement system, to be used for measuring both the parameters for gas sensor evaluation and the basic parameters for understanding the gas-sensing mechanism, has been designed and fabricated. Gas-sensing measurements are carried out time-dependent in different gas atmospheres (all gases are humidity-free and diluted in synthetic air) and at different operating temperatures.

Prior to gas-sensing measurements, the SnO_x nanoparticle films are annealed at a temperature of 300 °C for about 2 hours in 1,000 ppm ethanol in synthetic air. The annealing results in the formation of well defined sintering necks so that the nanoparticle structure does not alter during the measurement cycles if the operating temperature is below or equal to the annealing temperature (Section 2.4.2).

In order to obtain information about the chemisorption process, SnO_2 particle layers with different particle sizes are heated at 150-300 °C in atmo-

spheres with various oxygen partial pressures (95 mbar-490 mbar) analogue to Herrmann et al. [Herrmann et al. [37]]. The measurements are carried out to study the semiconducting behaviour of the nanoparticulate sample exposed to the oxygen ambient. For this, the resistance of the sample is recorded as a function of time at a particular temperature. Once the resistance value stabilises, the temperature is decreased by 25 °C and the measurements are repeated in the same manner. These precautions are essential to ensure that the resistance variation represented the semiconductor nature of the sample and the adsorption of the gas molecules. The exponential variation of $1/R$ with the temperature provides evidence of the semiconductor character of the SnO_2 nanoparticle film. The next step is to determine at which temperature the chemisorption mechanism takes place. The samples are, accordingly, annealed at constant heating rates of 6 °C/min in different gas atmospheres (synthetic air, ethanol and NO) and their resistance behaviour as a function of the temperature is compared. Finally, sensitivity and dynamic behaviour are compared for different particle size, stoichiometry, crystallographic structure, operating temperature, gas type and gas concentration to investigate the influence of the changes in the process parameters leading to different material properties. One of the main aims of the set-up used is to achieve a maximum automation of the measurement facility.

3.4.1 Measurement set-up for electrical and gas-sensing characterisation

A block diagram of the complete instrumental configuration with the switching device and the interconnections is shown in Figure 3.9. For measurements concerning the I-V, sensitivity and dynamic behaviour of a gas sensor, a picoammeter (model 487, Keithley Instr./Germany) with an internal voltage source is used. The instruments are connected via an IEEE-488 bus to the computer. The set-up can be used to measure gas-sensing characteristics in well defined temperature cycles and gas concentration levels [Kennedy et al. [45]]. Figure 3.10 shows an overall view of the gas-sensing measurement system. The important features, such as the measurement chamber, gas delivery system and picoammeter are indicated in the picture.

Gas delivery system

The schematic details of the gas delivery system, including the magnetic valves (MV), three mass flow controllers (MFC) (maximum flow rate: 10, 100 and 500 ml/min) for the analysing gas and one MFC for dry synthetic air (500 ml/min), is presented in Figure 3.11. This MFC is used either for

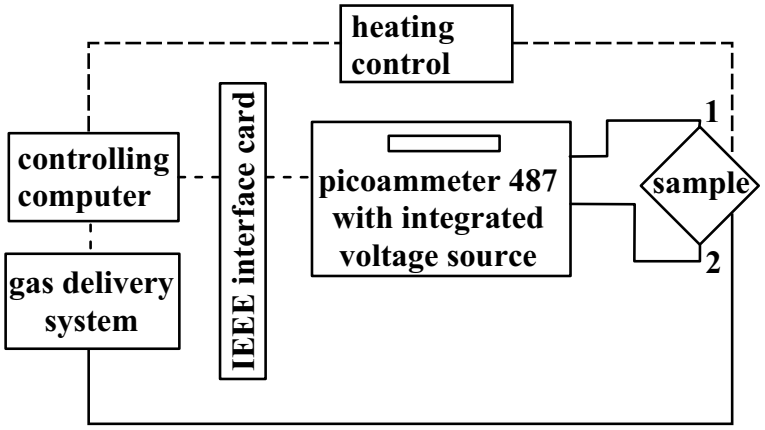

Figure 3.9: Schematic diagram of the I-V and gas-sensing measurement system.

the regeneration reaction process or to dilute the detectable gas. The unit controls the MFCs and magnetic valves; the gas concentration can be adjusted within the range of 10 to 1,0000 ppm depending on the initial gas concentration supplied.

Gas-sensing measurement chamber

Gas-sensing measurements require defined atmospheres. Consequently, the gas must be introduced into a defined reaction volume. This volume is assured by a closed measurement chamber. Figure 3.12 shows the measurement chamber with separate feedthroughs for preparing the electrical connections for resistance measurement and for heating and temperature control. All the connections to the measurement chamber, except the wires used for the heating control, are made from shielded triax cables; shields are earthed. The feedthroughs allow the measurement of resistivity values up to $10^{10}\,\Omega$cm. The measurement chamber, with a diameter of 100 mm and a reaction volume of 120 cm^3, is fabricated out of aluminium. The chip carrier is inserted into a chip socket, as indicated in Figure 3.13. Below the circuit board are conductor paths which are soldered to the heating control and picoammeter. During the measurement a constant gas flow of 150 ml/min is maintained in the chamber.

Automation of gas-sensing measurements

One of the main aims of this project is to achieve a maximum automation of the measurement facilities. Gas-sensing measurements normally require

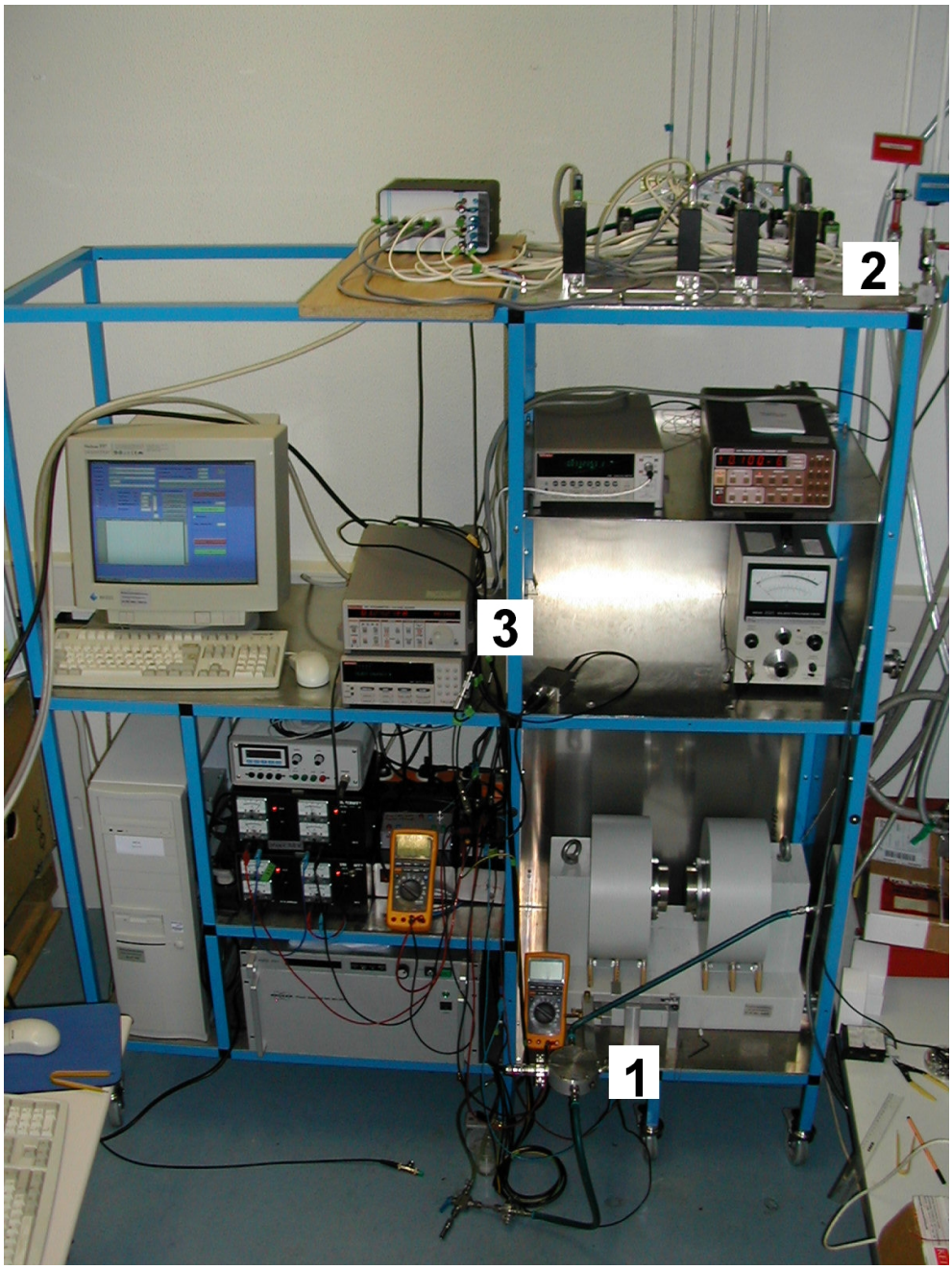

Figure 3.10: Overall view of the measurement set-up for the electrical and gas-sensing characterisation of SnO_2 nanoparticle layers: (1) shows the measurement chamber (2) the gas delivery system and (3) the picoammeter.

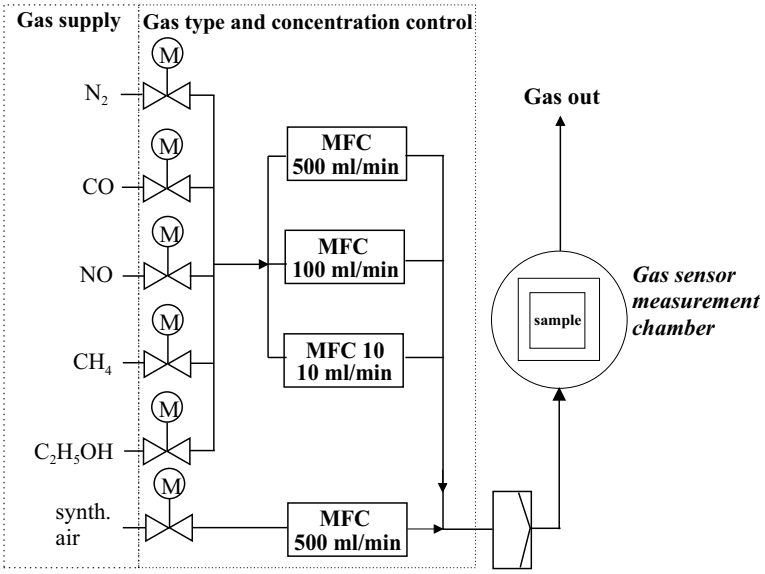

Figure 3.11: Schematic presentation of the gas delivery system. All gases are diluted in synthetic air.

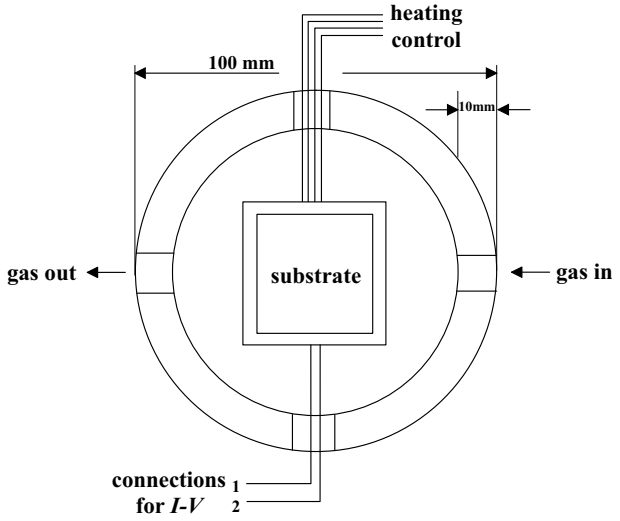

Figure 3.12: Schematic diagram of the measurement chamber.

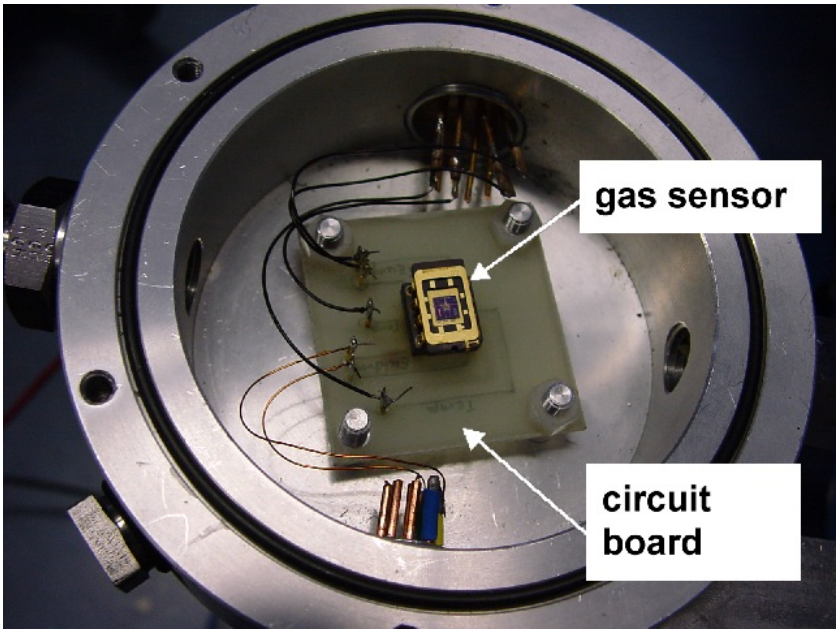

Figure 3.13: Overall view of the measurement chamber. The chip carrier is inserted into a socket. Below the circuit board are conductor paths.

long time (several days); by using the set-up described in this investigation, the measurements are carried out in a pre-set gas ambient and temperature cycles without the need of an operator. A measurement control program was implemented using the LabVIEW^{TM} 5.1 software (National Instruments, Austin,Texas/USA). A virtual instrument, having data acquisition, processing and storage capability for the semiconductor gas sensor data, was developed. It allows an easy control of the different experimental conditions used in gas sensor characterisation such as the I-V characteristic, sensitivity and response time measurements. A dedicated user-friendly front panel was developed.

An interface to follow the measurement is depicted in Figure 3.14. Indication of the status of the measurement and the real time display of the gas flow, temperature and current on an Excel file format-save option are some of the facilities. Similar graphical interfaces are also included in the software to control the calibration of the heating and measurement routines. To run the measurement, the user has to follow several options in the program:

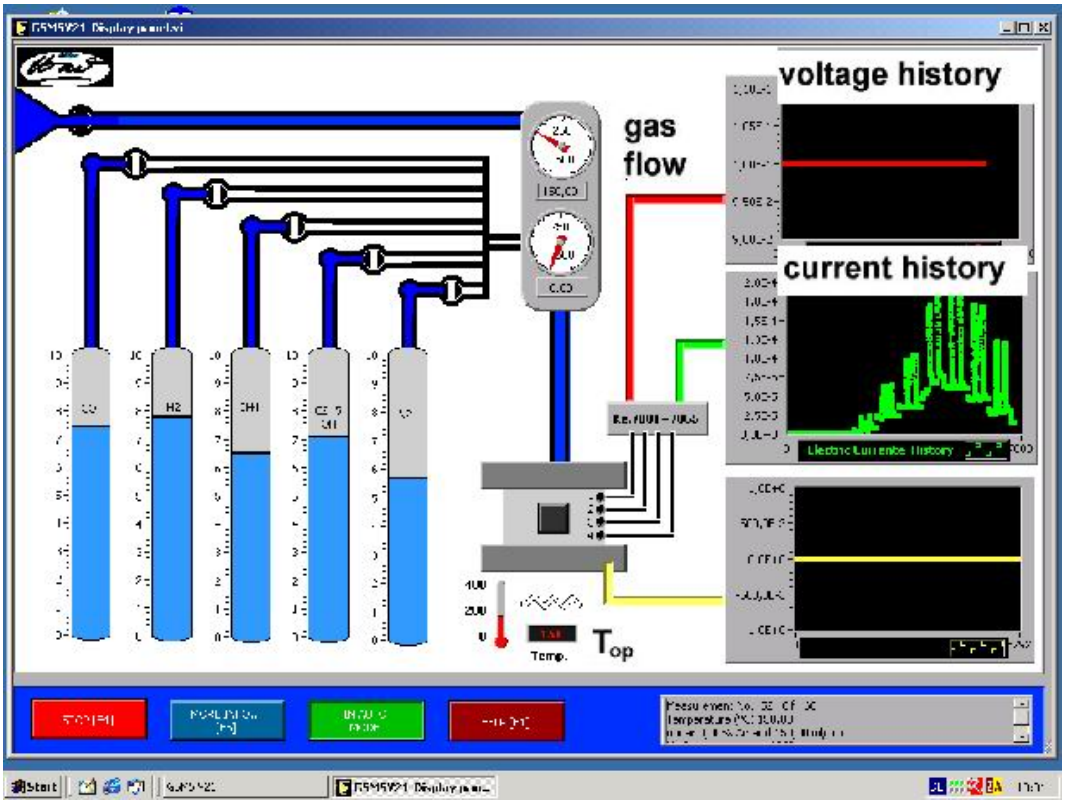

Figure 3.14: Graphical user interface of the instrument. The depicted interfaces show the voltage, current and resistance as functions of the time. Gas flow and operating temperature during the measurement are also shown.

1.	Entering the measurement parameters
1.1	Set gas type, gas concentration and gas flow
1.2	Set operating temperature
1.3	Set measurement type (I-V, sensitivity, response behaviour)
1.4	Set current and voltage
1.5	Set number of cycles
2.	Measurement runs
2.1	Online operating temperature, gas type, concentration and flow indicator
2.2	Online indicator for voltage and measured current
2.3	Online measurement type indicator
3.	Data processing
4.	Finish

All of these options are included in one program. Before an option is exercised, the measurement program asks what the laboratory temperature is in order to adapt the resistance of the TSR to the ambient temperature. Options 1.1 - 1.5 have to be entered in an extra window; options 2.1 - 2.3 can be followed on the screen. At the beginning of the process, the user is prompted for a file name, comments concerning the sample and any instructions as to the location to which stored data is to be sent. Upon selecting the options, the user must enter a new test sequence manually at every new measurement fraction. The operator is prompted to enter the required temperature and atmospheric conditions and ranges of each cycle. The total number of cycles is unlimited. For illustration purposes, a typical sequence for a gas-sensing measurements is shown in Table 3.3. It is essential to purge the tubes and

Type	**U** (V)	**T** (°C)	**Gas**	**Conc.** (ppm)	**Flow** (ml/min)	**Meas.** (No.)	**Meas. time** (ms)
response	0.1	300	air	0	150	500	[5,000]
response	0.1	300	ethanol	1,000	150	250	[5,000]
response	0.1	300	air	0	150	500	[5,000]
response	0.1	300	ethanol	1,000	150	250	[5,000]
response	0.1	300	air	0	150	500	[5,000]
response	0.1	300	ethanol	1,000	150	250	[5,000]

Table 3.3: Typical measurement sheet for the investigation of gas-sensing properties.

the measurement chamber volume before its commencement to ensure stable experimental conditions; adequate purging of the system is achieved by allowing nitrogen or synthetic air without any humidity to flow for a minimum period of 30 min. The resistance measurements are carried out on highly resistive SnO_2 nanoparticle films grown via the LPI method.

3.4.2 Typical gas-sensing measurement analysis

A typical analysis for determining the gas-sensing properties of a metal-oxide material is achieved by recording the electrical resistance versus time after changing the gas ambient. The resulting response transient is used to obtain sensitivity S and response time τ of the gas-sensing layer. The definition of sensitivity S is described in equation (2.23) and the analysis of the dynamic behaviour is discussed in Section 2.3. For the sensor characteristic both, the response time after changing the gas ambient and the response time for recovery, are of importance.

For illustration purposes, Figure 3.15 shows a response transient where sensitivity and dynamic behaviour are indicated. If different sensors are compared,

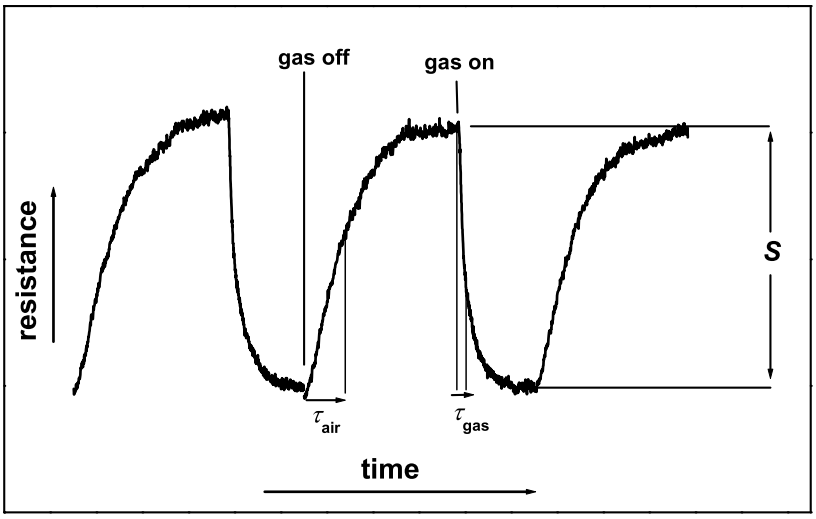

Figure 3.15: Typical response transient to characterise the sensing properties of a metal-oxide gas sensor. The important analysing parameters, sensitivity S and time constant τ, are indicated.

additional information, as discussed hereunder, is required. To investigate the gas-sensing properties of a specific gas sensor, the response transients are measured at different operating temperatures to find the optimum working temperature in a specific atmosphere for a specific material. Furthermore, gas-sensing investigations can be carried out for different gas types and material properties, such as particle size, layer thickness, crystallographic structure and stoichiometry. The compound of all measurements provides information which is necessary for the understanding of material structure dependent gas-sensing properties under different circumstances and for the optimisation of gas-sensing characteristics. Tin oxide nanoparticle layers, with a small standard deviation of the particle size distribution in the range of 10-35 nm, are used. The nanoparticles are treated in-situ during synthesis and ex-situ after deposition to increase knowledge about the influence of the material properties referred to this section.

Chapter 4

Material and gas-sensing properties of SnO_X nanoparticle films

In this Chapter, the results concerning the investigation of the SnO_2 nanoparticle and nanoparticle film structure depending on the process parameters using the synthesis method described in Section 3.2.1 are shown. Electrical parameters as well as gas-sensing properties of tin oxide layers based on monodisperse nanoparticles are presented and discussed. Combining knowledge of material characteristics and gas-sensing properties makes it possible to fabricate tailored gas sensors.

4.1 Influence of the process parameters on SnO_x nanoparticle formation

DMNPS and TEM measurements are used to study size-fractionation and the effect of in-flight sintering on particle size and morphology. The particle layer formation is studied by means of STM and SEM. The investigation of the chemical composition of SnO_x nanoparticle volume and surface due to in-situ and ex-situ processes is carried out by means of TEM, RBS and X-ray diffraction using synchrotron sources. Of particular interest is the variation of the surface stoichiometry using different process parameters. Accordingly, AES measurements are carried out. Furthermore, the change in the chemical composition, due to a post-heating treatment in synthetic air, is investigated.

4.1.1 Analysis of the SnO_x nanoparticle and nanoparticle film formation in the gas phase

The evaporation-condensation mechanism for the synthesis of SnO_x nanoparticles is tested with respect to its stability as a function of time. It is found that the number concentration of particles produced remains stable, within a 10 % variation for several consecutive days. The evaporation material in the evaporation boat can be used for weeks without replacement because of the small evaporation rate required to produce particles in the nanometer size range. The evaporation temperatures which are found to be necessary for obtaining aggregates in the desired size are achieved at 700-900 °C. The in-flight sintering temperature varies between 645-670 °C, depending on the selected particle size because larger particles require higher furnace temperatures for the same conditions. The influence due the introduction of oxygen into the sintering furnace needs to be examined with particular care.

Control of the particle size distribution

In Figure 4.1, the yield of nanoparticles, measured using the DMA, is shown as a function of the initial mobility-equivalent diameter D_{mi} of unsintered particles at different temperatures in the evaporation furnace. The synthesis set-up was shown in Figure 3.4. Note that these curves are not equivalent to particle size distributions as the efficiency of the radioactive charger, the transfer function of the DMA and the particle losses are all included. However, for the purposes of this investigation, only the yield of size-fractionated particles is relevant. The mobility diameter D_{mi} with the largest yield shifts to larger values as the temperature in the first tube furnace rises as a result of higher vapour pressure. It is also apparent that there is a specific temperature which maximises the yield for individual particle sizes. For this reason, the maximum particle number concentration for each particle size can be found applying the DMNPS method to each particle size at different temperatures.

The effect of the sintering and crystallisation of SnO particles in-flight in the second furnace is shown in Figure 4.2 which illustrates the yield of size-fractionated particles having an initial mobility-equivalent diameter of D_{mi}= 25 nm at various temperatures, measured by means of DMNPS (Section 3.2.1). The mean fractionated and sintered particle size is defined as D_{ms}. It can be seen that the width of the size distribution is very narrow; in reality, it is even narrower, due to the convolution of the two DMA transfer functions. As the sintering temperature rises, the mobility-equivalent diameter decreases

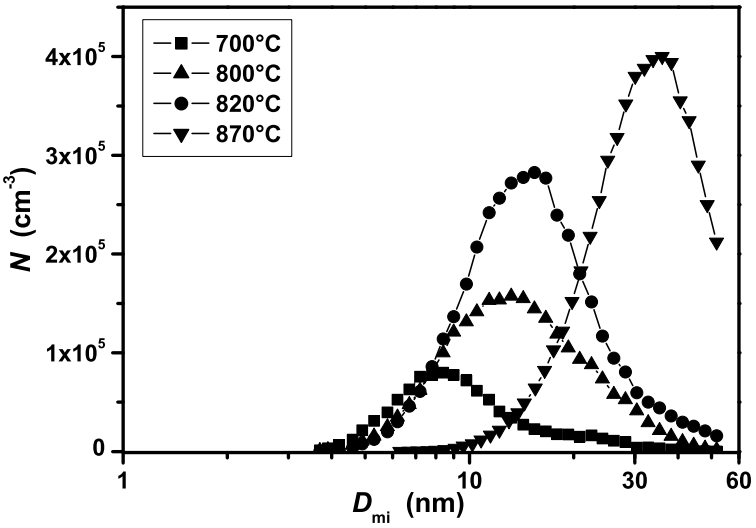

Figure 4.1: Yield of SnO nanoparticles as a function of the mobility-equivalent particle diameter selected by the DMA at different temperatures in the evaporation furnace.

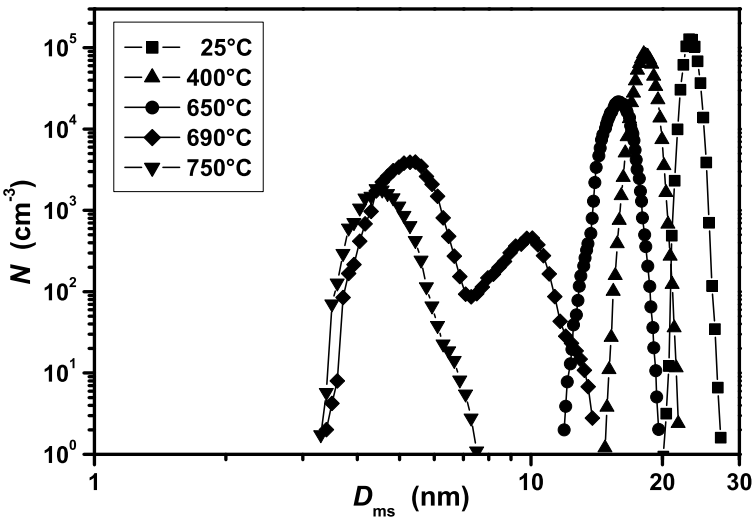

Figure 4.2: Yield of size-fractionated SnO particles having an initial mobility-equivalent diameter of D_{mi}=25 nm after in-flight sintering and crystallisation at different temperatures.

because of the compaction caused by the sintering of several primary particles in the aggregates [Kruis et al. [48]] The model for solid-state sintering may be applicable to nanoparticles. The development of a bimodal distribution at 690 °C and above arises from the partial evaporation and subsequent secondary nucleation of the SnO nanoparticles. The sintering temperature of 650 °C was chosen for the subsequent synthesis of nanoparticles for this size as it maintains monodispersity. The reduction in the yield of particles at this temperature, compared to room temperature, is brought about by the heating and cooling cycle which induces a radial temperature distribution inside and just outside the furnace; this leads to particle losses due to thermophoresis [Kennedy et al. [44]]. The effect of secondary nucleation was confirmed by means of TEM measurements in the range of 650-750 °C.

DMNPS measurements do not provide information about the morphology of gas-phase synthesised SnO_x nanoparticles. Morphology is an important parameter to investigate the characteristics of the reactive surface during gas-sensing processes. A defined particle SnO_x formation makes it possible to calculate the total reactive surface area for gas-sensing application. Thus, further investigations applying methods such as TEM, STM and SEM are required.

First of all, the formation of the morphology of unfractionated SnO nanoparticles was followed by means of TEM. Figure 4.3(a) shows the morphology of SnO particles immediately after an evaporation furnace temperature of 800 °C. The particles are aggregates with a low degree of crystallinity; this is evidenced by diffused rings in the electron diffraction. During in-flight sintering of unfractionated particles at 650 °C, an improvement in the particle and crystalline quality is obtained (Figure 4.3(b)). The particles have a relatively broad size distribution. The best results are obtained, as expected, using size-fractionation and subsequent sintering/crystallisation (Figure 4.4). Quasi-spherical morphology and a narrow size distribution are achieved for particles having an initial mobility-equivalent diameter D_{mi} below 30 nm; larger particles can be seen to be incompletely sintered and crystallised during the residence time of 0.5 s in-flight at 650 °C: this can be explained by looking at the characteristic coalescence time τ_c , which is a function of the radius of the primary particles, the sintering mechanism and temperature-dependent parameters, such as the surface tension and solid-state diffusion coefficient. Time τ_c can be estimated as follows [Kruis et al. [47]]:

$$\tau_c = \frac{1}{16}\frac{k_b T a^3}{D\gamma\nu_m} \tag{4.1}$$

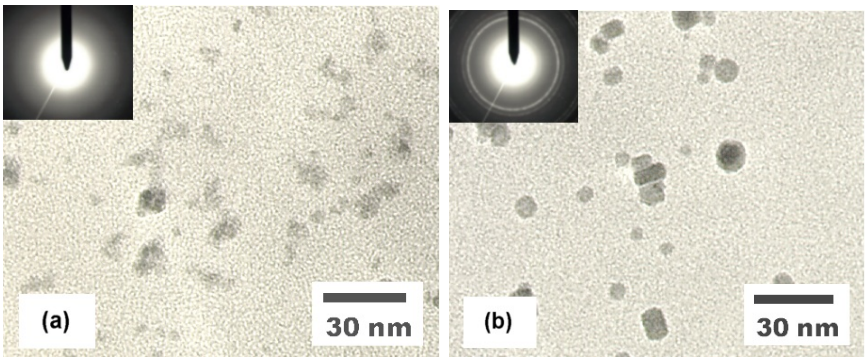

Figure 4.3: TEM micrographs of unfractionated SnO nanoparticles (a) after evaporation in furnace 1 and (b) after subsequent sintering and crystallisation at 650 °C in furnace 2.

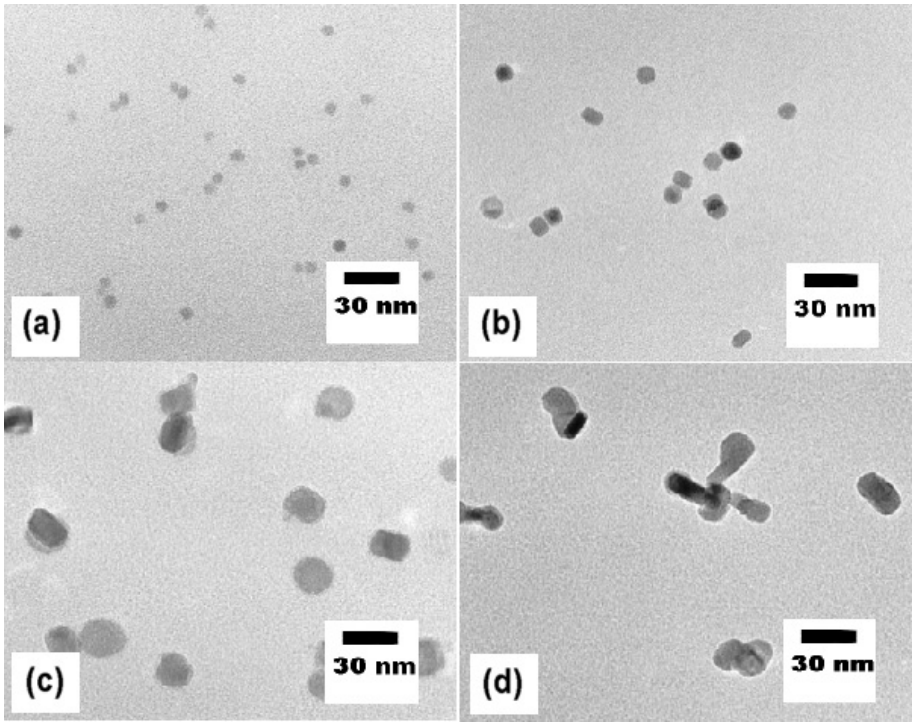

Figure 4.4: TEM micrographs of size-fractionated SnO nanoparticles, having initial mobility diameters of (a) 10 nm (b) 20 nm (c) 30 nm and (d) 45 nm which are sintered and crystallised in-flight at 650 °C for 0.5 s.

where k_B is the Boltzmann constant; D the diffusion coefficient; T the temperature; γ the surface tension; a the particle radius; and ν_m the molecular volume. The formula indicates that the characteristic coalescence time increases rapidly as the particle radius grows, so that larger aggregates (composed of larger primary particles at an intermediate stage) will require a longer residence time at the same temperature to become completely coalesced. This was confirmed by the experiments.

In Section 2.1.1, it was shown that nanoparticle sensor applications with particle diameters over D_{ms}=30 nm are not useful for determining size-dependent gas-sensing properties in this investigation because the gas-sensing properties are much less affected due to a different ratio between thickness of the charge depletion layer and the total particle volume compared to 10 nm large particles. Accordingly, no further experiments with increased residence times, with the objective of obtaining coalesced particles of larger sizes, were carried out.

In Figure 4.5, the particle size distribution determined from TEM micrographs with initial particle sizes (D_{mi}) of 15, 25 and 32 nm is presented, if the initial particle diameter is D_{mi}=32 nm the standard deviation is σ_{gT}=1.05. It can be seen that a relatively narrow size distribution, which is slightly broader for smaller particles, is obtained (for D_{mi}=15 nm particles σ_{gT}=1.09). This is caused by the diffusional broadening of the transfer function of the DMA; it is more significant for smaller particles [Hagwood et al. [35]]. The width can, in principle, be reduced further by changing the operating conditions of the DMA or by using a second DMA after sintering. The monodispersity of size-selected SnO nanoparticles measured using the DMNPS method, is confirmed. An additional oxidation process during the gas phase synthesis does not affect the particle size distribution.

The particle size analysis was also confirmed by means of STM measurements. STM offers the possibility of obtaining an impression about the 3-dimensional particle film formation although the resolution in the plane is limited due to the tip. Figure 4.6 shows STM micrographs of fractionated SnO nanoparticle layers with two different sizes, D_{ms}=10 nm and 30 nm. The sintering temperature to obtain monodisperse size distribution for D_{ms}=10 nm was 645 °C and for D_{ms}=30 nm 670 °C. No post-heating treatment was carried out. The large particle size difference can be accurately measured. The 10 nm particles cannot be detected separately. It was established that the particle layer of as-deposited SnO nanoparticles is a very porous media: this is one of the goals of this investigation because porous

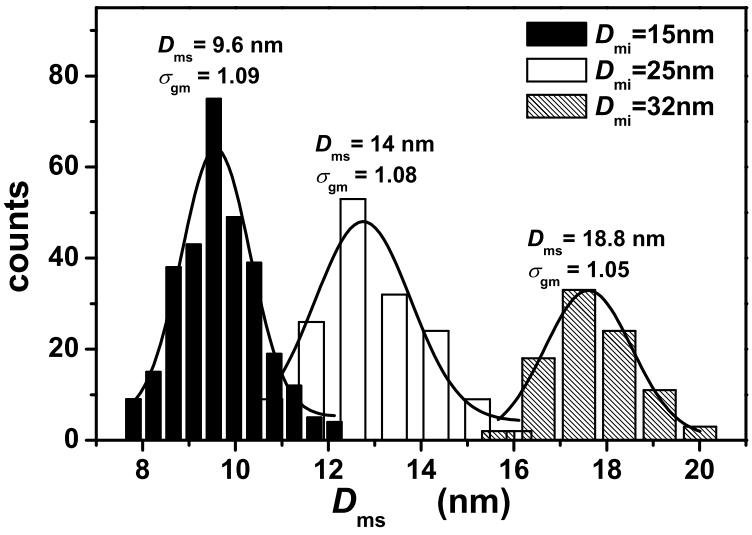

Figure 4.5: SnO nanoparticles extracted from TEM micrographs with initial sizes of D_{mi}=15, 25 and 32 nm. The standard deviation σ_{gT} is indicated.

media offer a higher surface area and, therefore, a larger amount of reactive places for the same layer volume (Section 1.1). This result is fulfilled for both particle sizes. Up to now, material investigations have concentrated on SnO, i.e. unoxidised nanoparticles. However, for gas-sensing measurements, a chemical composition of SnO_2 is required for sensing material. Additionally, SnO_2 has to be understoichiometric so that the chemisorption process, mentioned in Section 2.1.1, occurs. Therefore, TEM and XRD are used for the analysis of the crystallographic structure and AES and RBS for the measurement of the surface and volume stoichiometry. Generally, an oxygen deficiency of 0.1% is enough for gas-sensing application [Weisz [88]]. As described in Section 3.2.1, it is possible to add a defined amount of oxygen into the second furnace to oxidise the SnO nanoparticles to SnO_x ($1<x<2$).

TEM measurements do not only supply information about the particle morphology. The measurement system can also be applied for the analysis of the crystallographic structure using the electron diffraction pattern. First of all, measurements of the crystallographic structure are done by means of TEM analysis on fractionated SnO nanoparticles in the gas phase without oxygen and by adding 10 vol% oxygen into the second furnace (Figure 4.7). The initial mobility diameter is $D_{\mathrm{mi}} = 25$ nm and the measured mean diameter of

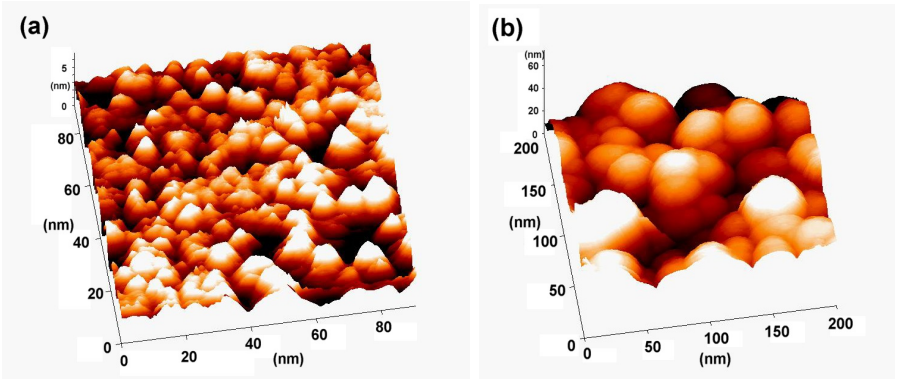

Figure 4.6: STM measurements of size-fractionated SnO nanoparticles with particle sizes of (a)D_{ms}=10 nm and (b)D_{ms}=30 nm.

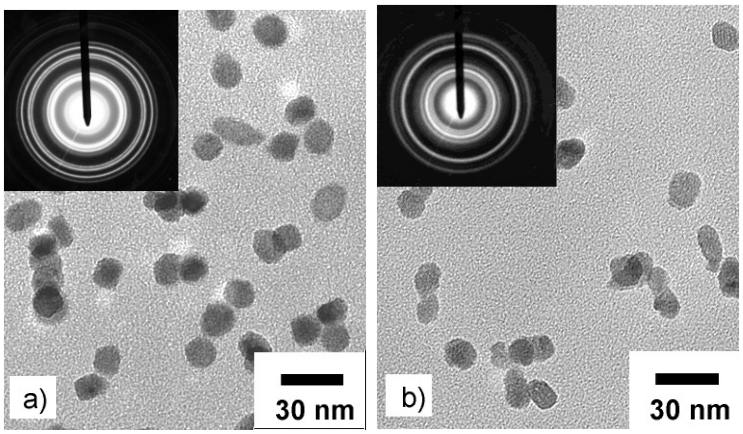

Figure 4.7: TEM image and electron diffraction patterns of fractionated SnO nanoparticles at an initial mobility diameter of 25 nm (a) without oxygen and (b) adding 10 vol% oxygen.

the sintered nanoparticles is $D_{\mathrm{ms}} = 14$ nm; this is in accord with the DMNPS results (Figure 4.2). The nanoparticles are spherical and crystalline and have a narrow size distribution. Diffraction rings indicate a good crystallinity of the size-selected tin oxide nanoparticles with and without oxygen. A comparison of the lattice parameter, with gold as reference material, shows that the diffraction pattern of the unoxidised sample indicates romarchite SnO with a tetragonal structure. The electron diffraction pattern of the oxidised sample indicates two structures: Casserite, i.e. tetragonal SnO_2, and a high pressure phase of orthorhombic SnO_2. Shek et al. also found, by means of X-ray diffraction, a mixture of an orthorhombic and a tetragonal SnO_2 phase in ultrafine tin oxide particles produced by an inert gas condensation method

[Shek et al. [80]]. The orthorhombic phase of SnO_2 is metastable and was observed under high pressure conditions [Suito et al. [83]]. Shek et al. believe that the orthorhombic phase is an intermediate product appears when disordered tin oxide transforms to stable tin oxide (rutile phase) via annealing under oxygen deficiency conditions. The structure of the thin films of SnO_2 change, during subsequent annealing in oxygen atmospheres up to 1,000 °C, into a tetragonal phase. The epitaxial tin oxide thin film phase transformation of SnO to SnO_2 starts at 300 °C and is completed at 700 °C. Between these temperatures an additional phase of Sn_3O_4 has been detected [Pan et al. [69]]. The nanoparticles in this synthesis set-up were sintered at 650 °C in the gas phase under different oxygen conditions. An annealing process at higher temperatures than 300 °C would probably be necessary to achieve a fully stable tetragonal phase of tin oxide, but this treatment will certainly also change the particle size distribution of the nanoparticle films. As the particle size is to be kept constant during the gas-sensing operation, the effect of an annealing at temperatures higher than 400 °C was not investigated because this would cause a further sintering process and, therefore, a loss of the well defined particle layers and monodisperse particle size distribution. However, the investigation of the crystallographic structure will be discussed more in detail in the next section.

Study of the surface topography after annealing

First studies analysing the topography of the SnO_x nanoparticle layer have been carried out by STM measurements (Figure 4.8). Nevertheless, this method is limited laterally due to the width of the tip. Therefore, the SEM method is used. Figure 4.8(a) shows a view of the surface topography of an unannealed tin oxide nanoparticle film. The regular grain size, uniform particle deposition, porous structure and connectivity between the particles can be qualitatively identified. No difference could be seen, by means of SEM between the nanoparticle film which is annealed for 1,000 hours at 300 °C (see Figure 4.8(b)) and the unannealed nanoparticle film. This was supported by XRD measurements which did not detect a change in the crystallite size of the annealed layer. The formation of the sintering necks which, unfortunately, cannot be seen using the SEM method due to insufficient resolution, is thus possible without changing the particle size. Equation (2.27) describes the development of the ratio of the sinter neck width and the particle diameter (x/a), which is valid for constant a, constant temperature and for the initial stages of the sintering $(x/a<1)$, whereby (x/a) is a function of $t^{1/(n+1)}$, $t^{-1/5}$ and $t^{-1/6}$ respectively. Consequently, after a very rapid initial increase in the neck width, the neck width develops much more slowly. This ensures

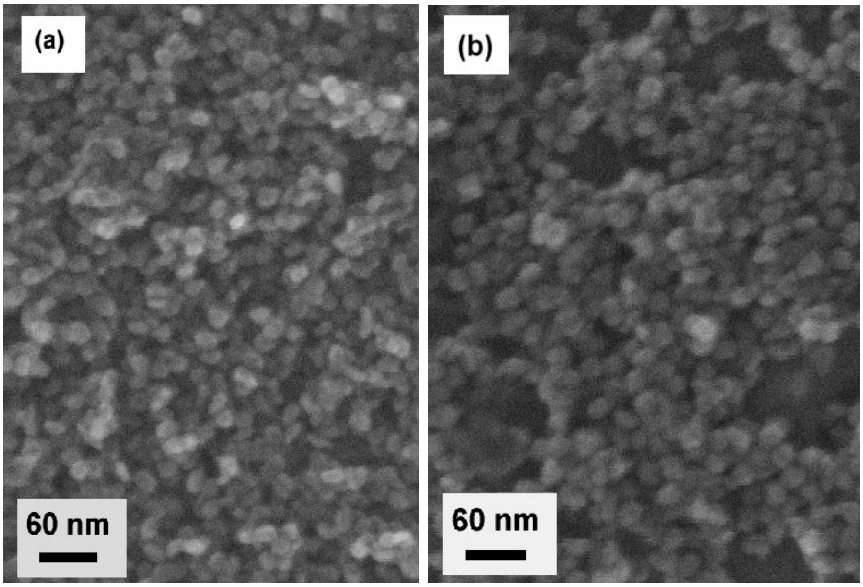

Figure 4.8: SEM micrograph of a nanoparticle film composed of size-fractionated (a) as-deposited SnO nanoparticles and (b) annealed at 300°C for 1,000 hrs in oxygen and ethanol.

that sinter necks can develop without substantially changing the particle dimensions. The stability of the layer against grain growth is probably due to the fact that the particles already underwent a high-temperature treatment during the gas-phase synthesis. Furthermore, the uniform grain size ensures a similar neck formation rate for all particles without substantially changing the grain size. Further investigations concerning these phenomena are carried out with X-ray diffraction measurements using synchrotron sources, presented in the next section.

4.2 Study of the chemical composition of SnO_X nanoparticles during synthesis

It is well known that two conditions have to be fulfilled for tin oxide to act as a gas-sensing layer. Firstly, the material must have an SnO_2 crystallographic structure; secondly, SnO_2 has to have oxygen vacancies (understoichiometric). This section shows the results of the analysis of the chemical composition influenced by different in-situ and ex-situ process parameters.

4.2.1 Change of the crystallographic structure due to addition of oxygen or annealing

Two different SnO_2 phases have been investigated up to now by means of electron diffraction: the tetragonal phase (casserite) and the high pressure orthorhombic phase [Suito et al. [83]]. Differences between these phases concerning their gas-sensing properties have not yet been investigated. Consequently, it is necessary to obtain information about the crystallographic phases of tin oxide layers based on monodisperse nanoparticles and then, if the phase is confirmed, the gas-sensing characteristics of the two samples need to be compared. In this section, basic information about the crystallographic structure of nanoparticle layers dependent on various process parameters is investigated. Gas-sensing characteristics are discussed in Section 4.3 and compared with the crystallographic structure and stoichiometry results; these measurement are carried out to understand the sensing mechanism of tailored SnO_2 nanoparticle films and to optimise the gas-phase synthesis process.

At the beginning of this investigation it was necessary to prove the appropriateness of the synthesis set-up. The crystallite phase of tin oxide layers, composed of size-fractionated nanoparticles with different mobility-equivalent diameters in the range of $D_{ms} = 10$-25 nm after sintering without the addition of oxygen, was, therefore, measured (Figure 4.9). A small particle size of 10 nm causes a strong broadening of the Bragg peaks which can overlap other peaks; this leads to a more difficult analysis of the lattice structure. However, for particle sizes over 15 nm, the predominant peaks observed at 2Θ=21.11° (d=4.88 Å), 2Θ=34.4° (d=3.002 Å), 2Θ=38.88° (d=2.689 Å) and 2Θ=43.13° (d=2.435 Å) correspond to the (001), (101), (110) and (002) planes of the tetragonal SnO (romarchite) phase. The (101) and the (110) planes could also be detected for 10 nm particles. No Bragg peaks corresponding to SnO_2 were found. If SnO_2 particles are to be generated, an additional oxidation process is necessary in this set-up. This oxidation process was investigated by means of electron diffraction (Figure 4.7). In order to confirm the results and to achieve additional information about the oxidation process dependent on different parameters, additional XRD measurements were carried out since, in the case of TEM investigations, the oxidation process took place in the sintering furnace.

If 10 vol% oxygen is added, both SnO_2 phases are detected (Figure 4.10). O denotes the position of the Bragg peaks for orthorhombic SnO_2 and T the position of the Bragg peaks for tetragonal SnO_2. The Bragg peaks

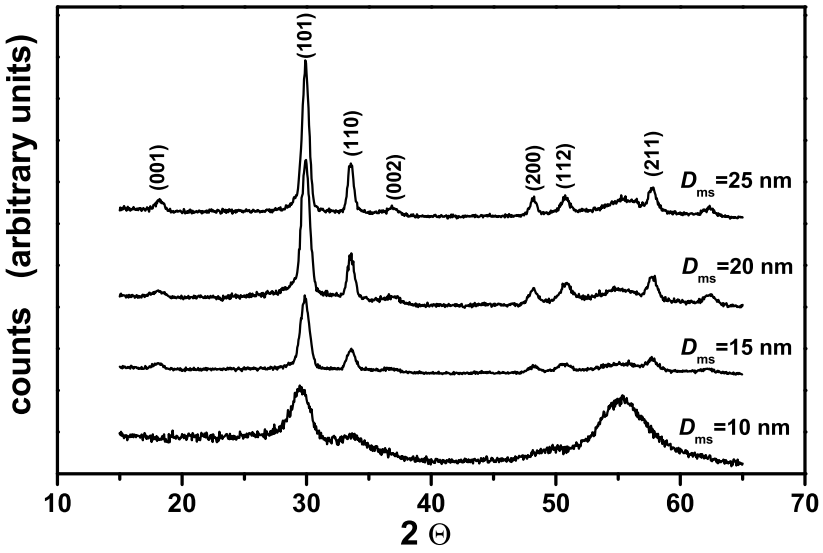

Figure 4.9: Θ-2Θ scans of a nanoparticle film composed of size-fractionated SnO nanoparticles with D_{ms} within the range of 10-25 nm without addition of oxygen in the second furnace. The lattice planes of tetragonal SnO are indicated.

at 2Θ=24.4°, 2Θ=29.8° and 2Θ=35.7° clearly point to the (110), (111) and (002) planes of orthorhombic SnO_2; 2Θ=31.04° (d=3.34 Å), 2Θ=34.4°, 2Θ=39.63° (d=2.64 Å) and 2Θ=44.27° (d=2.375 Å) clearly point to the (110), (101) and (200) planes of the tetragonal SnO_2 phase. An increase in the oxygen concentration during in-situ oxidation does not change the crystallographic structure. Even after additional heat treatment at 400 °C in synthetic air, no change was found.

The influence of the deposition technique on the post-annealing process was investigated. Electrical forces using an electrostatic precipitator (ESP) and inertial forces using a low pressure impactor (LPI) were applied. SnO size-selected nanoparticles are deposited in the case of both techniques and annealed in synthetic air, at a volume flow rate of 150 ml/min, at 300 °C (maximum operating temperature) for 2 hours. This is done to obtain information about possible changes in the chemical composition during annealing before using the nanoparticle film for gas detection. Figure 4.11 shows the Θ-2Θ scans of the as-deposited SnO nanoparticles with D_{ms}=20 nm using ESP and LPI after annealing. If the low pressure impaction method is used,

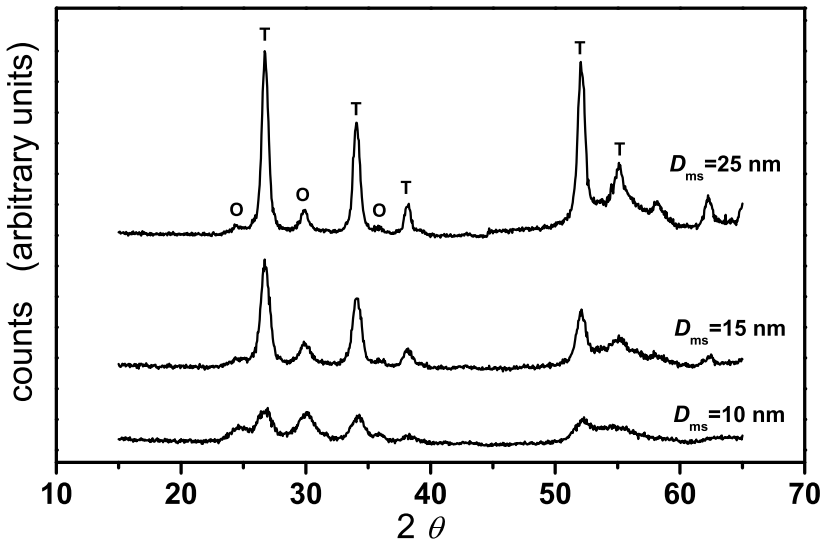

Figure 4.10: Θ-2Θ scans of a nanoparticle film composed of size-fractionated in-situ oxidised SnO_x nanoparticles with D_{ms} within the range of 10-25 nm with the addition of 10 vol% oxygen in the second furnace. O denotes the position of the Bragg peaks for orthorhombic SnO_2 and T the position of the Bragg peaks for tetragonal SnO_2 planes.

the nanoparticle layer consists of only an orthorhombic SnO_2 phase, whereas a mixture of a tetragonal and orthorhombic SnO_2 appears if electrical forces are used for the deposition of the nanoparticles. These phenomena can be explained by an incompleted oxidation process after using the LPI deposition method causing a different layer formation; it results in a metastable SnO_2 phase. Because of the higher velocity of nanoparticles during the LPI process, it is assumed that an LPI method will create more dense particle layers than when using an ESP. Even after 24 hours at 300 °C, no tetragonal phase in the case of LPI was detected. This means that, after the nanoparticles have been deposited by means of inertial forces, a complete oxidation to a tetragonal SnO_2 phase requires higher temperatures. For the analysis of gas-sensing properties of SnO_2 nanoparticle films not only the crystallographic structure is of importance but also the stoichiometry, especially at the surface (Section 2.1.2). The mean crystallite size of the SnO nanoparticles is calculated from the line-broadening of all Bragg peaks, whereby the resolution of the measurement set-up is included. Table 4.1 shows crystallite size values compared to particle size values measured by means of DMNPS

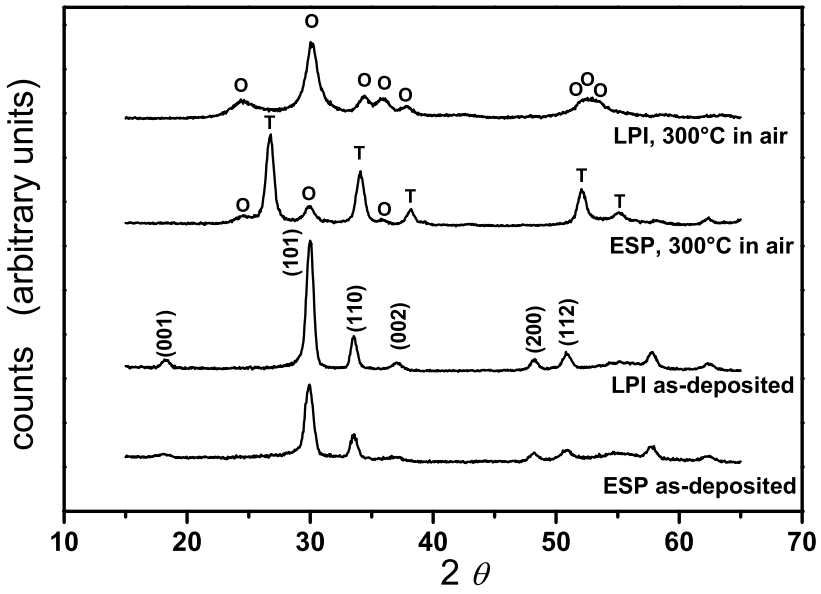

Figure 4.11: Θ-2Θ scans of a nanoparticle film composed of size-fractionated SnO nanoparticles with D_{ms}=20 nm using ESP and LPI. Both samples were post-annealed at 300 °C in synthetic air for 2 hours.

and TEM. The size values are in good accord with each other. The larger difference detected in measuring the 10 nm sample might have occurred due to the existence of only one Bragg peak to calculate the crystallite size. Consequently, the gas-phase synthesis set-up for monodisperse particles is reliable. Additionally, the similarity of the values for particle and crystallite indicates that each size-selected SnO particle are monocrystalline.

4.2.2 Study of the volume and surface stoichiometry change of SnO_x nanoparticle films

In this investigation the gas-sensing material is used at operating temperatures up to 300 °C. The change in the chemical composition of the sample has, therefore, to be followed up to the maximum temperature in order to understand possible changes in the gas-sensing characteristics. In Section 4.2.1, the change in the crystallographic structure was investigated by means of

D_{mi} (nm)	DMNPS (nm)	TEM (nm)	XRD (nm)
15	10.2	9.6	7.3
25	14.5	14.0	14.9
32	18.3	18.8	17.5
45	24.5	24.2	23.3

Table 4.1: Comparison of the mean measured particle size using DMNPS and TEM and the mean crystallite size using XRD for different initial mobility particle diameters D_{mi}.

XRD. This method provides information about the whole nanoparticle layer in order to analyse possible changes in the crystallographic structure, since a stable lattice structure is required during gas-sensing measurements.

The surface is the predominant factor in determining the gas-sensing characteristics. AES is a very surface-sensitive analysis method (Section 3.3.3). Consequently, this method is used to measure the change in the surface stoichiometry due to in-situ high temperature oxidation or ex-situ heat treatment.

Analysis of the volume stoichiometry of as-deposited SnO_x nanoparticles

The chemical composition of tin oxide nanoparticle films can also be investigated by means of RBS. This method enables the stoichiometry of nanoparticle films in different planes, i.e. in different film depths, to be determined.

Figure 4.12 shows two RBS spectra of as-deposited monosized nanoparticles ($D_{mi} = 20\,nm$) on polished carbon substrates. The layer thickness is found to be 350 nm. This value is also calculated from the deposition area, the deposition time and the particle number concentration during the gas phase synthesis process. The curves correspond to the different oxygen concentrations in the second furnace. The effect of the addition of oxygen can be seen by the intensity change at the oxygen peak. If 10 vol% oxygen is added in the second tube furnace, the value of the edge peak and the area of the oxygen peak increase. Thus, as already determined by means of TEM and XRD, the oxygen content of SnO_x particles is increased by adding oxygen.

The Sn-O ratio through the layer can be determined by means of the

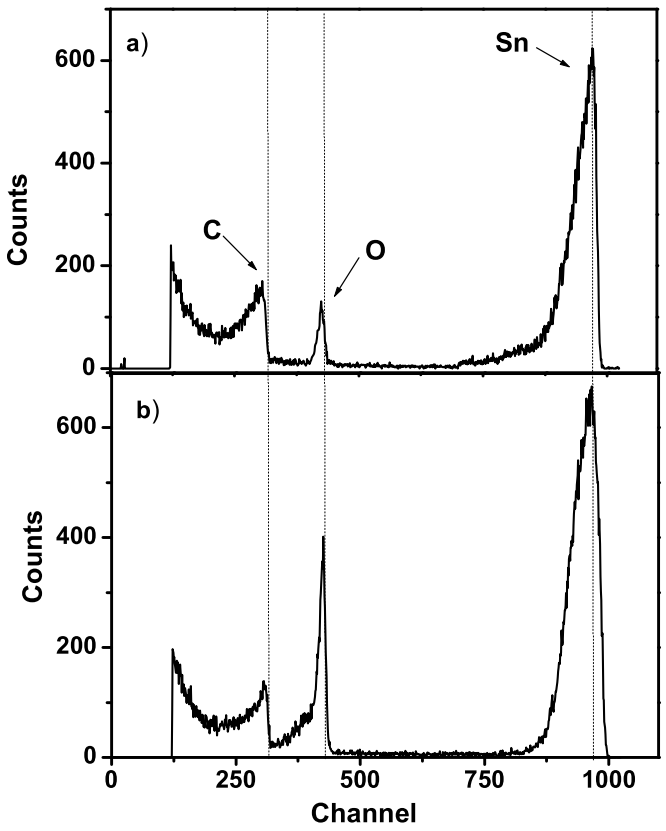

Figure 4.12: RBS spectrum obtained from monodisperse nanoparticle films of SnO_x on glassy carbon (a) without oxygen and (b) with 10 vol% oxygen (D_{ms}=20 nm).

"rump" program. The concentration depth profiles for the SnO_x layer are depicted in Figure 4.13. Figure 4.13(a) shows that without oxygen the stoichiometry of the SnO material used is initially constant ($SnO_{1.1}$) throughout the complete layer. This is in agreement with the crystallographic structure results in Section 4.2.1, where only the tetragonal SnO structure was found if no oxygen is added in the sintering furnace. In the first 100 nm, SnO_x has a higher oxygen concentration ($SnO_{1.3}$), probably caused by a physisorption process of oxygen on the surface as the samples are transported in air. Also water molecules on the surface may contribute to the increase in the oxygen concentration. If 10 vol% pure oxygen is introduced into the second furnace, the stoichiometry of the layer lies between $SnO_{1.8}$ on top of the layer and SnO_2 inside the layer (Figure 4.13(b)). The lower oxygen content on top of

the layer can be caused by oxygen vacancies on the surface of the sensing material. The surface stoichiometry results are discussed below.

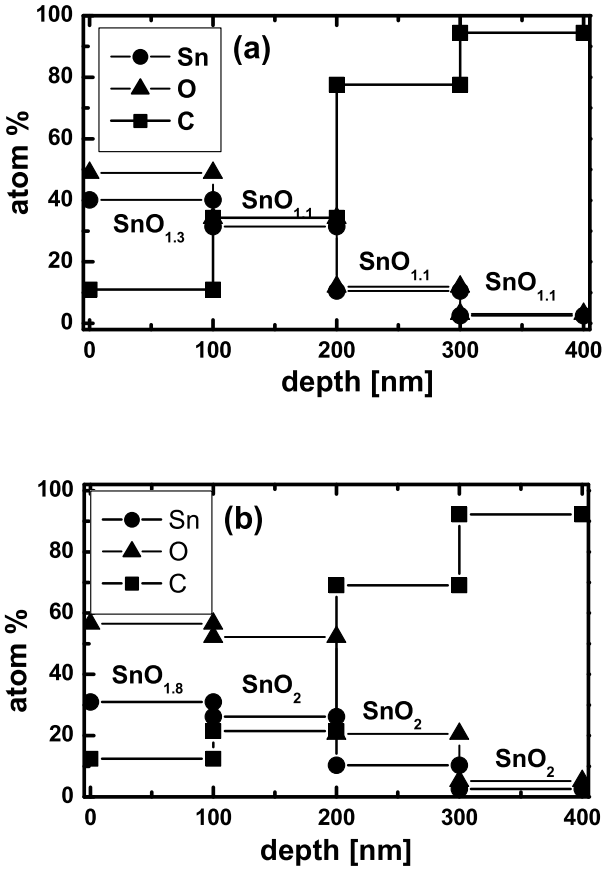

Figure 4.13: Element depth profile of monodisperse thin particle films of SnO_x on glassy carbon substrates (a) without oxygen and (b) with 10 vol% oxygen (D_{ms}=20 nm).

Stoichiometry change on the SnO_x nanoparticle surface

The upper panel of Figure 4.14 shows a typical AES spectrum recorded from 10 nm SnO nanoparticles deposited on a Si(111) surface. The Sn(MNN) doublet consists of two well separated features at 421 and 429 eV. The intensity ratio between the O and Sn Auger features corresponds to a composition of $SnO_{1.2}$. This finding is in agreement with TEM, RBS and XRD studies which prove the tetragonal SnO phase and a similar Sn-O ratio of the particles. The

C signal at 270 eV is due to residual hydrocarbon contamination during the transfer of the samples from the deposition to the analysis chamber. The shape and intensity of the Auger lines do not change with the particle size, indicating that the surface chemical composition is independent of the particle diameter.

The SnO samples are post-annealed at 300 °C in synthetic air for one hour. Auger spectra of annealed nanoparticles of different sizes are shown in the lower panel of Figure 4.14. This treatment changes the shape of the Sn doublet significantly. The double structure in the first derivative spectrum corresponds to a well resolved double peak structure in the original spectrum; this can be retrieved by numerical integration of the Auger spectra recorded. The variation observed in the line shape, due to annealing, indicates a broadening of the original peaks which may be attributable to different chemical environments of the tin atoms. Similar line distortions were reported earlier for as-deposited and at 500 °C annealed SnO_x films prepared by ion-beam assisted deposition [Choi et al. [12]]. The authors interpreted this finding as being evidence of the presence of metallic Sn at the surface that causes chemically shifted Auger lines. However, in this investigation no evidence of metallic Sn could be found. The change in the Sn Auger lines may be related to an intermediate and not fully relaxed oxidation state of the Sn atoms. Annealing leads also to a structural change in the nanoparticle film since weak Auger features of oxidised Si are observed at around 80 eV (see also Section 4.2.1). The layer apparently opens up when the nanoparticles are oxidised. Oxidation of SnO is accompanied by a volume reduction of approximately 7%. A change of microstructure was observed earlier with thin films [Pan et al. [69] and Choe et al. [10]]. The change in the Sn line shape and the enhanced oxygen signal due to SiO_2 complicate a quantitative analysis of the nanoparticle stoichiometry. To obtain a good estimate, the Auger spectra were adjusted by substracting the SiO_2 background signal and by comparing the results from the peak-to-peak-intensities with an analysis of the original, i.e. an integrated spectra. Both ways of determining the Auger line intensities result in a composition of approximately SnO_2, i.e. the surface of the particles is oxidised by the annealing process. However, the distorted line shape indicates a mixed oxidation state.

A second post-annealing process at 300 °C for 1 hour in synthetic air leads to a further change in the Auger spectra as shown in the top panel of Figure 4.15. The Si substrate signal increases; this may be due to an enhanced opening of the nanoparticle film. The Sn Auger doublet shows again two well resolved features, indicating a uniform oxidation state. To extract the

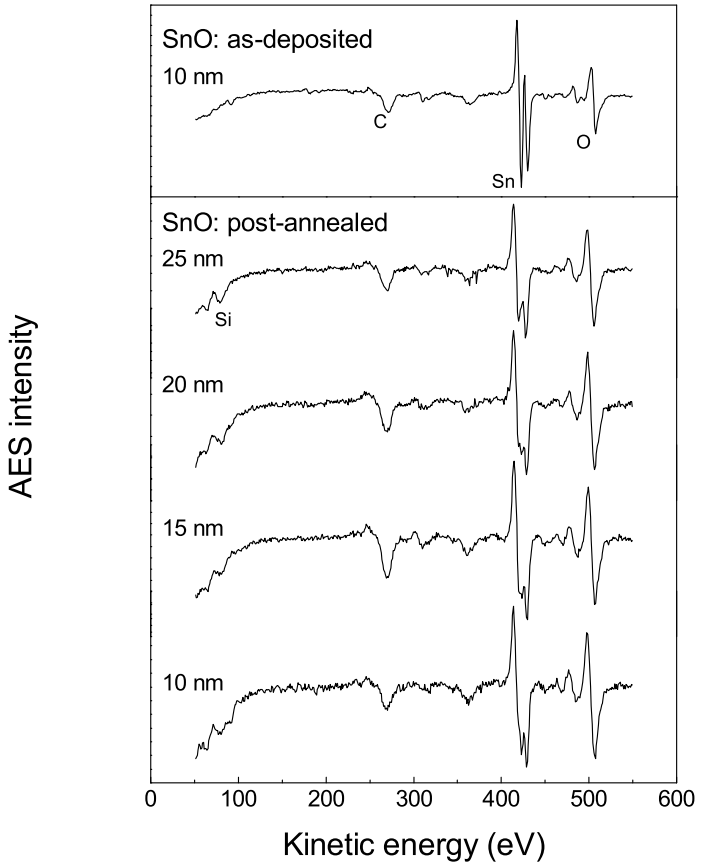

Figure 4.14: Top panel: Auger spectrum of as-deposited 10 nm SnO nanoparticles; lower panel: Auger spectra of SnO nanoparticles of different sizes annealed once at 300 °C in synthetic air for one hour.

true stoichiometry of the nanoparticles, the tin oxide spectra are adjusted by subtracting the normalised Auger spectrum of the Si substrate shown in the middle panel of Figure 4.15. The Si spectrum is normalised to the intensity of the Si line in the tin oxide spectra. The lower panel of Figure 4.15 illustrates the corrected Auger spectrum for the 10 nm nanoparticles. The resulting oxygen content is almost unchanged, irrespective of the particle size; it corresponds to $SnO_{1.9}$. Consequently, annealing of as-deposited SnO nanoparticles at 300 °C in synthetic air for 2 hours alomost leads to a stoichiometric SnO_2 phase. This has been confirmed by XRD measurements but indicated two crystallographic structures (Figure 4.11) depending on the particle deposition method.

Stoichiometry change of in-flight unoxidised and oxidised SnO_x nanoparticles

In order to study the properties of nanoparticles oxidised in the gas phase, SnO_x particles of 20 nm diameter were prepared by adding 10, 20 and 35 vol% oxygen to the carrier gas. The increasing oxygen content extracted from the peak-to-peak Auger intensities is plotted as solid circles in Figure 4.16. By taking the original Auger line intensities after numerical integration, the error in the oxygen content determined is $\Delta x \cong \pm 0.2$. Hence, it must be concluded that, as the oxygen content in the carrier gas increases, the in-flight oxidation of the particles changes the stoichiometry from $SnO_{1.2}$ (no oxygen) to $SnO_{1.8}$. After deposition on the Si substrates, the in-flight oxidised particles are post-annealed at 300 °C in synthetic air for one hour. The resulting oxygen content is also plotted in Figure 4.16 for single and double post-annealing steps. The stoichiometry of the nanoparticles is independent of the number of post-annealing steps. All in-flight oxidised nanoparticles show a composition of approximately $SnO_{1.8}$: this is significantly lower than the oxygen content of post-annealed SnO nanoparticles. Even heating at 300 °C for 4 hours in synthetic air does not change the $SnO_{1.8}$ composition. Thus, for a given heat treatment, the final stoichiometry of the particles is dependent on its previous history during synthesis. Effective oxidation by post-annealing of the deposited particles is suppressed if the particles are pre-oxidised in the gas phase. A possible explanation is that an inhomogeneous phase mixture of SnO, Sn_3O_4 and SnO_2 of the in-flight oxidised particles exists at the surface of the nanoparticles, but no intermediate phases were found by means of XRD measurements (Section 4.2.1). From oxidation studies of thin SnO films, it is known that the transformation into SnO_2 occurs during heating at 500-600 °C for 1 hour, either directly or by passing through an intermediate phase of Sn_3O_4 [Geurts et al. [29]]. In this investigation, in-flight oxidation

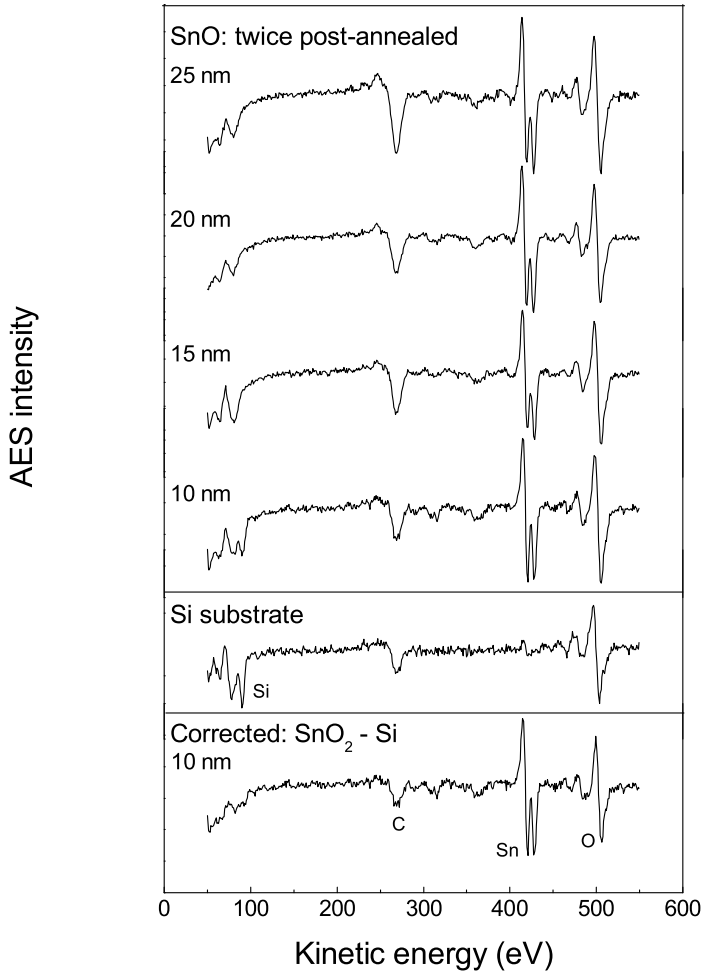

Figure 4.15: Top panel: Auger spectra of SnO_x nanoparticles of different sizes post-annealed twice at 300 °C in synthetic air for 1 hour; middle panel: Auger spectrum of the Si substrate; bottom panel: adjusted Auger spectrum for 10 nm SnO_x nanoparticles.

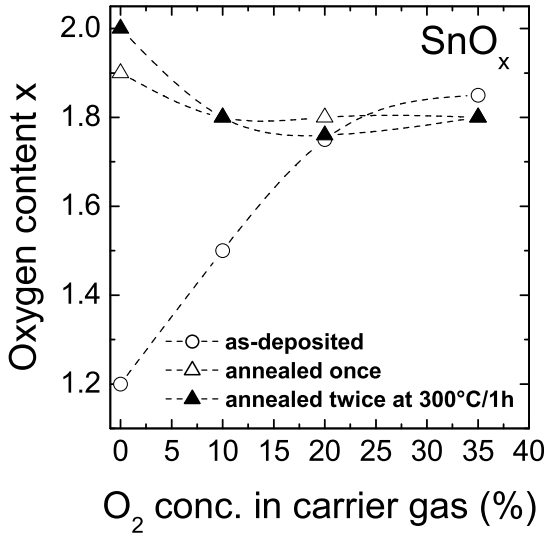

Figure 4.16: Change of oxygen content in SnO_x with different concentrations of oxygen in the carrier gas, before and after annealing.

occurs within a much shorter time scale (0.5 s) and may leave the nanoparticles in a non-uniform state; this shows a different oxidation behaviour during post-annealing for different in-situ treatments.

The oxygen content of SnO nanoparticles oxidised in-flight or by a post-annealing process after deposition is independent of the particle size. However, the AES and XRD measurement results show that in-situ oxidation produces tin oxide of different chemical composition compared to that after post-treatment in air. XRD measurement results show that post-annealing of SnO nanoparticles in synthetic air at 300 °C produces - normally - a thermodynamically unstable orthorhombic phase if the LPI deposition method is used, whereas Auger measurement indicates that such a treatment generates a full stoichiometric tin oxide surface. However, the microhotplates for electrical and gas-sensing characterisation have been configured for applying the LPI method because tin oxide nanoparticle films can be produced by LPI much faster compared to the ESP technique (Section 3.2.2).

However, the Auger results do not indicate that the surface of the tin oxide nanoparticles is fully oxidised if an in-situ high temperature oxidation has occurred. Even after additional heat treatment in synthetic air, a maximum

stoichiometry value of $SnO_{1.85}$ was measured. This means that, although the crystallographic structure analysis only shows an SnO_2 structure, there are more oxygen vacancies on the surface of in-situ oxidised SnO particles than on the surface of post annealed SnO nanoparticle layers. The Auger results are independent on the particle size [Ramamoorthy et al. [73]]. Consequently, the process parameters described in this section make it possible to fabricate SnO_x nanoparticle films with a defined chemical composition. The effect on the gas-sensing properties will be discussed in the next chapter.

4.3 Gas-sensing properties of monodisperse SnO_2 nanoparticle layers

Prior to the gas-sensing measurements, the SnO_x nanoparticle films are annealed at a temperature of 300 °C for about 2 hours in 1,000 ppm diluted ethanol. Annealing leads to the formation of sintering necks. This is supported by the fact that during the annealing process the resistance of SnO_x nanoparticle samples decreases by several orders (Figure 4.17) although a morphology change of the particle layer is not detetected by means of SEM as shown in Figure 4.8. The results for a sample with a mean particle diameter of D_{ms}=15 nm show that resistance, initially 5 GΩ at room temperature, reaches a stable value of 12 kΩ after heating for 2 hours at 300 °C; if the sample is annealed a second time, the resistance from room temperature to the maximum operating temperature changes by a maximum of one order, e.g. for D_{ms}=15 nm between ∼100 kΩ at 25 °C and 10 kΩ at 300 °C. This annealing procedure is always carried out for a new sample combined with a temperature calibration of the microhotplate. As described in Section 2.3, the use of nanoparticles is of great interest for gas-sensing applications due to their large surface to volume ratio. However, the ratio between particle volume and thickness of the charge depletion layer can cause significant changes in the gas-sensing properties. This section discusses different characteristics of nanoparticle layer, such as chemisorption, sensitivity and dynamic behaviour for different particle sizes at different temperatures and for different gas types and gas concentrations; additionally, the influence of various process parameters such as an in-situ oxidation process on the gas-sensing properties of gas sensitive films, based on monodisperse SnO_2 nanoparticles, is presented.

In order to characterise the chemisorbed species, the electrical resistance R is measured in different oxygen concentrations at temperatures within the

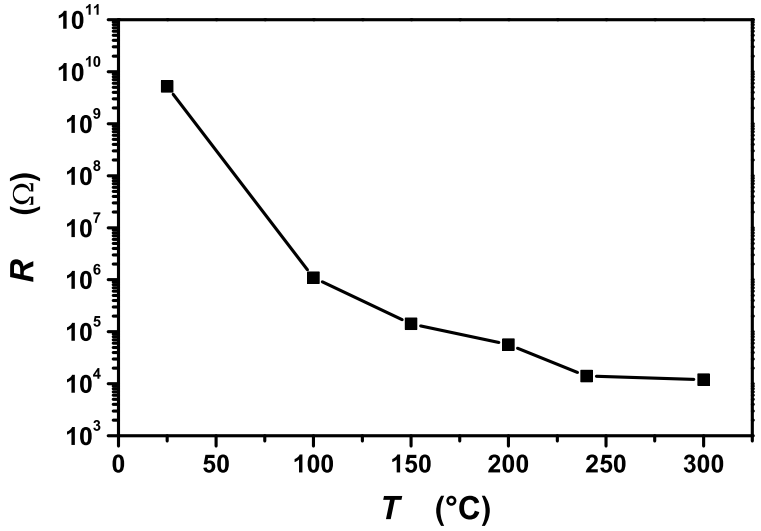

Figure 4.17: Resistance of a sample with D_{ms}=15 nm as a function of the temperature during annealing. The temperature of 300 °C is kept constant for 2 hours.

range of 50-300 °C. Using this method, the mean charge of the adsorbed oxygen atoms can be found [Hermann et al. [37]]. Additionally, the resistance is measured as a function of the temperature for a constant heating in different atmospheres to determine the temperatures at which different reactions between gas and sensing material occur. After characterisation of the particle-to-particle contact evolution, the gas-sensing characteristics of SnO_2 films based on monodisperse nanoparticles are investigated. The layers are prepared using the method described in Section 3.2. Four samples were prepared from nanoparticles having mobility diameters after sintering of D_{ms} = 10, 15, 20 and 35 nm (NF10, NF15, NF20 and NF35). Further particle and film properties, such as the standard deviation of the particle size distribution σ_{gm} calculated from DMNPS measurements and σ_{gT} from TEM measurements, relating to the surface density and the number of particle layers, are presented in Table 4.2. The electrical resistance R of all samples was measured in 1,000 ppm ethanol at 250 °C. It can be seen that the diameters, as determined from TEM D_{T} (9.6, 14, 19.8 and 34 nm for samples NF10, NF15, NF20 and NF35 respectively) match well with D_{ms}. The deposition conditions are chosen such that the estimated layer thickness of all samples is equal. The nanoparticles are deposited on microhotplates with interdigitated electrodes as described in Section 3.2.2. The resulting values of

	D_{mi} (nm)	D_{ms} (nm)	σ_{gm}	D_{T}	σ_{gT} (nm)	**density** (#/μm^2)	**thickness** (μm)	**R** (Ω)
NF10	15	10	1.12	9.6	1.09	$1.99{\cdot}10^6$	1.52	$2{\cdot}10^6$
NF15	25	15	1.11	14	1.08	$5.75{\cdot}10^5$	1.5	$4{\cdot}10^5$
NF20	33	20	1.08	18.8	1.05	$2.48{\cdot}10^5$	1.52	$4{\cdot}10^3$
NF35	75	35		34		$4.54{\cdot}10^4$	1.5	$3{\cdot}10^3$

Table 4.2: Characteristics of deposited SnO particles in the form of nanoparticle films used for gas-sensing investigations. The nanoparticle film thickness is assumed for a closed packed system.

the resistance of the annealed samples are also shown in Table 4.2. Clearly, the resistance increases sharply for smaller particle sizes. A similar effect was found by Xu et al., who explained this by the change in the ratio between the thickness of the space charge region and the particle diameter [Xu et al. [91]]. Furthermore, the influence of the in-situ and ex-situ treatment, such as annealing and oxidation, is measured. The gas-sensing properties in terms of sensitivity and dynamic behaviour are determined by measuring the time-dependent changes in resistance on altering the gas environment in the measurement chamber at operating temperatures varying from 100 to 300 °C. Ethanol and carbon monoxide are used as reducing gases and nitrogen oxide as an oxidising gas.

4.3.1 Study of particle-to-particle temperature-dependent contact

The large decrease in the resistance and the change in the contact type show that an annealing process up to 300 °C leads to a sintering process between particles. In this section the investigation of the electrical contact between size-selected SnO_2 nanoparticles is carrried out. The particle-to-particle contact formation is measured by means of I-V measurements. The I-V plot provides information about the contact type. For SnO_2, different contact types have been found [Göpel [33]]. Figure 4.18 shows two I-V plots for sample NF20. The sample was heated in 1,000 ppm ethanol. It can be seen that if the sample is annealed up to 150 °C for the first time, a Schottky contact is obtained. It should be taken into account that the I-V measurement also includes an electrode-particle contact. Nevertheless, if the sample is heated up to 250 °C the Schottky contact disappears and an ohmic contact is established. Once the contact type has changed to an ohmic contact the type does not change anymore and is independent of temperature;

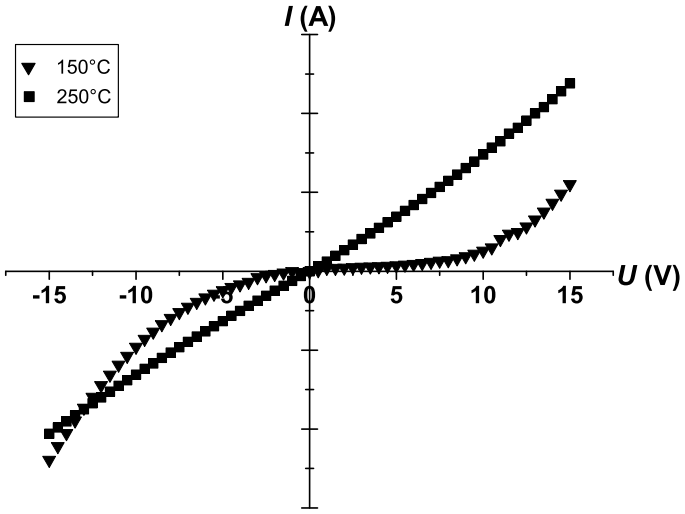

Figure 4.18: *I-V* characteristics of sample NF20 showing a Schottky contact at 150 °C and an ohmic contact at 250 °C.

this is due to a sufficient sintering process between the tin oxide nanoparticles. However, the shapes of the *I-V* curves do not change with the particle size indicating that the contact types are independent of the particle diameter. Consequently, to have not only a stable particle size but also a stable particle-to-particle contact, each sample has to be heated up to at least 250 °C.

4.3.2 Analysis of the chemisorption process at the surface of nanoparticle layers

As described in Section 2.1.2, the chemisorption effect is responsible for the gas-sensing mechanism of metal-oxide materials. In this investigation, the chemisorption process is measured by the electrical resistance as a function of the temperature at a constant heating rate. It is also possible to evaluate the charge of the adsorbed species on the surface of the semiconducting material (Section 3.4). Both experiments were carried out to confirm the gas-sensing mechanism for nanoparticle samples and to achieve basic information about the status of the gas sensor before reaction with a reducing or an oxidising gas.

Evaluation of the oxygen species after chemisorption

In order to investigate the chemisorption process of oxygen on the surface, the temperature dependence of the resistance at different oxygen concentrations in nitrogen was measured for samples NF10 (Figure 4.19) and NF20. The steady-state values of $1/R$ for sample NF10 are depicted in a log-log plot as a function of $p(O_2)$ at 200, 250 and 300 °C. The behaviour can be described by the equation [Herrmann et al. [37]]:

$$\frac{1}{R} \sim \frac{1}{R_0} \cdot p(O_2)^{-\frac{1}{n}} \tag{4.2}$$

A positive value of n shows the n-type behaviour of the SnO_2 nanoparticle samples because this behaviour shows the adsorption of oxygen resulting in a charge transfer mechanism and, therefore, in an increase of the electrical resistance. This means that the resistance of the SnO_2 nanoparticle films rises as the oxygen partial pressure $p(O_2)$ increases. If n is close to 4, anionic vacancies, as the main structure defects, act as a source of conduction electrons.

In literature two mechanisms involving oxygen doubly anionic (O^{2-}) and oxygen singly anionic (O^-) species have been proposed [Chang [8]]. It may also be mentioned here that n in the equation (4.2) signifies the value of the oxygen species responsible for the gas-sensing raction. The values of n=4 and n=2 correspond to the O^- and O^{2-} species respectively. Referring to the graph, a value of n=2.6 ± 0.1 is observed for sample NF10. The value n=2.6 indicates that both O^{2-} and O^- are involved in the chemisorption process at temperatures between 200 and 300 °C. For sample NF20 the value of n observed in the present case in temperatures ranging from 200 °C to 250 °C was n=3.3. That means that the charge transfer process during chemisorption depends also on the particle size of the sample, resulting in different ratios of the amounts of adsorbed O^{2-} and O^- species and, therefore, different thicknesses of the charge-depletion layer.

If the oxygen pressure is reduced, the nanoparticle surface becomes devoid of oxygen species. The anionic species interact with the semiconductor surface by taking excess electrons from the n-type semiconductor; thus, removal of these species from the surface is equivalent to increasing the electron concentration near the surface of the nanoparticles. The response of $1/R$ varies inversely to the oxygen pressure and quite rapidly for the particle sample. This can be explained by a combination of a high surface area and good electrical interconnections between particles.

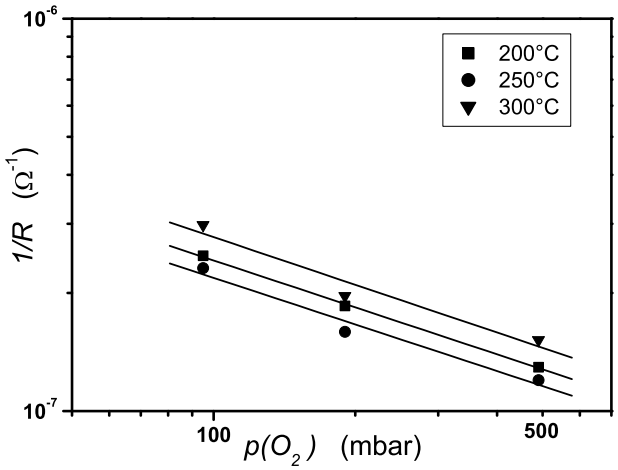

Figure 4.19: Sample NF10: inverse resistance as a function of oxygen partial pressure at different temperatures.

Study of electrical properties in different atmospheres at a constant heating rate

If a metal-oxide semiconducting material is heated, this leads to a decrease in the electrical resistance at T<100 °C [Lantto [50]]. In the case of metal-oxide gas sensors, a chemisorption mechanism in an oxygen atmosphere which takes place at higher temperatures causes a decrease in the charge carriers due to the charge transfer mechanism at the surface and, therefore, an increase in the resistance at >100 °C (Section 2.1.2).

In order to study the temperature at which the chemisorption process is dominant, firstly, resistance measurements were carried out by heating sample NF10 from room temperature up to 300 °C at a constant heating rate of 6 °C/min in various oxygen concentrations (10, 20 and 50 vol%). Figure 4.20 shows that for all oxygen concentrations there is a decrease in resistance as the temperature increases up to 150 °C. Over 150 °C, an increase in resistance is observed; this is more noticeable for higher oxygen concentrations. This phenomena confirms the investigations of metal-oxide gas-sensing materials, referred to in literature, for temperature-dependent physisorption and chemisorption processes at the surface (Section 2.1.2): below 100 °C, oxygen molecules are physisorbed; this does not affect the electrical properties of the semiconductor material and, thus, the decrease observed in the resistance corresponds to the decrease in the resistance of an n-type semiconductor ma-

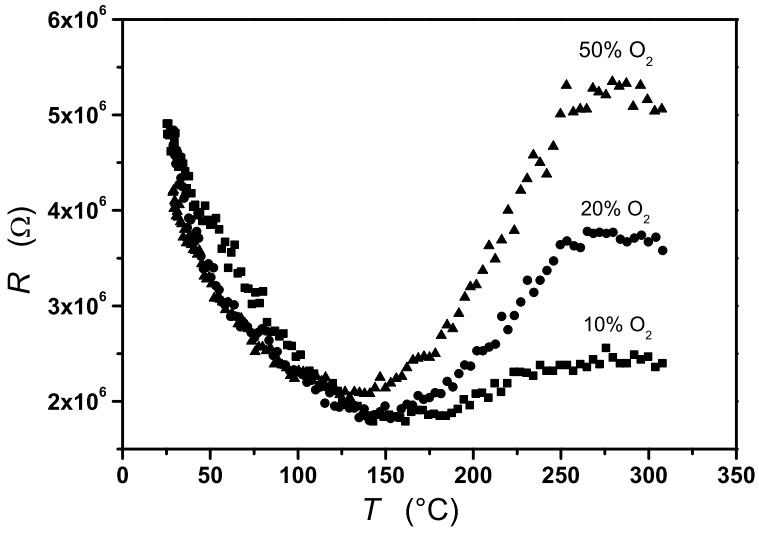

Figure 4.20: Sample NF10: resistance as a function of temperature at different oxygen concentrations (heating rate 6 °C/min).

terial as the temperature increases. This is supported by the observation that these changes are not dependent on the oxygen concentration. Above 100 °C, chemisorbed oxygen acts as an electron acceptor and creates an O_2^- species on the surface. Electrons on the semiconductor surface are transferred to the adsorbed oxygen species through a charge transfer mechanism. The negative charge generates a depletion layer and a Schottky potential barrier is formed on the metal oxide surface [Weisz [88]]. By means of electron paramagnetic resonance (EPR) investigations, together with conductance measurements, it was shown that at T>150 °C, an O_2^- to O^- transformation takes place [Chang [8]], leading to a further increase in the resistance. Figure 4.20 also shows that the equilibrium of chemisorption gas is reached applying a steady-state resistance value T>250 °C. Note that at this temperature also an ohmic particle-to-particle contact is also established (Figure 4.18). Furthermore, similar measurements as shown in Figure 4.20 were taken for different particle sizes and in different gas atmospheres to understand the adsorption and desorption mechanism of oxygen for various gas types.

Figure 4.21 demonstrates the slopes for two particle diameters. It can be seen that the electrical resistance of the 20 nm particle layer starts to increase at higher temperatures (170 °C compared to 150 °C for NF10). This means that the adsorption of oxygen on the SnO_2 surface depends not only on

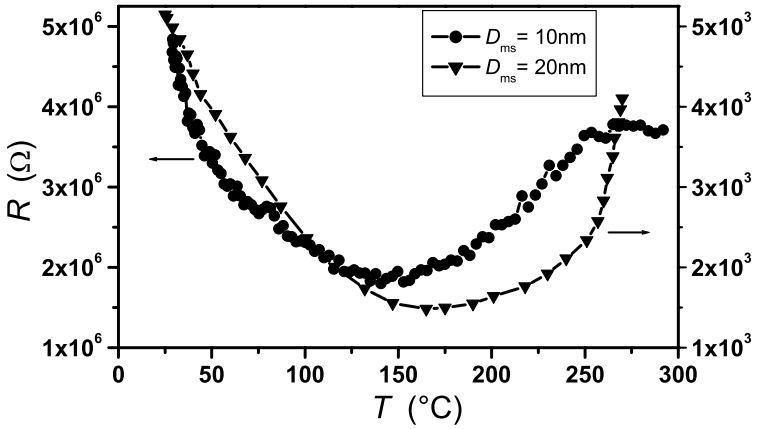

Figure 4.21: Resistance as a function of temperature at 20 vol% oxygen (heating rate 6 °C/min) for samples NF10 and NF20.

the thermodynamic circumstances but also on the mean particle size of the sensitive layer too. Also, the resistance does not reach a steady-state value at the maximum temperature, indicating that samples with a higher surface to volume ratio reach the equilibrium more rapidly. In another experiment, the resistance change as a function of the temperature was observed in a reducing atmosphere. The decrease in resistance, as the temperature of the nanoparticle sample in 1,000 ppm ethanol in synthetic air rises is shown in Figure 4.22. No chemisorption process can be detected by means of the resistance, although 99.9 % of the surrounding atmosphere is synthetic air. This means that if an oxygen molecule is adsorbed at the surface, it is removed immediately by the subsequent reaction with the ethanol molecules, i.e. the desorption process of oxygen dominates that of adsorption. Nevertheless, the adsorption and desorption processes at the surface of the gas-sensing material always reached an equlibrium, where both processes could not be detected separately. This means that in 1,000 ppm ethanol the equilibrium of the chemisorption process has been shifted towards desorption. Consequently, the electrical resistance has its highest value at room temperature, decreases to its lowest value at 170 °C and remains fairly constant up to 260 °C. This behaviour is independent of the nanoparticle size of the sample selected in this investigation (Table 4.2). Similar results have been found for nanoparticle samples in pure nitrogen where no chemisorption process takes place, and in other reducing atmospheres.

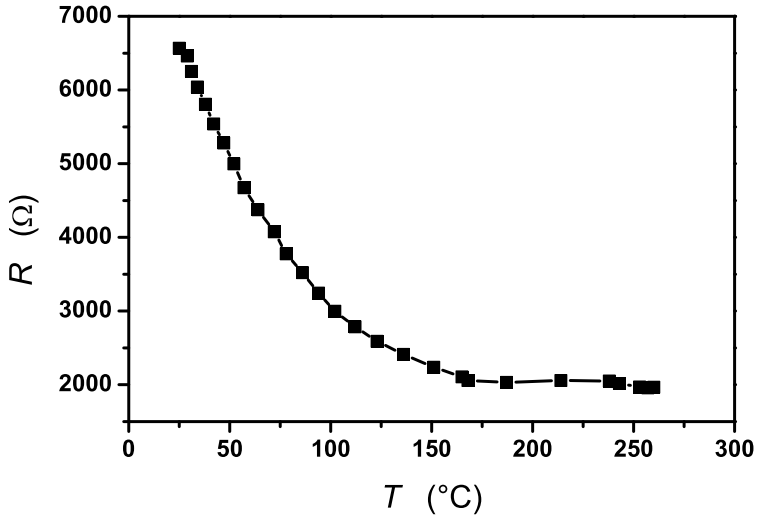

Figure 4.22: Resistance as a function of temperature in 1,000 ppm ethanol in synthetic air (heating rate 6 °C/min) for sample NF20.

If the nanoparticle samples are introduced into an oxidising atmosphere, the reactions differ because additional formations of oxygen adsorbates, due to the presence of an oxidising gas, increase the thickness of the space charge region (Section 2.1). Therefore, the conductivity decreases with increasing temperature. Figure 4.23 shows an example of the resistance and temperature as a function of time for the NF15 sample in 1,000 ppm NO. NO starts reacting at room temperature with the SnO_2 surface, as shown in equation 2.5). At this temperature, the resistance increases by about two orders, reaches its maximum at 160 °C and then decreases until the maximum temperature has been reached. This characteristic is explained by the desorption of NO_2 which occurs above 160 °C. Accordingly, gas-sensing measurements with NO gas molecules should not be done at higher temperatures because this would be followed by a lower surface coverage and, consequently, by smaller sensitivity values since the reaction conversion is lower. It should be taken into account that the nanoparticle SnO_2 sensor reacts with NO at room and higher temperatures, but a recovery process will require temperatures above 150 °C to remove NO_2 from the surface of the metal-oxide. The stability and reproducibility of this gas sensor for NO at room temperature is, thus, unsatisfactory.

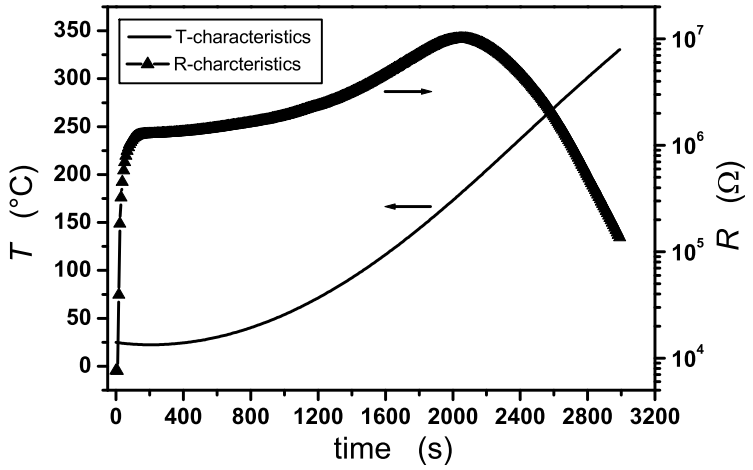

Figure 4.23: Temperature and resistance as a function of time in 1,000 ppm NO (heating rate 6 °C/min) for sample NF15.

4.3.3 SnO_2 nanoparticle gas-sensing behaviour

The addition of a reducing gas, such as ethanol, methane, carbon monoxide or hydrogen, leads to surface reactions which cause a decrease in the surface coverage of the oxygen species and, as a consequence, a decrease in resistance at temperatures above 150°C (Section 2.1). For gas-sensing research, it is important to know how the gas-sensing material reacts for different gas types and gas concentrations. Each gas type can have an optimum operating temperature and even an optimum material structure: these parameters must be found and applied to ensure that the best values for sensitivity and dynamic behaviour are obtained. For example, rank-order filtering of sensor array data can significantly improve gas discrimination capability [Wilson et al. [90]]. This investigation has concentrated on the characterisation of gas-sensing properties in ethanol and the influence of operating temperatures and process parameters, i.e. particle size, in-situ and ex-situ oxidation and annealing treatment.

Sensing behaviour in a reducing atmosphere

Ethanol has been used predominantly as a reducing gas in this investigation. Gas-sensing properties are measured at operating temperatures 150-300 °C for the samples which were shown in Table 4.2. The particle layers were produced by generating SnO nanoparticles, followed by a post-annealing process

at 300 °C in synthetic air.

To determine the gas-sensing properties of SnO_2 films based on monodisperse nanoparticles, the resistance transients observed for sample NF20 at 300 °C are shown as an example in Figure 4.24. The "on"-state shown in the graph corresponds to the introduction of ethanol diluted in synthetic air and the "off"-state to the introduction of pure synthetic air. The measured

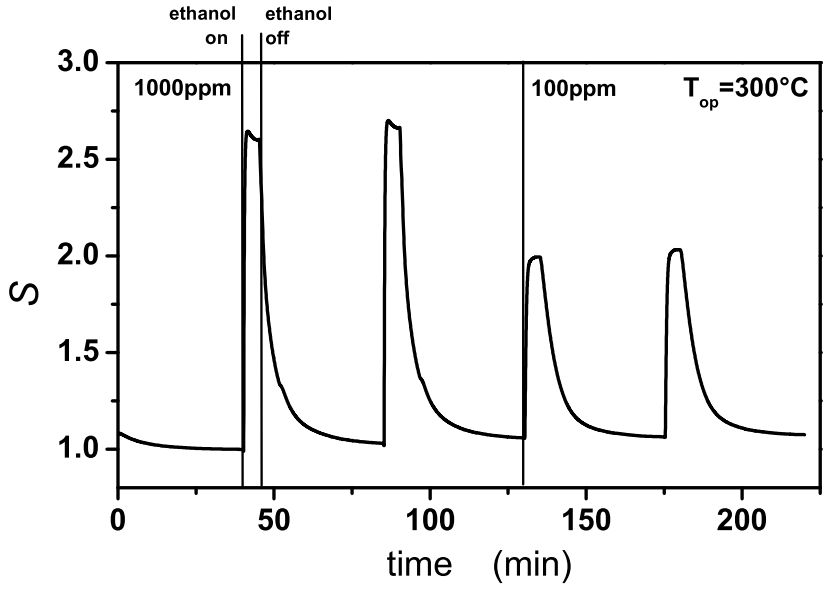

Figure 4.24: Response transients of sample NF20 on switching the ethanol flow on and off (T=300 °C; ethanol concentration 1,000 ppm).

change of the resistance on the introduction of ethanol has a time constant of τ=38 s and the introduction of synthetic air τ=400 s. The real time constants will be slightly lower as the time needed for exchanging the gas atmosphere in the measurement chamber (∼8 s) is included in the measured value. The resistance transients are reproducible. Decreasing the ethanol concentration from 1,000 to 100 ppm leads to a decrease in the sensitivity from 2.7 to 1.9 and an increase in the time constant from 38 to 63 s. If the operating temperature is lowered by 50 °C, the sensitivity decreases for 1,000 ppm to 1.8 and for 100 ppm to 1.35, and the sensor reacts more slowly. This means that for gas-sensing applications it is always important to keep the temperature constant.

By using this measurement system it is possible to adjust the operating temperature within a variation of 1% (Section 3.1.1). Sensitivity, as a function of the operating temperature, was studied for two different samples, NF10 and NF20, in 1,000 ppm ethanol (Figure 4.25). The samples are not oxidised in the gas phase. Each data point represents the sensitivity values on a single microhotplate. Figure 4.25 illustrates the increase of the sensitivity as the operating temperature rises for both samples. Clearly, the maximum sensitivity value is for both samples at temperatures higher than 250 °C. If sample NF10, having a smaller particle size, is used, the sensitivity value is higher at all operating temperatures between 100 °C and 250 °C. This measurement confirmed the theory about size-dependent gas-sensing properties (Section 2.2) and will be discussed in more detail in Section 4.3.4.

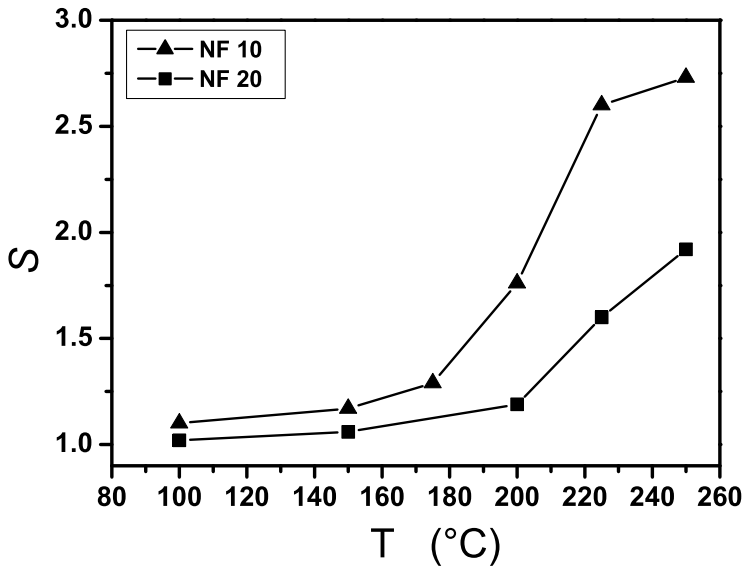

Figure 4.25: Gas sensitivity of sample NF10 and NF20 as a function of the operating temperature in 1,000 ppm ethanol.

Behaviour of in-situ oxidised SnO_2 nanoparticle layers

To vary the sensitivity of a metal-oxide gas sensor, different methods exist, such as doping, producing a second metal-oxide phase in the sensing layer and, as presented in this investigation, varying the particle size. In this section, an easy way to increase the sensitivity will be discribed. It has been

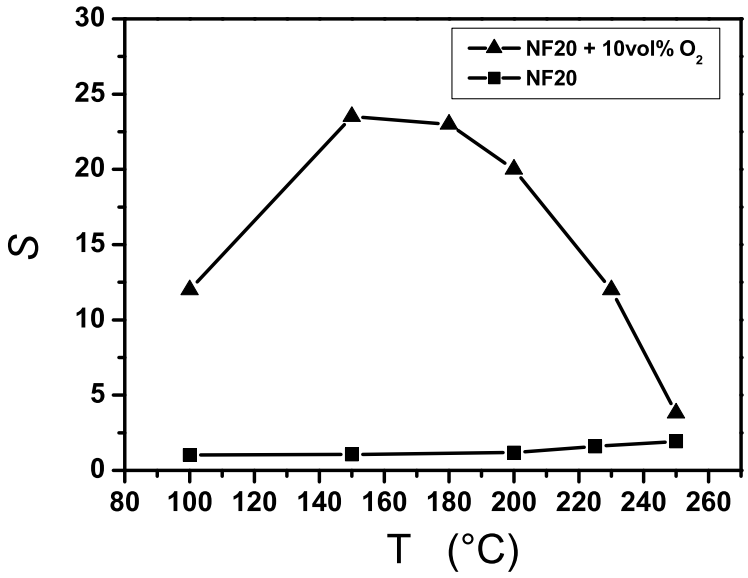

Figure 4.26: Gas sensitivity of NF20 and in-situ oxidised NF20 as a function of the operating temperature in 1,000 ppm ethanol.

demonstrated how the variation of the process parameter during the synthesis and also in post-treatment processes can influence the material structure, i.e. the particle size, particle film formation and chemical composition. Here, the influence of the sensitivity due to an in-situ oxidation process and, therefore, the influence of the chemical composition will be shown and the effect will be explained by the material characterisation results obtained in Section 4.2.

Figure 4.26 shows sensitivity as a function of operating temperature for two different samples: NF20 and NF20 in-situ oxidised. Both samples were annealed after deposition in synthetic air at 300 °C. Compared to an unoxidised sample in the gas phase, the maximum sensitivity of an in-situ oxidised SnO_2 nanoparticle sample is nearly one order higher and the maximum sensitivity shifts towards a lower operating temperature in 1,000 ppm ethanol. This effect can be explained by means of the chemical composition results of the whole nanoparticle layer and the surface. From XRD measurements (Section 4.2.2), it was established that the introduction of 10 vol% oxygen in the sintering furnace causes an oxidation of SnO, followed by a crystallographic structure change from tetragonal SnO to a nearly complete tetragonal SnO_2 phase including a small amount of the orthorhombic structure. It is well

known that the tetragonal SnO_2 phase is thermodynamically more stable [Suito et al. [83]]. If the SnO nanoparticle layers are heated after deposition at 300 °C in synthetic air, no change in the crystallographic structure is obtained. If the SnO nanoparticles are not in-situ oxidised and post-annealed at 300 °C in synthetic air, an orthorhombic SnO_2 phase is detected. This means that the crystallographic structure of SnO_2 has a major influence on the sensitivity. Obviously, although the particles are heated for only 0.5 s in the sintering furnace at a temperature of 660 °C, this treatment has a much greater effect on the development of a stable crystallographic structure than that in a post-annealing process of long duration at 300 °C in synthetic air. It should be mentioned that this sensitivity increase effect can be achieved by a simple change in the process conditions.

The gas-sensing mechanism takes place at the surface of the sensing material. The different gas-sensing properties mentioned above can also be explained by different surface chemical compositions. Therefore, AES as a surface sensitive investigation method was used to measure the surface stoichiometry value (Section 3.3.3); this value provides qualitative information about the number of oxygen vacancies at the surface of SnO_2 nanoparticle samples and, consequently, about the number of adsorbable oxygen places. AES measurements show that an in-situ oxidised sample has a lower stoichiometry value ($SnO_{1.85}$) on the surface compared to a sample without in-situ oxidation after annealing at 300 °C in synthetic air (Figure 4.16). Accordingly, in-situ oxidised samples have a larger number of oxygen vacancies at the surface. This means that if more oxygen atoms adsorb at the surface a higher reaction rate is achieved leading to higher sensitivity values. Equation (2.8) confirms this effect because a lower stoichiometry results in a higher concentration of ionised donator atoms N_d and, therefore, in a larger value for the potential barrier V_s and the thickness of the space charge region L_{SC}.

These results illustrate that surface stoichiometry and crystallographic structure influence the gas-sensing properties of SnO_2 nanoparticle films. It should also be taken into account that an orthorhombic SnO_2 has a different electrical band structure compared to the tetragonal phase: this will influence the thickness of the space charge region and, thus, the value of the sensitivity. However, the change in the band structure was not proved in this investigation.

4.3.4 Influence of particle size on gas-sensing properties

In this section, size-dependent gas-sensing properties (sensitivity and dynamic behaviour) are investigated. The samples are prepared without in-situ oxidation and have the same estimated layer thickness (Table 4.2). Figure 4.27 compares the response transients of nanoparticle films (NF10, NF20 and NF35) at 300 °C with particles sizes D_{ms}=10, 20 and 35 nm in 1,000 ppm ethanol. As expected from theory (Section 2.4), sensitivity towards ethanol increases as the particle size decreases. Moreover, concerning the dynamic behaviour, the value of τ diminishes with decreasing particle size; τ=10 s for NF10 and τ=38 s for NF20. In the case of sample NF35, it was difficult to estimate τ due to a small change in the resistance on gas exposure. The fast response for samples NF10 and NF20 also indicates that the SnO_2 nanoparticles are properly connected in the layer. Due to the high reactive surface of the nanoparticles, the measured response time values of the gas sensors are smaller for ethanol compared to other studies and the dynamic behaviour is mainly influenced by the layer surface [Chung et al. [13]].

Figure 4.28 presents sensitivity of nanoparticle films as a function of the particle size in the range 200-300 °C. The sensitivity increases with decreasing particle size as established in Figure 4.27. A temperature increase leads also to an increase in the sensitivity because more oxygen molecules are chemisorbed [Kennedy et al. [46]]. Another effect of the rising temperature is that an oxygen species transformation from O_2^- to O^- takes place at approximately 200 °C [Chang [8]]: this leads to higher charge transfer rates per oxygen atom and, thus, to higher sensitivity values. As mentioned in Section 2.3, the decrease in the surface state density for smaller particle sizes also leads to an increase of the sensitivity due to a lower Fermi-level pinning.

Similar results were obtained by changing the mean particle size in the range 5 nm to 32 nm via the calcination temperature and by using metal additives [Xu et al. [91]]. In addition to the wide particle size distribution observed in Xu's samples, the process parameters responsible for size control must have caused microstructure and composition variations so that the conclusions reached concerning the size dependence of gas sensitivity might not be conclusive.

It should be emphasised again that, in this investigation, the size distribution is narrow, the particle size is the only variable and different particle sizes have been prepared separately, i.e. no post-annealing or doping was

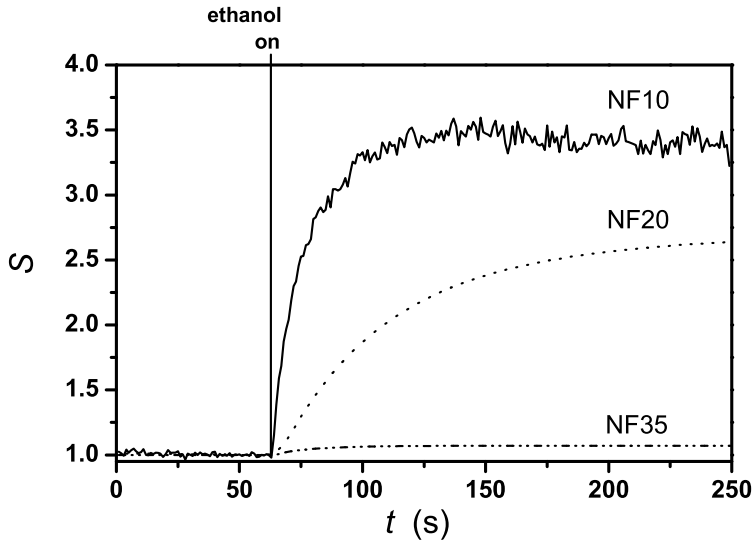

Figure 4.27: Response transients of samples NF10, NF20 and NF35 after switching the ethanol flow on (T=300 °C; ethanol concentration 1,000 ppm).

carried out to change the particle size; also, that the microstructure of the layers of different particle sizes is comparable and does not change as a result of annealing up to 300 °C. It is clear that the variations of S and τ observed are merely a consequence of nanoparticle size dependence. As mentioned earlier, a sharp increase in the resistance value is observed for sample NF10 with a particle size of D_{ms}=10 nm in comparison to samples NF15, NF20 and NF35 with D_{ms}=15, 20 and 35 nm respectively. The Debeye length L_{D} is estimated to be 3 nm [Ogawa et al. [67]]. In this investigation, the Debye length appears to have a larger value (approximately 7-8 nm). This is supported by the fact that sensitivity is a function of particle size in the 10-35 nm size range especially at sizes below 20 nm. With smaller particle sizes (2 less than D_{ms}), the particle core is the major resistance controlling part of the particle chain and the sensitivity is known to be a function of the nanoparticle size. The concentration and energy position of absorption sites in the band gap of the semiconductor are also affected significantly. Additionally, surface state density decreases with decreasing particle size, leading to less Fermi-level pinning and, consequently, to an increase in the charge depletion layer [Malagu et al. [57]]. The correlation between surface state density and particle size has been demonstrated by means of a model using the Poisson

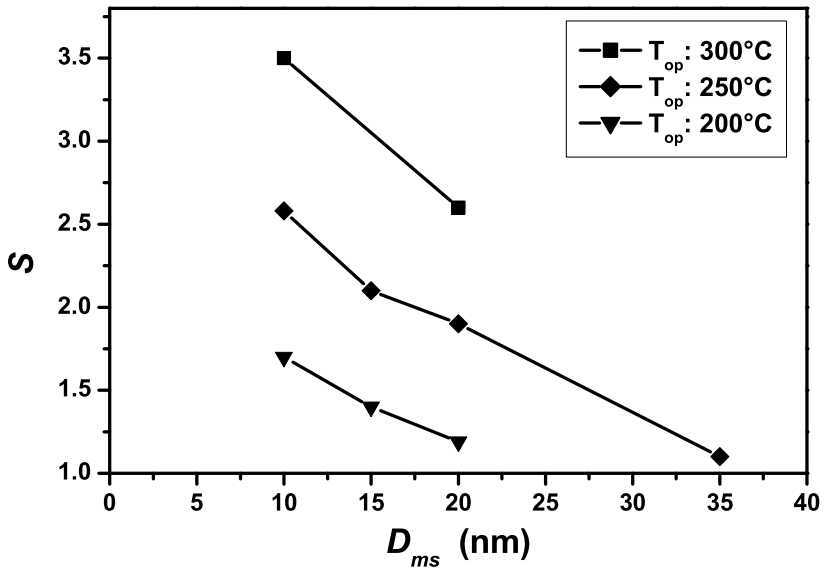

Figure 4.28: Sensitivity as a function of the particle size at different temperatures in 1,000 ppm ethanol. The layer thickness for all the samples is 1.5 μm.

equation and, experimentally, by means of scanning tunnelling spectroscopy (STS) measurements [Maffeis et al. [55]]. Together, these factors result in improved sensitivity and dynamic behaviour of the nanoparticle films towards the gas molecules in terms of higher sensitivity and low response time for smaller particle sizes (especially those below D_{mi}=20 nm).

4.4 Improvement of nanoparticle SnO_2 gas sensors

For further characterisation of gas sensors based on metal-oxide materials not only sensitivity and response behaviour are of interest. It is also important to have a sensor which has different sensitivity values for different gas types and also identifies gas types for practical applications. In this section the initial measurement results concerning this topic are presented.

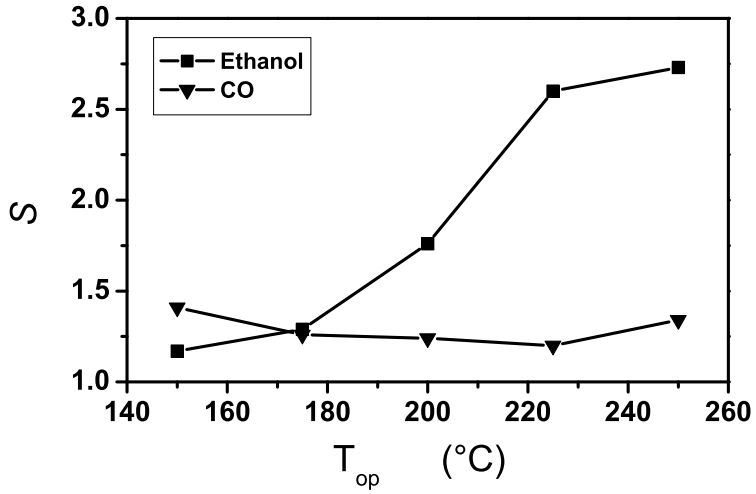

Figure 4.29: Gas sensitivity of NF10 as a function of the operating temperature in 1,000 ppm ethanol and 1,000 ppm CO.

4.4.1 Nanoparticle gas-sensing behaviour in different atmospheres

Although the gas-sensing work in this investigations is concentrated on ethanol as the detectable gas, other gases also react with the SnO_2 particle surface, resulting in a measurable resistance change. Furthermore, it is important to determine the sensing behaviour of other gases in order to investigate possible selective properties of a SnO_2 nanoparticle gas sensor. The first approach towards a selective sensor is, in most cases, to establish different sensitivity values at the same operating temperature but with the same gas concentration for different gas types. This phenomenon is depicted for sample NF10 in Figure 4.29 for 1,000 ppm ethanol and CO of equal concentration. Each gas was detected separately with the same gas sensor. The results show that sensitivity for CO has a low value and, therefore, is difficult to be identified at temperatures between 150 °C and 250 °C because sensitivity is usually below 1.4 and does not depend significantly on temperature. Compared to CO, ethanol can be detected at temperatures above 180 °C with sufficient sensitivity. The same measurements have been done for CH_4 whose sensitivity values are similar to CO. Consequently, it should be possible to distinguish between ethanol and CO at the same operating temperature if the gas concentration is known.

4.4.2 Study of gas identification by means of response transients

As mentioned in the last section, there is increased interest nowadays in the production of a selective gas sensor. Many different methods have been followed: for instance, film thickness has a great influence on sensitivity. Sakai et al. assumed that the molecular weight of the gas is responsible for different sensitivity values [Sakai et al. [74]]. They explained this by using the Knudsen diffusion equation assuming that the gas reaction follows first-order kinetics with respect to the gas concentration and, therefore, a calculation of the concentration profile for different gases in the pores of the sensing material can be made (Section 2.4.2).

In this investigation, gas recognition was established by means of response transients for different gas types. This method analyses the slope of the electrical resistance versus time for the reaction and recovery processes. Due to the fact that the chemical reaction of the gas with the sensing surface can produce intermediate products and that each part of the reaction process is time dependent, the oxygen adsorption and desorption reaction of this effect can be followed. One example of this measurement is given in Figure 4.30. 1,000 ppm methane is introduced into the measurement chamber and resistance measurements are carried out with the NF20 sample at 270 °C. The reaction and recovery processes are repeated four times. If the response transient is compared with the transient of ethanol depicted in Figure 4.24, it is established that introduction of methane is followed by two minima and a stable resistance value is observed after ~ 40 min. The first minimum appears directly after introducing methane and the second after 800 s. The gas-sensing characteristic of methane in these conditions is reproducible. The response transient of ethanol has only one minimum and a constant value is reached for sample NF20 after ~ 2 min. The recovery process for both gas types is similar.

If hydrogen is detected in the same sample under the same conditions (gas concentration; temperature), the slope of the response transient is different compared to that of methane or ethanol. The response transients for hydrogen are presented in Figure 4.31. Introduction of H_2 is followed by a rapid decrease in the resistance but the resistance minimum does not reach a steady-state value immediatly after the minimum. The resistance increases and reaches a constant value after ~ 30 min. No further resistance minima were detected. The recovery process is also different compared to that using ethanol and hydrogen. Introduction of synthetic air is followed by an increase

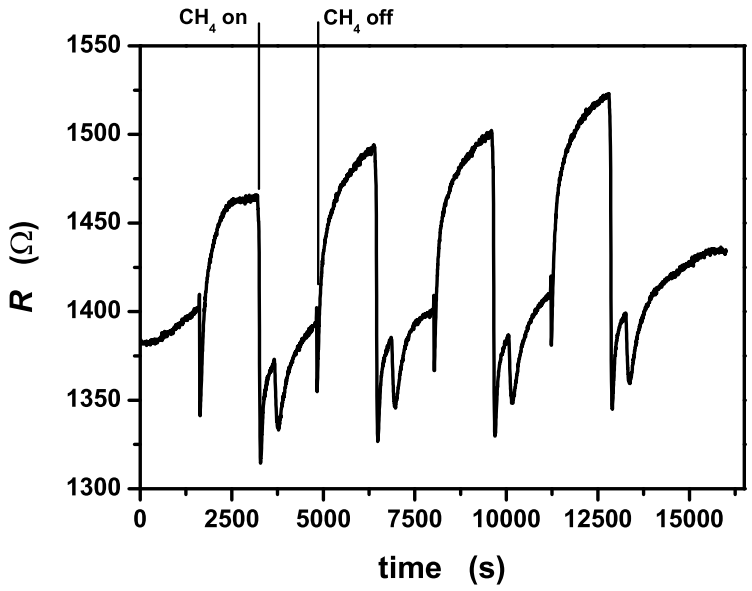

Figure 4.30: Response transients of sample NF20 on switching the methane flow on and off (T=270 °C; concentration 1,000 ppm).

in the resistance; this is to be expected, but the resistance value reaches a maximum and then decreases. A constant value is reached after ∼40 min.

The results in this section indicate that it is possible to identify the gas type from the slope of the response transients. Further investigations are necessary to interpretate these results in a detailed form. Clearly, the response transients depend on the diffusion coefficient of the gas molecules with different molecular masses, the activation energy for the surface reaction and the electrical properties of the sensing layer itself. The reaction velocity is also dependent on the temperature and gas concentration. In order to apply a nanoparticle gas sensor, cross-sensitivity, i.e. gas-sensing behaviour for more than one gas type introduced into the measurement chamber, should be the subject of future investigations.

4.4.3 Further methods of understanding and improving SnO_2 gas-sensing devices

Up to now, *I-V* measurements were carried out. For more detailed information about the effect of chemisorption on the properties of the charge

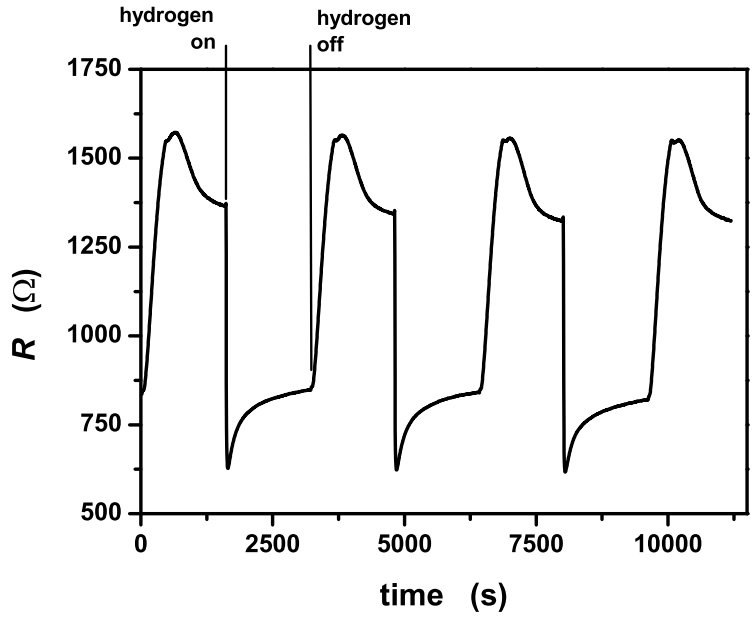

Figure 4.31: Response transients of sample NF20 on switching the H_2 flow on and off (T=270 °C; concentration 1,000 ppm).

carriers dependent on the particle size or other process parameters, van der Pauw and Hall measurements are necessary. With these methods it is possible to obtain information about the charge carrier concentration and mobility separately at different temperatures and various gas atmospheres. The gas-sensing measurement system has already been configurated for these measurement types. The measurement chamber fits directly between the pole caps of the Hall magnet and is made out of aluminium to ensure a homogeneous magnetic field through the whole measurement chamber. Additionally, the feedthrough for the electrical characterisation has four contacts so that Hall measurements can be carried out. First results show that DC Hall measurements are possible using nanoparticle samples prepared by means of the method described in Section 3.2.1[Sentürck [79]].

In order to improve gas-sensing properties, doping of the gas-sensing material or a mixture of metal-oxides is a promising method because the doping element, such as platinum, palladium or silver, decreases the activation energy of the chemisorption process. Doping of tin oxide enhances sensitivity and decreases the response time [Schmid et al. [77] and Promsong et al. [64]].

If the activation energy is reduced, the power consumption during sensing is also reduced. Doping can be done by means of the gas phase synthesis process (Section 3.2) using another furnace, connected to the set-up, for the doping material (Figure 3.4).

Nanoparticles not only enable sensors with different sensitivities to be built, they also make it possible to reduce the size of the sensor device. For analysing a gas mixture, several sensors with different sensitivities for the same component are fabricated nowadays [Lee et al. [52]]. Normally, these dissimilar sensitivities are obtained by operating similar sensors at different temperatures. This requires a complicated temperature control and necessitates larger equipment. It is better to produce a parallel set of sensors with different sensitivities and operate them at the same temperature using sensing layers with different chemical compositions or different particle sizes (Figures 4.26 and 4.28). Additionally, the different response transients can help to fabricate a selective multi gas sensor array (Fig. 4.30). In this investigation, the diameter of the deposition spot was reduced to $\sim$500 μm. Therefore, it is possible to produce a single device with more than 1 sensing area by means of a combination of microsystem technology on a 4 mm^2 microhotplate with several interdigitated electrode structures and an upgrading of the gas phase synthesis process.

Chapter 5

Concluding comments

In order to investigate the dependence of gas-sensitive properties of undoped tin oxide (SnO_x) films based on monodisperse tin oxide nanoparticles films, a new thin film synthesis technique was developed; it comprises several independent but controllable steps and allows a control over particle and film properties. These steps include particle size-fractionation, high-temperature in-flight oxidation and post deposition treatment, leading to different chemical composition characteristics.

Monocrystalline and quasi-monodisperse (σ_g<1.1) tin oxide nanoparticles are formed in mean crystallite sizes adjusted between 10-35 nm. Subsequently, they are deposited at room temperature on different substrates, depending on the characteristics to be measured, forming a thin porous layer. TEM, AES, STM, XRD and RBS measurements were carried out to obtain information about the morphology and the chemical composition of the tailored nanoparticles and nanoparticle films. This experimental procedure ensures that particles of different sizes have undergone the same thermal and chemical treatment.

For gas-sensing analysis, annealing of the particle layers is essential to form conducting necks and to activate the reactive surface. The maximum post-annealing temperature is 300 °C. It has been established in these experiments that annealing of the layer in oxygen does not change the particle size but decreases the resistance at room temperature over several orders of magnitude. It is surmised that sintering necks are formed which facilitate electrical transport and that, due to the in-flight temperature treatment and the uniform particle size, the nanoparticle film is stable against grain growth. This is in contrast to the usual practice of varying the grain size by means of the synthesis conditions or by changing the annealing temperature.

For the application of nanoparticle layers as gas-sensing films in particular, microhotplates with an interdigitated electrode pattern, a heating layer and a temperature sensitive resistance for the control of the operating temperature are used, allowing a maximum temperature of 300 °C. The buried geometry of the electrode pattern is especially designed for the uniform deposition of nanoparticles.

The fully automated gas-sensing measurement set-up described in this investigation offers a simultaneous investigation of basic electronic parameters and important practical gas-sensing parameters and, therefore, is suitable for investigations of nanoparticle samples. The main advantage of this set-up is that measurements can be done in a wide range of temperatures from room temperature to 300 °C, gas ambient and gas concentration levels (10-10,000 ppm) and for long periods of time. The set-up can be used to measure high resistance (10^8-$10^{10}\,\Omega$) nanoparticle samples.

The basic gas-sensing mechanism of SnO_2 films, composed of different particle sizes and equal film thickness, were measured in the temperature range of 200-300 °C. The particle layers show the well known temperature-dependent behaviour of the resistance of an n-type tin oxide semiconductor in an oxygen atmosphere, indicating that different oxygen species are involved in the chemisorption process.

For the first time, it has been demonstrated conclusively that using smaller tin oxide particles in the size range 10-35 nm leads to higher values of sensitivity for ethanol vapour and a more rapid response on changing gas conditions. The effect is especially clear for particles of 20 nm or less.

In addition, the effect of the in-situ and ex-situ treatment on the chemical composition has been studied. It has been found that these treatments can cause the formation of different crystallographic structures and different surface stoichiometry values. The in-situ oxidised and post-annealed (at 300 °C) particle layers have smaller surface stoichiometry values ($SnO_{1.8}$) and a different SnO_2 crystallographic structure compared to those of unoxidised samples (SnO_2), resulting in higher sensitivity and a shift of the maximum sensitivity to lower operating temperatures.

Future investigations should concentrate on detailed electrical measurements to identify the properties of the charge carriers in the volume and at the surface of the nanoparticle layer. Furthermore, as the results in this investigation

have been established using undoped SnO_2 particles, similar measurements should be carried out with doped particles or by means of multi-sensor arrays. This is possible by means of small variations in the synthesis set-up. The measurement system itself has already been constructed to determine resistance and conductivity as well as the charge carrier concentration and mobility of nanoparticle samples in a single measurement chamber.

Appendix A

Microhotplates for gas-sensing measurements

The microhotplate substrate used for gas-sensing analysis of nanoparticle layers is introduced in Section 3.1. The sequence of the fabrication process is discussed below. However, the microhotplate is made out of several layers by means of microsystem technology based on silicon. Additionally, the set-up to control the operating temperature is described.

A.1 Fabrication of microhotplates by means of microsystem technology

This section describes the processes used to fabricate microhotplates for the characterisation of SnO_2 layers based on monodisperse nanoparticles. The microhotplate is a multilayer substrate which consists mainly of an interdigitated electrode pattern, a heating layer and a temperature sensitive resistance (Figure 3.1). Microsystem technology is required in order to be able to measure a sufficient resistance for gas-sensing analysis of nanoparticulate samples.

A.1.1 The p-Si layer

For obtaining the p-Si layer, epitaxial growth, combined on a pure silicon wafer with a dopant gas containing an acceptor element from the third main group such as B_2H_6, is applied. During an epitaxy process, the chemical compound in the gas phase containing Si is lead into a tube. The tube contains pure silicon wafers which are heated to the process temperature of about 1,200 °C. Predominantly silane (SiH_4) and chlorosilanes ($SiCl_4$, $SiHCl_3$,

SiH_2C_{12}) are used as reaction gases, together with the carrier gas H_2. The epitaxy process is carried out above 1,200 °C. During this process reaction gas decomposes to silicon and gaseous Cl_2 or HCl. Si deposits on the substrate surface. The reaction gas is diluted with an inert carrier gas in order to avoid a breakdown of the molecular species prior to the deposition. Furthermore, small concentrations of phosphine PH_3 for n-type doping are added to obtain appropriate doping of the epitaxial deposited layers. The dopant concentration is usually 10^{14} to 10^{20} atoms/cm^3. Higher concentrations cannot be achieved with dopants because this would exceed the silicon solubility limit.

In epitaxy, the deposition of the atoms takes place initially on the surface nucleation sites. These are generally corners and edges of incomplete crystal planes. Therefore, these planes are preferentially completed by deposition before a new crystal layer grows. A uniform growth of a single crystal epitaxial layer is ensured [Menz et al. [60]].

A.1.2 The SiO_2 layer

The electrically isolating oxide layer is produced by dry thermal oxidation in the open tube process in a pure oxygen atmosphere. The p-Si wafer is transferred into a quartz tube which is heated in a three-zone resistance furnace at a constant process temperature of approximately 1000 °C. The wafers are fixed vertically by special bins, so-called "carriers", running into the tube slowly at ∼700 °C. Afterwards, the temperature is increased in a 10 °C/min step until the process temperature is reached.

In order to achieve an oxide thickness of d_{ox} the following model, valid for both oxidation methods, can be used:

$$d_{ox} = \sqrt{((\frac{A^2}{4}) - B(t - t_0))} - \frac{A}{2} \tag{A.1}$$

A and B are constants dependent on the temperature and crystal orientation;, t_0 is the equivalent time duration for the oxide thickness already present due to the reaction at room temperature; and t is the process duration.

A.1.3 The nitride layer

In order to prevent further growth of the SiO_2 layer caused by the high operational temperature of 350 °C, a nitride layer as isolation layer and diffusion barrier are deposited on SiO_2. Additionally, a silicon nitride layer, together

with a phosphor silicate glass (PSG), is used because the thermal conductivity is very low. Consequently, the power consumption for heating is reduced.

A.1.4 The poly-Si layer

The poly-Si layer acts as a heating resistor. In order to maintain its electrical stability, a possible further migration of the oxygen molecules from the SiO_2 layer is prevented by the nitride layer. The current, which is directly proportional to the current density, flows through the poly-Si and the dissipated electrical power is turned into heat. 16 of the 32 contact windows are used for leading the current into the poly-Si layer and the other 16 are used for the outflow of the current. The maximum operating current is about 80 mA, i.e. $\sim$5 mA for each contact window. The concave ring form of the poly-Si structure is achieved in two steps:

1) Growth of a poly-Si layer at 625 °C on the whole surface by applying low pressure CVD due to

$$SiH_4(g) \rightarrow Si(s) + 2H_2(g) \tag{A.2}$$

2) Photolithography makes all the unmasked area, except the central ring structure, vulnerable to etching. The selective etching process, described hereunder, removes the vulnerable area and the photo resist outstanding ring structure remains. Afterwards, the photo resist must be removed by stripping.

A.1.5 The BPSG layer

After the outstanding poly-Si structure with steep edges is produced, an enclosing plane insulation layer is needed.

For the planarisation of the poly-Si structure, the BPSG reflow method is applied [Hilleringmann [38]]. BPSG stands for boron phosphorus-doped silicate glass. Each element has a concentration of 4% in the BPSG layer. After the deposition of the BPSG layer, a high temperature treatment at 900 °C (melting point) is processed. During melting, the liquid glass flows over the steep edges and can achieve smoothness and planarisation after cooling down.

The contact windows can be etched locally by means of lithography and etching. Anisotropy during etching must be high. Experimentation has shown

that the selective wolfram CVD provides optimal results for filling the contact windows while keeping the planar structure. The wolfram CVD takes place at 400 °C due to

$$3SiH_4 + 4WF_6 \rightarrow 4W + 3SiF_4 + 12HF \tag{A.3}$$

A.1.6 The PSG layer with buried interdigitated electrodes

The structure of the interdigitated electrodes can be achieved by a Physical Vapor Deposition (PVD) step covering the whole surface. For this substrate, evaporisation or sputtering of the metals (Ti:25 nm+Pt:175 nm) can be done. The two-layered electrodes result from the fact that Ti has a very good adhesion feature and Pt has excellent conductivity. Sputtering is achieved by an ion beam shooting on to a negative target cathode. In simple cases, the cathode is made up of the metal concerned. The ion beam usually has a very high energy level in the keV range. As a result, atoms or molecules of the target sputter out and deposit on to the substrate's surface and build up a homogeneous thin layer. After sputtering, as the next step, lithography + anisotropy etching can be applied to form the interdigitated structure.

Almost identical to the BPSG step described in Section A.1.5, the PSG reflow is used where a phosphorous-doped silicate glass with an 8% doping content, instead of the boron phosphorous mixture, is produced. The difference to the BPSG step is that the temperature treatment is carried out at a higher temperature (950 °C, the melting point of PSG).

A.2 Temperature of gas-sensing measurement substrates

As described in Section 3.1, the microhotplates used for gas-sensing measurement have a poly-silicon layer for heating and a temperature sensitive resistance (TSR) to obtain information about the current operating temperature. These layers have to be included in a temperature control set-up consisting of a measuring transducer, a personal computer and an actuator.

The measuring transducer is used to convert the electrical resistance of the temperature sensitive layer into a voltage signal so that the personal computer can handle it. A measurement card (ME2600, Meilhaus Electronic GmbH, Germany) can receive voltage values in the range of -10V to +10V. Thus, it is necessary to use this measurement range. Figure A.1 shows a circuit diagram to apply the measurement range. A constant voltage signal of 10 V is impressed on a voltage divider, which consists of a resistance of 3.7 kΩ and the TSR, and on another fixed voltage regulator which generates a reference voltage of 5 V. At room temperature, the dropped voltage at the TSR is usually 4 V. The voltage which is dropped at the TSR is applied together with the 5 V signal to an operation amplifier. The operation amplifier subtracts both voltage signals and amplifies them by a factor of 10. The measurement card can then work in its full measurement range. Accordingly, the voltage signal which is received from the measurement card can be transferred into a value for the operating temperature if the substrate has been calibrated. The computer compares the current temperature with a set-point in order to apply a defined current to the heating layer.

The current which flows through the heating layer (poly-Si) is adjusted by an npn-transistor. The basis measurement current card of the computer controls the current through the heating layer. A voltage of 58 V has to be applied to the heating layer with an electrical resistance of ∼500 Ω in order to ensure that the maximum operating temperature is achieved. Figure A.2 shows a heating system circuit diagram together with the transistor to control a defined current flow through the heating layer.

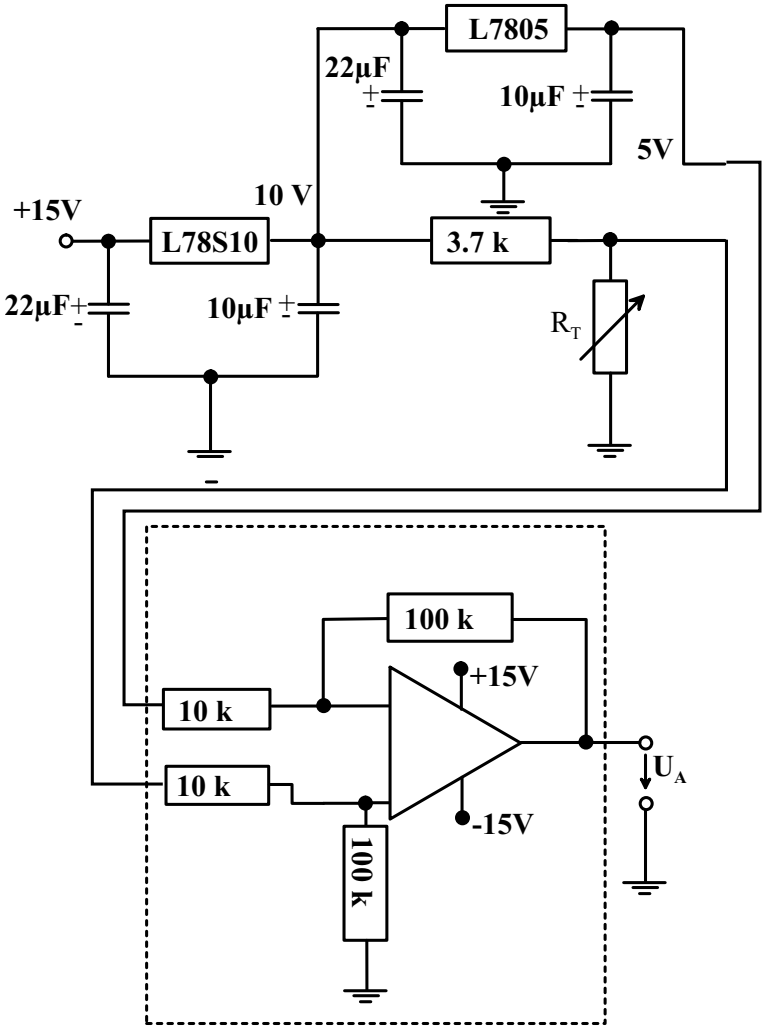

Figure A.1: Circuit diagram to determine the operating temperature.

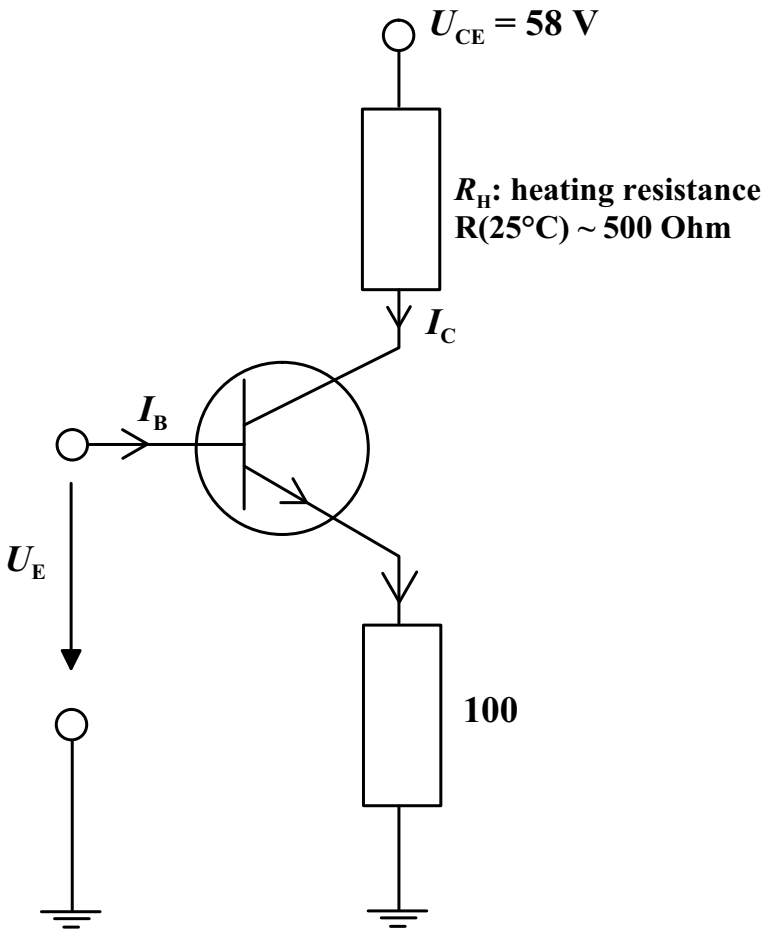

Figure A.2: Circuit diagram of the heating system for substrates used for gas-sensing measurements.

Bibliography

References

[1] Adachi M., Okuyama K., Kousaka Y. and Tanaka H. **(1988)**
Preparation of gas sensitive film by deposition of ultrafine tin oxide particles.
J. Aerosol Sci. 19(2): 253 – 263.

[2] Atkins P.W. **(1990)**
Physical Chemistry
Oxford University Press, Oxford 4th edition, 601.

[3] Baik N.S., Sakai G., Shimanoe K., Miura N. and Yamazoe N. **(2000)**
Hydrothermal treatment of tin oxide sol solution for preparation of thin-film sensor with enhanced thermal stability and gas sensitivity.
Sensors and Actuators B65, 97 – 100.

[4] Baraton M.I., Merhari L., Ferkel H. and Castagnet J.F. **(2002)**
Comparison of the gas sensing properties of tin, indium and tungsten oxides nanopowders: carbon minoxide and oxygen detection.
Mater. Sci. Eng. C19(1-2), 315 – 321.

[5] Barbi G.B. and Blanco J.S. **(1993)**
Structure of tin oxide layers and operating temperature as factors determining the sensitivity performances to NO_x.
Sensors and Actuators B15-16, 372 – 378.

[6] Capone S., Rella R., Siciliano P. and Vasanelli L. **(1999)**
A comparison between V_2O_5 and WO_3 thin films as sensitive elements for NO detection.
Thin Solid Films 350 (1-2) 264 – 268.

[7] Cavicchi R.E., Walton R. M., Aquino-Class M., Allen J. D. and Panchapakesan B. **(2001)**
Spin-on nanoparticle tin oxide for microhotplate gas sensors.
Sensors and Actuators B77, 145 – 154.

[8] Chang S.C. **(1980)**
Oxygen chemisorption on tin oxide: correlation between electrical conductivity and EPR measurements.
J. Vac. Sci. Technol. 17, 366 – 369.

[9] Chen D.R., Pui D.Y.H., Hummes D., Fissan H., Quant F.R. and Sem G.J. **(1998)**
Design and evaluation of a nanometer aerosol differential mobility analyzer (Nano-DMA).
J. Aerosol Sci. 29: 497 – 509.

[10] Choe Y.S., Chung J.H., Kim D.S., Kim G.H. and Baik H.K. **(1999)**
Phase transformation and morphological evolution of ion-beam sputtered tin oxide films on silicon substrate.
Mater. Res. Bull. 34, 1473 – 1479.

[11] Choi W.K., Cho J.S., Song S.K., Jung H.J., Koh S.K., Yoon K.H., Lee C.M., Sung M.C. and Jeong K. **(1997)**
The characterization of undoped SnOx thin film grown by reactive ion-assisted deposition.
Thin Solid Films 304, 85 – 97.

[12] Choi W.K., Song S.K., Cho J.S., Yoon Y.S., Jung H.J., Koh S.K. and Choi D. **(1997)**
H_2 gas-sensing characteristics of SnO_x sensors fabricated by a reactive ion-assisted deposition with/without an activator layer.
Sensors and Actuators B40, 21 – 27.

[13] Chung W.Y., Lim J.W., Lee D.D., Miura N. and Yamazoe N. **(2000)**
Thermal and gas-sensing properties of planar type micro gas sensors.
Sensors and Actuators B64, 118 – 123.

[14] Coblenz W.S. **(1990)**
The physics and chemistry of the sintering of silicon.
J. Mater. Sci. 25, 2754 – 2764.

[15] Comini E., Faglia G. and Sberveglieri G. **(2001)**
UV light activation of tin oxide thin films for NO_2 sensing at low temperatures.
Sensors and Actuators B78, 73 – 77.

[16] Cukrov L.M., McCormick P.G., Galatsis K. and Wlodarski W. **(2001)**
Gas sensing properties of nanosized tin oxide synthesized by mechanochemical processing.
Sensors and Actuators B77, 491 – 495.

[17] de Keijser T.H., Langford J.I., Mittemeijer E.J. and Vogels A.B.P. **(1982)**
Use of the Voigt function in a single-line method for the analysis of X-ray diffraction line broadening.
J. Appl. Cryst. 15, 308 – 314.

[18] Delpha C., Siadat M. and Lumbreras M. **(2000)**
Discrimination of a refrigerant gas in a humidity controlled atmosphere by using modelling parameters.
Sensors and Actuators B 62(3), 226 – 232.

[19] Delpha C., Siadat M. and Lumbreras M. **(2001)**
An electronic nose using time reduced modelling parameters for a reliable discrimination of Forane 134a.
Sensors and Actuators B 77(1-2), 517 – 524.

[20] Dieguez A., Romano-Rodriguez A., Morante J.R., Kappler J., Barsan N. and Göpel W. **(1999)**
Nanoparticle engineering for gas sensor optimisation: improved sol-gel fabricated nanocrystalline SnO_2 thick film gas sensor for NO_2 detection by calcination, catalytic metal introduction and grinding treatments.
Sensors and Actuators B60, 125 – 137.

[21] Dieguez A., Romano-Rodriguez A., Morante J.R., Weimar U., Schweizer-Berberich M. and Göpel W. **(1996)**
Morphological analysis of nanocrystalline SnO_2 for gas sensor applications.
Sensors and Actuators B31, 1 – 8.

[22] Dieguez A., Vila A., Cabot A., Romano-Rodriguez A., Morante J.R., Kappler J., Barsan N., Weimar U. and Göpel W. **(2000)**
Influence on the gas sensor performances of the metal chemical states introduced by impregnation of calcinated SnO_2 sol-gel nanocrystals.
Sensors and Actuators B68, 94 – 99.

[23] Dixkens J. and Fissan H. **(1999)**
Development of an electrostatic precipitator for off-line particle analysis.
Aerosol Sci. Technol. 30, 438 – 453.

[24] Endres H.E., Jander H.D. and Güttler W. **(1995)**
A test system for gas sensors.
Sensors and Actuators B23, 163 – 172.

[25] Faglia G., Benussi G., Depero L., Dinelli G. and Sberveglieri G. **(1996)**
NO_2 sensing by means of SnO_2(Al) thin films grown by the rheotaxial growth and thermal oxidation technique.
Sensors and Materials 8, 239 – 249.

[26] Fau P., Sauvan M., Trautweiler S., Nayral C., Erades L, Maisonnat A. and Chaudret B. **(2001)**
Nanosized tin oxide sensitive layer on a silicon platform for domestic gas applications.
Sensors and Actuators B78, 83 – 88.

[27] Figaro Engineering Inc., Japan.
Technical Reports
www.figarosensors.com

[28] Fromm E. **(1998)**
Kinetics of Metal-Gas Interactions at Low Temperature.
Springer-Verlag Berlin-Heidelberg, 16.

[29] Geurts J., Rau S., Richter W. and Schmitte F.J. **(1984)**
SnO-films and their oxidation to SnO_2: Raman scattering, IR-reflectivity and x-ray diffraction study.
Thin Solid Films 121, 217 – 223.

[30] Göpel W., ed.: Sberveglieri G. **(1992)**
Future trends in the development of gas sensors.
Kluwer Academic Publishers 365 – 409.

[31] Göpel W. **(1994)**
New Material and transducers for chemical sensors.
Sensors and Actuators B18, 1 – 21.

[32] Göpel W. and Reinhardt G. **(1996)**
Metal oxide sensors: new devices through tailoring interfaces on the atomic scale. From Sensors Update edited by Baltes H., Göpel W. and Hesse J.
VCH Verlagsgemeinschaft mbH, Weinheim, Germany.

[33] Göpel W. and Schierbaum K.D. **(1995)**
SnO_2 sensors: current status and future prospects.
Sensors and Actuators B26, 1 – 12.

[34] Hagen J. **(1996)**
Technische Katalyse - Eine Einführung.
VCH - Weinheim, 109-111.

[35] Hagwood C., Sivathanu Y. and Mulholland G. **(1999)**
The DMA Transfer Function with Brownian Motion a Trajectory/Monte-Carlo Approach.
Aersol Sci. Techn. 30, 40 – 61.

[36] Harvey I., Coles G. and Watson J. **(1989)**
The development of an environmental chamber for the characterization of gas sensors.
Sensors and Actuators 16, 393 – 405.

[37] Herrmann J.M., Disdier J., Fernandez A., Jiminez V.M. and Sanchez-Lopez J.C. **(1997)**
Oxygen gas sensing behavior of nanocrystalline tin oxide prepared by the gas phase condensation method.
Nanostructured Materials 8, 675 – 686.

[38] Hilleringmann U. **(2002)**
Silizium Halbleitertechnologie.
Teubner Verlag Stuttgart, Germany.

[39] Ihokura I., Watson J. **(1994)**
The stannic oxide gas sensor. Principles and applications.
CRC Press, Inc. Boca Raton, Florida.

[40] Ihokura K., Tanaka K. and Murakami N. **(1983)**
Use of tin dioxide sensor to control a domestic gas heater.
Sensors and Actuators 4, 607 – 612.

[41] Jimenez V.M., Caballero A., Fernandez A., Espinos J.P., Ocana M. and Gonzalez-Elipe A.R. **(1999)**
Structural characterization of partially amorphous SnO_2 nanoparticles by factor analysis of XAS and FT-IR spectra.
Solid State Ionics 116, 117 – 127.

[42] Jin Z., Zhou H.J., Jin Z.L., Savinell R.F. and Liu C.C. **(1998)**
Application of nano-crystalline porous tin oxide thin film for CO sensing.
Sensors and Actuators B52, 188 – 194.

[43] Joo B.S., Choi N.J., Lee Y.S., Lim J.W., Kang B.H. and Lee D.D. **(2001)**
Pattern Recognition of Gas Sensor Array Using Characteristics of Impedance.
Sensors and Actuators B77, 209 – 214.

[44] Kennedy M.K., Kruis F.E. and Fissan H. **(2000)**
Gas phase synthesis of size selected SnO_2 nanoparticles for gas sensor applications.
Mater. Sci. Forum 343-346, 949 – 954.

[45] Kennedy M.K., Kruis F.E., Fissan H. and Mehta B.R. **(2003)**
A fully-automated gas-sensing and electronic parameter measurement setup for miniaturized nanoparticle gas sensors.
Rev. Sci. Instr. in print.

[46] Kennedy M.K., Kruis F.E., Fissan H., Mehta B.R., Stappert S. and Dumpich G. **(2003)**
Tailored nanoparticle films from monosized tin oxide nanocrystals: particle synthesis, film formation, and size-dependent gas-sensing properties.
J. Appl. Phys. 93, 551 – 560.

[47] Kruis F.E., Fissan H. and Rellinghaus B. **(2000)**
Sintering and evaporation characteristics of gas-phase synthesis of size-selected PbS naoparticles.
Mat. Sci. Eng. B69-70, 329 – 334.

[48] Kruis F.E., Nielsch K., Fissan H., Rellinghaus B. and Wassermann E.F. **(1998)**
Preparation of size-classified PbS nanoparticles in the gas phase.
Appl. Phys. Lett. 73, 547 – 549.

[49] Kupriyanov L.Yu. **(1996)**
Semiconductor sensors in Physico-Chemical Studies.
Handbook of Sensors and Actuators. Santa Clara, USA, 27.

[50] Lantto V. **(1994)**
Semiconductor gas sensors as an example of thick-film transducers.
Informacije MIDEM 26(4), 228 – 237.

[51] Lantto V., Romppainen P. and Leppavuori S. **(1988)**
A study of the temperature dependence of the barrier energy in porous tin dioxide.
Sensors and Actuators 14, 149 – 163.

[52] Lee D.S., Huh J.S. and Lee D.D. **(2003)**
Classifying combustible gases using micro-gas sensor array.
Sensors and Actuators B93, 1 – 6.

[53] Li F.,Xu J.,Yu X., Chen L., Zhu J., Yang Z. and Xin X. **(2002)**
One-step solid-state reaction synthesis and gas sensing property of tin oxide nanoparticles.
Sensors and Actuators B81, 165 – 169.

[54] Liu Z.G., Hu W.S., Wu Z.C. and Feng D. **(1996)**
Comparative study of laser ablation techniques for fabricating nanocrystalline SnO_2 thin films for sensors.
Materials Letters 28, 369 – 372.

[55] Maffeis T.G.G., Owen G.T., Wilks S.P., Malagu C., Martinelli G., Kennedy M.K. and Kruis F.E. **(2003)**
Direct evidence of the dependence of surface state density on the size of SnO_2 nanoparticles observed by scanning tunneling spectroscopy.
submitted.

[56] Maisels A., Kruis F.E., Fissan H., Rellinghaus B. and Zähres H. **(2000)**
Synthesis of tailored composite nanoparticles in the gas phase.
Appl. Phys. Letters 77, 4431 – 4433.

[57] Malagu C., Guidi V., Stefancich M., Carotta M.C. and Martinelli G. **(2002)**
Model for Schottky barrier and surface states in nanostructured n-type semiconductors.
J. Appl. Phys. 91(2), 808 – 814.

[58] Martinelli G., Carotta M.C., Traversa E. and Ghiotti G. **(1999)**
Thick-film gas sensors based on nano-sized semiconducting oxide powders.
MRS Bulletin, 30 – 36.

[59] McAleer J.F., Moseley P.T., Noris J.O.W, Williams D.E and Tofield B.C. **(1987)**
Tin dioxide gas sensors.
J. of Chem. Soc., Faraday Transactions 1 83, 1323 – 1346.

[60] Menz W., Mohr J. and Paul O. **(2001)**
Microsystems Technology.
Wiley-VCH, Weinheim, Germany.

[61] Metzger T.H., Kegel I., Paniago R. and Peisl J. **(1999)**
Grazing incidence x-ray scattering: an ideal tool to study the structure of quantum dots.
J. of Physics D-Appl. Phys. 32, A202 – A207.

[62] Nagel R., Hahn H. and Balogh A.G. **(1999)**
Diffusion processes in metal/ceramic interfaces under heavy ion irradiation.
Nucl. Instr. and Meth. in Phys. Res. B148, 930 – 935.

[63] Nayral C., Viala E., Colliore V., Fau P., Senocq F., Maisonnat A. and Chaudret B. **(2000)**
Synthesis and use of a novel SnO_2 nanomaterial for gas sensing.
Appl. Surf. Sci. 164, 219 – 226.

[64] Promsong L. and Sriyudthsak M. **(1995)**
Thin tin-oxide film alcohol-gas sensor.
Sensors and Actuators, 504 – 506.

[65] Ogawa H., Abe A., Nishikawa M. and Hayakawa S. **(1981)**
Preparation of tin oxide films from ultrafine particles.
J. Electrochem. Soc. 128(3), 685 – 689.

[66] Ogawa H., Abe A., Nishikawa M. and Hayakawa S. **(1981)**
Electrical properties of tin oxide ultrafine particle films.
J. Electrochem. 128(9), 2020 – 2025.

[67] Ogawa H., Nishikawa M. and Abe A. **(1982)**
Hall measurement studies and an electrical conduction model of tin oxide ultrafine particle films.
J. Appl. Phys. 53, 4448 – 4455.

[68] Pan Q., Xu J., Dong X. and Zhang J. **(2000)**
Gas-sensitive properties of nanometer-sized SnO_2.
Sensors and Actuators B66, 237 – 239.

[69] Pan X.Q., Fu L. **(2001)**
Oxidation and phase transitions of epitaxial tin oxide thin films on (1012) sapphire
J. Appl. Phys. 89, 6048 – 6055.

[70] Panchapakesan B., DeVoe D.L., Widmaier M.R., Cavicchi R. and Semancik S. **(2001)**
Nanoparticle engineering and control of tin oxide microstructures for chemical microsensors applications.
Nanotechnol. 12, 336 – 349.

[71] Park H.S., Shin H.W., Yun D.H., Hong H.K., Kwon C.H., Lee K.C. and Kim S.T. **(1995)**
Tin oxide micro gas sensor for detecting CH_3SH.
Sensors and Actuators B25, 478 – 481.

[72] Prost W., Kruis F.E., Otten F., Nielsch K., Rellinghaus B., Auer U., Peled A., Wassermann E.F., Fissan H. and Tegude F.J. **(1998)**
Monodisperse Aerosol Particle Deposition: Prospects for Nanoelectronics.
Microelect. Eng. 41/42, 535 – 538.

[73] Ramamoorthy R., Kennedy M.K., Nienhaus H., Lorke A., Kruis F.E. and Fissan H. **(2003)**
Surface oxidation of monodisperse SnO_x nanoparticles
Sensors and Actuators B88 281 – 285.

[74] Sakai G., Baik N.S., Miura N. and Yamazoe N. **(2001)**
Gas sensing properties of tin oxide thin films fabricated from hydrothermally treated nanoparticles: dependence of CO and H_2 response on film thickess.
Sensors and Actuators B77, 116 – 121.

[75] Satterfield C.N. **(1970)**
Mass transfer in heterogeneous catalysis.
Cambridge, Mass.: MIT Press.

[76] Schierbaum K.D., Weimar U., Kowalkowski and Göpel W. **(1991)**
Conductivity, workfunction and catalytic activity of SnO_2-based sensors.
Sensors and Actuators B3, 205 – 214.

[77] Schmid W., Barsan N. and Weimar U. **(2003)**
Sensing of hydrocarbons with tin oxide sensors: possible reaction path as revealed by consumption measurements.
Sensors and Actuators B89, 232 – 236.

[78] Seiyama T., Kato A., Fujiishi K. and Nagatani M. **(1962)**
A new detector for gaseous components using semiconductor thin film.
Anal. Chem. 34, 1502 – 1503.

[79] Sentürck R. **(2003)**
Überprüfung einer Hall-Messeinrichtung zur elektrischen Charakterisierung von Zinnoxid-Nanopartikelschichten. Diploma thesis, Universität Duisburg-Essen.

[80] Shek C.H., Lai J.K.,Lin G.M. and Zheng Y.F. **(1997)**
Nanomicrostructure, chemical stability and abnormal transformation in ultrafine particles of oxidized tin.
J. Phys. Chem. Solids 58, 13 – 17.

[81] Shimizu Y. and Egashira M. **(1999)**
Basic aspects and challenges of semiconductor gas sensors.
MRS Bulletin 24, 18 – 24.

[82] Stiles K. and Kahn A. **(1988)**
Correlation between E_F pinning and development of metallic character in Ag overlayers on GaAs (110).
Phys. Rev. Let. 60, 440 – 443.

[83] Suito K., Kawai N. and Masuda Y. **(1975)**
High pressure synthesis of orthorhombic SnO_2.
Mater. Res. Bulletin 10, 677 – 680.

[84] Thiel B. and Helbig R. **(1976)**
Growth of SnO_2 single crystals by a vapour phase reaction method.
J. Crystal Growth 32, 259 – 264.

[85] Umweltsensortechnik GmbH
Technical Reports
www.umweltsensortechnik.de

[86] Ulrich M., Kohl C.D. and Bundle A. **(2001)**
Percolation model of a nanocrystalline gas sensitive layer.
Thin Solid Films 391, 299 – 302.

[87] Wada K. and Egashira M. **(2000)**
Hydrogen sensing properties of SnO_2 subjected to surface chemical modification with ethoxylsilanes.
Sensors and Actuators B62, 211 – 219.

[88] Weisz P.B. **(1953)**
Effects of electronic charge transfer between adsorbate and solid on chemisorption and catalysis.
J. of Chem. Phys. 21(9), 1531 – 1538.

[89] Williams G. and Coles G.S.V. **(1999)**
The gas-sensing potential of nanocrystalline tin oxide produced by a laser ablation technique.
MRS Bulletin 24, 25 – 29.

[90] Wilson D.M. and de Weerth S.P. **(1997)**
Signal processing for improving gas sensor response time.
Sensors and Actuators B41 63 – 70.

[91] Xu C., Tamaki J., Miura N. and Yamazoe N. **(1991)**
Grain size effects on gas sensitivity of porous SnO_2-based elements.
Sensors and Actuators B3, 147 – 155.

[92] Yoo K.S., Cho N.M., Song H.S. and Jung H.J. **(1995)**
Surface morphology and gas-sensing characteristics of SnO_{2-x} thin films oxidized from Sn films.
Sens. Actuators B25, 474 – 477.

[93] Zampiceni E., Bontempi E., Sberveglieri G. and Depero L.E. **(2002)**
Mo influence on SnO_2 thin films properties.
Thin Solid films 418, 16 – 20.

[94] Zemel J.N. **(1988)**
Theorectical description of gas-film interaction on SnO_x.
Thin Solid Films 163, 189 – 202.

[95] Zhang G., Liu M. **(2000)**
Effect of particle size and dopant on properties of SnO_2-based gas sensors.
Sensors and Actuators B69, 144 – 152.

[96] Zhu J.H., Brunner K. and Abstreiter G. **(1998)**
Observation of 105 facetted Ge pyramids inclined towards vicinal Si(001) surfaces.
Appl. Phys. Lett. 72, 424 – 426.

List of Figures

List of Tables

Marcus Kennedy
Rochusstraße 24
40479 Düsseldorf
Email: m-kennedy@t-online.de

Persönliche Angaben:

Geburtsdatum:	06.03.1971
Geburtsort:	Bonn
Familienstand:	verheiratet
Staatsangehörigkeit:	Irisch

Schulbildung:	08/83 - 06/90	Gymnasium: Christian-Wirth-Schule, Usingen Abschluß: allgemeine Hochschulreife
Berufsausbildung:	09/90 - 02/93	Ausbildung zum Chemielaboranten, Fresenius AG, Bad Homburg v.d.H.
Studium:	10/93 - 02/99	Studium der Materialwissenschaften, Technische Universität Darmstadt Vertiefungsrichtung: Physikalische Metallkunde, Dünne Schichten, Oberflächentechnik Abschluß: Diplom-Ingenieur
Promotion:	01/04	Dissertation in der Fakultät für Ingenieurwissenschaften, Universität Duisburg-Essen Abschluß: Doktor-Ingenieur

Berufliche Erfahrung:

03/93 - 09/93	Chemielaborant, Fresenius AG in Bad Homburg v.d.H.
03/99 - 12/03	wissenschaftlicher Angestellter im Fachgebiet Prozeß- und Aerosolmeßtechnik, Universität Duisburg-Essen
seit 01/04	Projektingenieur, PEAK Werkstoff GmbH, Velbert